Title
Experimental Study on Laser Additive Manufacturing of Metal Matrix Nanocomposite

Author
Lin, Ting Chiang

Publication Date
2018

Peer reviewed|Thesis/dissertation

UNIVERSITY OF CALIFORNIA

Los Angeles

Experimental Study on Laser Additive Manufacturing of Metal Matrix Nanocomposite

A dissertation submitted in partial satisfaction of the

requirements for the degree Doctor of Philosophy

in Mechanical Engineering

by

Ting Chiang Lin

2018

ABSTRACT OF THE DISSERTATION

Experimental Study on Laser Additive Manufacturing of Metal Metrix Nanocomposites

by

Ting Chiang Lin

Doctor of Philosophy in Mechanical Engineering

University of California, Los Angeles, 2018

Professor Xiaochun Li, Chair

The objective of this study is to experimentally provide insights and guidance for rational design of laser additively manufactured high-performance metal matrix nanocomposites (MMNCs) for various applications. Laser additive manufacturing (LAM) has emerged as a popular metal manufacturing platform to accelerate novel material creation and build high performance products with complex geometries that traditional processes have been impossible to fabricate. However, there still exist great challenges in LAM of conventional metals and its alloys such as absence of porosities, poor surface morphologies or hot cracking, deteriorating the resulting material performance. MMNCs consisting two or more different phases give a potential opportunity to obtain enhanced material properties, suggesting a novel route for LAM to tackle the great challenges. Nevertheless, problems arise from agglomeration of nanoparticles and processing difficulties due to the introduction of secondary phase. In this dissertation, a wide variety of MMNCs were laser additively manufactured to experimentally study the nanoparticle effects on

powder morphology, laser reflectivity, micro/nanostructure and resulting material performance, providing insightful processing routines for LAM of high-performance MMNCs.

The MMNC powder is one of the major factors for LAM to obtain a desired component. In this study, two fabrication techniques, i.e., nanoparticle self-assembly with assistance of ultrasonic processing or mechanical mixing, were used to produce MMNC powders including aluminum metal matrix nanocomposites (AMNCs), aluminum silicon alloy matrix nanocomposites (AlSi12-TiC), and copper matrix nanocomposites (Cu-WC). MMNC powders with different volume ratio (x) between nanoparticles, i.e., titanium carbide (TiC) or tungsten carbide (WC), and matrix, i.e., Al, AlSi12 or Cu, were prepared, including AMNC with x=0.25 and x=1, AlSi12-TiC with x=0.05; x=0.25, and Cu-WC with x=0.1, x=0.25; x=0.66, respectively. The reflectivity measurements of ultrasonic processed powders show a significant decrease in laser reflectivity at the wavelength of 1070 nm as the nanoparticle fraction increases. Moreover, the analysis of light scattering (LS) and scanning electron microscope (SEM) reveals that a uniform size distribution of ultrasonic processed powders. Nanoparticles were self-assembled at the surface of the matrix powders due to the favorable energy state. Internal microstructures revealed by focused ion beam (FIB) show a uniform distribution and good dispersion of nanoparticles throughout the matrix powders. In addition, to demonstrate the scalability, two different mechanical mixing techniques were developed to produce MMNC powders, namely, wet mechanical mixing and dry mechanical mixing. Whereas the powders produced via wet mechanical mixing show the laser reflectivity of the powders decreases as the nanoparticle fraction increases, while the reflectivity of dry mechanical mixed powder, i.e., Cu-WC (x=0.66), only exhibits a slight reduction due to the less nanoparticle coverage on the matrix copper. The powders (Al system) with a spherical shape and uniform size produced by wet mechanical mixing are

similar to those by the ultrasonic processing, demonstrating a good scalability of the technique. For copper matrix system, more efforts are still needed to improve the powder morphology, size distribution, and nanoparticle dispersion and distribution inside the matrix. This study provides a scalable and low cost route for mass production of MMNC powders with high loadings of nanoparticle for LAM.

Experimental studies on LAM of two types of AMNC powders were carried out to investigate the nanoparticle effects on micro/nanostructure and material performance. Assembled powders by both ultrasonic processing and mechanical mixing, were additively manufactured by laser melting using a customized laser additive manufacturing system. AMNCs (with 17 vol.% TiC and 35 vol.% TiC) were successfully laser deposited via laser melting. The material performance shows that the Young's modulus, yield strength, and hardness of the AMNCs increase as the nanoparticle fraction increases. The AMNC (35 vol.% TiC) delivers a yield strength of up to 1.0 GPa, plasticity over 10 %, and Young's modulus of approximately 200 GPa. The AMNC (35 vol.% TiC) offers unprecedented performance in terms of specific yield strength, specific Young's modulus, and elevated temperature stability at 400 ºC amongst all aluminum alloys. The exceptional mechanical properties are attributed to high density of well-dispersed nanoparticles, strong interfacial bonding between nanoparticles to aluminum, and ultrafine grain sizes (approximately 331 nm). Additionally, AMNC (15 vol.% TiC) sample was laser deposited via melting of powders produced by the mechanical mixing, offering comparable mechanical properties to that of AMNC (17 vol.% TiC). The study paves a new pathway for laser additive manufacturing of nanoparticles reinforced aluminum for widespread applications.

To achieve comparable mechanical properties of AMNCs, laser additive manufactured AlSi12 matrix nanocomposites, i.e., AlSi12-TiC (x=0.05 and x=0.25), were successfully produced.

Micro/nanostructure analysis shows that the grain size of AlSi12-TiC nanocomposites decrease as the fraction of incorporated nanoparticles increases. Additionally, chemical reaction products, i.e., SiC nanoparticles and Al_3Ti intermetallic phase, have been identified and observed by X-ray diffraction (XRD) and transmission electron microscopy (TEM). The microhardness and Young's modulus of the laser deposited AlSi12-TiC (x=0.25) were increased to 578 ± 42.5 HV and 187.73 ± 28 GPa, respectively, showing comparable properties to that of AMNC (35 vol.% TiC), i.e., 330.3 ± 30.6 HV and 197 ± 27 GPa. The improved results can be attributed to the dispersed nanoparticles and reaction products. This research suggests a new design route to directly deposit high performance aluminum alloys by benefiting from the strengthening effects of the minor phase(s) in alloy while decreasing the amount of incorporated nanoparticles.

The experiments on LAM of Cu matrix nanocomposites were carried out to explore the feasibility on high performance copper materials. While a great number of porosities with ball-liked morphologies appeared after laser melting of the powders on a pure copper substrate, good layer uniformity and densification of the additively manufactured samples were obtained by replacing the pure Cu with nickel or as-cast MMNC substrate, mainly because of less thermal conductivity difference and good wettability between the powders and substrates. The internal microstructures exhibit a uniform nanoparticle distribution but some nanoparticle agglomeration exists in the matrix. The grain structure of laser deposited samples has refined by the laser induced rapid solidification rate and incorporated nanoparticles, showing a smaller grain size than that of as-cast MMNC samples. The study experimentally demonstrates a feasible processing way to directly laser deposit dense Cu matrix nanocomposites.

In summary, extensive experimental studies presented in this dissertation have demonstrated various feasible processing methods of LAM to produce high-performance MMNC.

A wide variety of laser deposited MMNCs produced in this study can provide insights and guidance to LAM on powder fabrication (nanoparticle selection, volume fractions, reflectivity, size and morphology, and scalability) and processing/microstructure/properties relationships. This study also advances the knowledge base for rational design of high-performance MMNCs with desirable properties for various applications.

The dissertation of Ting Chiang Lin is approved.

Tsu-Chin Tsao

Pei-Yu Chiou

Yongje Hu

Xiaochun Li, Committee Chair

University of California, Los Angeles

2018

Dedicated to my mother for her unconditional love.

TABLE OF CONTENTS

ACKNOWLEDGEMENTS

I would like to thank my advisor Xiaochun Li for his continuous support and guidance of my Ph.D. journey. It would be impossible for me to successfully go through Ph.D. study without his patience and motivation. His guidance encouraged me in all the time of research. I am grateful to have the opportunity to learn the novel science-driven manufacturing technologies from him, which build up my research attitude and even future career.

Besides my advisor, I would like to acknowledge the rest of my doctoral committee: Professors Tsu-Chin Tsao, Pei-Yu Chiou and Yongje Hu, for their valuable inputs and insightful comments, which widen my research from various perspectives.

My sincere thanks also go to all of my colleagues in the research group and friends in Taiwan and UCLA. Without their precious support it would not have been possible to conduct this research. I must especially thank Dr. Chao Ma, Chezheng Cao, Max Sokoluk, YuSheng Kuo, and Chia-Hung Hung for their help in my research and our numerous discussions. I am grateful to have them as good friends and excellent collaborators.

Finally, I must express my deepest gratitude to my mother for supporting me spiritually throughout Ph.D. journey and my life.

VITA

2013, M.S., Mechanical Engineering, National Taiwan University of Science and Technology

2011, B.S., Mechanical Engineering, National Taiwan University of Science and Technology

Journal Papers

- **T.C. Lin**, et al., "Fabrication of Metal–Polymer Nanocomposites by In-Fiber Instability", *J. Manuf. Sci. Eng.* ASME, 2016, 4, 041008
- C. Ma, J. Zhao, C. Cao, **T.C. Lin**, et al., "Fundamental Study on Laser Interactions with Nanoparticles Reinforced Metals—Part I: Effect of Nanoparticles on Optical Reflectivity, Specific Heat, and Thermal Conductivity", *J. Manuf. Sci. Eng.* ASME, 2016, 138, 121001
- C. Ma, J. Zhao, C. Cao, **T.C. Lin**, et al., "Fundamental Study on Laser Interactions with Nanoparticles Reinforced Metals—Part II: Effect of Nanoparticles Surface Tension, Viscosity, and Laser Melting", *J. Manuf. Sci. Eng.* ASME, 2016, 138, 121002
- J. Zhao, A. Javadi, **T.C. Lin**, et al., "Scalable Manufacturing of Metal Nanoparticles by Thermal Fiber Drawing", *J. Manuf. Sci. Eng.* ASME, 2016, 4, 041002
- A. Javadi, J. Zhao, C. Cao, M. Pozuelo, Y. Yang, I. Hwang, **T.C. Lin**, et al "Stretching Micro Metal Particles into Uniformly Dispersed and Sized Nanoparticles in Polymer", *Scientific reports*, 2017, 7(1), 7098.

Conference Papaers

- **T.C. Lin**, J. Zhao, A Javadi, et al., "Feasibility study on thermal drawing of polymer fibers containing micro/nano metal wires", Flexible Automation (ISFA), 2016, 378-381.
- M. S. Mutyala, A. Javadi, J. Zhao, Lin, **T.C. Lin**, et al., "Scalable Platform for Batch Fabrication of Micro/Nano Devices on Engineering Substrates of Arbitrary Shapes and Sizes", *Procedia Manufacturing*, 2015, 1, 205-215.

- M. S. Mutyala, J. Zhao, Lin, **T.C. Lin**, et al., "Study on materials and fabrication of functional thin film AlN force sensors", *Journal of Manufacturing Processes*, 2015, 19, 233-238.
- M. S. Mutyala, L. Chen, L., **T.C. Lin**, et al., "Surface Modification of Polycrystalline Diamond Compacts by Carbon Ion Irradiation", 2016, *Procedia Manufacturing*, 5, 634-643.

CHAPTER 1 INTRODUCTION

1.1 Background and motivation

Recently, additive manufacturing has emerged as a popular manufacturing technology to speed up product creation. A machine for additive manufacturing fabricate parts with arbitrary shapes directly from three-dimensional computer aided design (CAD) models without any fixtures, tooling, and human intervention demanded of traditional manufacturing process. This novel manufacturing technology is able to directly produce the parts that traditional processes have been impossible to fabricate. Currently common techniques used in additive manufacturing are stereolithography (SLA), three dimensional printing (3DP), selective Laser sintering/Melting (SLS/SLM), and fused deposition modeling (FDM). In addition, environmental friendly products produced using additive manufacturing techniques such as rapid freeze prototyping (RFP) and freeze-form extrusion fabrication (FEF) have been reported[1-3]. Among all the additive manufacturing processes, laser additive manufacturing (LAM) is of significance to directly fabricate functional metallic tooling and components that meet the demanding requirements in the field of aerospace, defense, automotive and biomedical industries[4-10].

However, there are some intrinsic and long-standing challenges associated with laser additive manufacturing of conventional metals and metal alloys. For example, high reflectivity metals with high thermal conductivities such as aluminum and copper require a high energy input to fully melt the powders[5,11,12]. Powders with poor flowability also pose a difficulty to the powder spreading process in LAM[11]. Moreover, some lightweight materials like titanium or aluminum are sensitive to oxidation or chemical reaction, inhibiting metallurgical bonding with previous built layers and thus leading to a great amount of porosities[13]. Furthermore, a vast majority of current

conventional alloys, e.g., Al7075, cannot be laser additively printed because of intolerable microstructures with large columnar grains and cracks[14,15]. These challenges require significant efforts for post processing, e.g., surface or thermal treatments, to obtain the parts with desired material performance.

Recently, metal matrix nanocomposites (MMNCs) have emerged as an important new class of metallic materials with nano-sized particulates reinforced in the metal matrix. MMNCs consisting of a metal matrix reinforced with nanoparticles offer very different physical and mechanical properties from those of the matrix. For example, with incorporation of nanoparticles, MMNCs have great potentials to obtain significantly enhanced mechanical properties/performance (e.g., strength, ductility, stiffness, wear resistance, and creep resistance), thermophysical properties, electrical properties, and so on. In recent years, extensive research and development in this area are trying to unleash such unusual properties for widespread applications[4,16-22]. Several manufacturing technologies have been developed to produce MMNCs including electrodeposition[23-25], solidification processing [26,27], high energy ball milling and so on. Nanocomposite concept was also introduced to laser additive manufacturing (LAM). Various nanoparticles were mixed or incorporated into the original powders to investigate the potential benefits for LAM[4,28-40]. However, most of the previous researches mainly focused on the improvement of material performance. So far, only little fundamental understanding has been obtained on the accumulative effects of nanoparticles on laser reflectivity and their interaction with micro/nanostructure and material performance during the laser layered deposition of MMNCs. Moreover, numerous unresolved issues such as agglomeration of nanoparticles have been observed, which little research on the improvement of distribution and dispersion of nanoparticles have been reported. Therefore, there is a great opportunity to acquire the knowledge of the nanoparticle

effects on laser reflectivity and understand how to successfully laser deposit materials with a uniform dispersion and distribution of nanoparticles. This dissertation could provide us insights and guidance on how to improve the mechanical performance during LAM of MMNCs, possibly broadening its fabrication capability and application space.

1.2 Research objectives

This study is to experimentally provide insights and guidance for rational design of laser additively manufacturing (LAM) of high-performance metal matrix nanocomposites (MMNCs) for various applications. More specifically, the research objective is to understand the nanoparticles effects on laser reflectivity of powders, micro/nanostructure and mechanical properties of laser additively manufactured components.

1.3 Work summary

The remaining chapters of this dissertation include

- Chapter 2 reviews the state-of-art additive manufacturing techniques and MMNCs processing.
- Chapter 3 discusses fabrication of MMNCs powders using two processing routes
- Chapter 4 presents experimental results on LAM of aluminum matrix nanocomposite (AMNCs) by selectively melting the novel powders presented in Chapter 3.
- Chapter 5 studies the LAM of aluminum alloy matrix nanocomposite (i.e., AlSi12-TiC system)
- Chapter 6 explores the feasibility on LAM of copper matrix nanocomposite (i.e. Cu-WC system)
- Chapter 7 draws conclusions
- Chapter 8 recommends future work

CHAPTER 2 LITERATURE REVIEW

2.1 Laser additive manufacturing of metallic materials

The term of "laser additive manufacturing (LAM)" implies layer by layer shaping and consolidation of a feedstock, which typically is powder, to form complex geometries using laser. Current typical LAM technologies include but not limit to direct metal laser sintering (DLMS), laser engineered net shaping (LENS), and selective laser sintering/melting (SLS/SLM)[1,4,41]. Detailed process description will be introduced at section of 2.3.5. Materials have been developed so far include aluminum[2,5,6,11,14,15,42-47], copper[28,48-5448,53,55-61], titanium[31,32,62-69], stainless steel[7,70,71], nickel[9,72-78], iron[79] and so on. This section will first briefly review common laser additively manufactured materials and then mainly focus on reviewing LAM of aluminum and copper systems that are more related to this study.

2.1.1 LAM of stainless steel

A longstanding challenge existing in pure metals and alloys is to overcome the strength-ductility trade-off[80]. Austenitic 316L stainless steel (SS) has a major drawback of low yield strength approximately 250 to 300MPa[81], which requires metallurgical routes such as rolling and forging to simultaneously achieve high strength and ductility. Wang et al., successfully demonstrated stainless steel parts with an ultimate tensile strength (UTS) of about 700MPa and a ductility of about 36% using laser additively manufacturing[7]. The structure-property relationship of the additively manufactured steels has been investigated, revealing that the parts exhibit a hierarchically heterogeneous microstructure with multiple length scales from nano to sub-millimeters. Furthermore, cellular structures of the printed parts contain a large fraction of low-angle grain boundaries, nonconventional ripple-like grain shapes and broad grain size distribution, that are commonly observed in alloys manufactured using commercial additive manufacturing

machine (Concept Laser in the study). A variety of deformation mechanisms including dislocation slips, cellular wall evolution and deformation twinning offers a progressive work-hardening mechanism. To conclude, these heterogeneous microstructures are determinant for the exceptional combination of strength and ductility of the material.

2.1.2 LAM of titanium (Ti) and Ti based alloy

Pure titanium or titanium alloy are an excellent candidate for LAM because of its high strength, low density, high corrosion resistance and good biocompatibility[32,62,63]. Densification behavior, microstructure evolution and wear performance of SLMed pure Ti parts were reported[31,63]. The presence of refined martensitic α′ features in the sample improved the hardness but limited the wear performance due to the poor densification. Fatigue resistance, crack growth behavior and microstructure of printed part were investigated by Leuders et al.[62], showing challenges such as porosity, residual stress, and chemical reaction (α′ martensite) that have been also observed in other report[64]. Thijs et al. studied the microstructure evolution on SLM-ed Ti-6Al-4V components, revealing that the direction of grains is mainly determined by the scanning strategy and part geometry[64]. Moreover, precipitation of an intermetallic Ti3Al phase was also observed with a lower scanning speed during the processing.

In addition, the biomedical applications of SLM-ed titanium alloys such as (Ti-6Al-7Nb[65]and Ti-24Nb-4Zr-8Sn[66]) have been reported. The metallic porous titanium structure with mechanical properties closed to those of bones allows a better bone ingrowth and implant fixation[67-69]. Further researches are necessary to ensure the reliability of the printed parts for human body tests[70].

2.1.3 LAM of nickel based alloy (superalloy)

Nickel-based superalloys have been widely applied to various fields especially aerospace industry because of its good weldability, excellent creep resistance, and high temperature corrosion resistance. Laser additive manufacturing enables a rapid fabrication of complex structure, offering a significant advantage to directly produce Ni based alloys. Materials produced by LAM include but not limit to Inconel 625[72], Inconel 718[9,73-75], Nimonic 263[76], and Inconel 738[77]. Liu et al.[74] and Amato et al.[78] studied the microstructure-mechanical properties relationship of IN718. The residual stress development of Nimonic 263 was studied by Vilaro et al.[76]. The detailed microstructure characteristics and mechanical properties of IN738LC and IN625 were presented by Cloots et al.[77] and Li et al[72]. These studies show the range of LAM research being conducted in the super alloy society.

2.1.4 LAM of aluminum (Al) and Al based alloy

Lightweight materials, such as aluminum (Al) and its alloys, have been extensively used in today's society for energy saving and environmental sustainability because of their high specific stiffness, high specific strength, and good ductility etc[82-84]. Laser additive manufacturing (LAM) of aluminum alloys for complex, lightweight products is highly desirable for numerous applications, such as aerospace and automobile components and systems[5,11,42]. However, there exist a number of challenges in the LAM of aluminum powders. Aluminum powders have a relatively high reflectivity (>91%)[11] in the typical LAM laser wavelength, and show high thermal conductivity, suggesting the requirement for a high laser power to overcome the rapid heat dissipation and meet the requirement of powder melting[5]. Also, the inherently light aluminum with poor flowability poses a difficulty to the powder spreading process in LAM[11]. Moreover, one of the main difficulties for the effective LAM of aluminum is the oxidation[2,43]. Aluminum powders

are extremely sensitive to oxidation whether solid or molten state, and thus during the laser processing the adherent thin oxide films exposed on the molten aluminum reduce the wettability and hinder the formation of desired melt[11]. Even after solidification, the entrapped oxide films within the material possibly generate the weakness regions of the component[44]. Therefore, the oxidation issue may be the more significant problem in LAM than other conventional manufacturing of aluminum, because the surface oxide film on the powder may be stirred and incorporated into the molten poor during the laser processing, which affects any surrounding solid parts and also inhibits metallurgical bonding with the previous built layers[42], leading to the initiation of spheroidization, i.e., balling effect, or interior porosities[4]. Consequently, aluminum based powders are very unsuitable for LAM despite the same particle shape and size distribution as other metallic powders[4,11]. The major challenges include porosity minimization[5,45,46] and hot cracking[14].

Extensive efforts have been focused on the above issues. Recent studies showed that the preheating of building platform can improve the laser absorptivity[71] and significantly enhance the dimensional and shape accuracy of the final LAM parts[47]. The poor flowability of aluminum powders can be also improved by having the powders with a spherical shape and uniform size distribution[5,42,85]. By optimizing the process parameters, the mechanical properties of LAM AlSi10Mg specimens are comparable to those of components processed by conventional methods[45,46]. Introduction of Si powder (4 wt.%) into 7075 aluminum alloy shows the improvement of fluidity and thus successfully suppressing the hot cracks in common LAM of Al-7075[14].

Nevertheless, despite a significant amount of LAM research has been carried out on Al-Si based alloy, it is so far impossible to obtain parts from most other high strength aluminum alloys

that meet the strength of their wrought counterpart[5,6]. It is very problematic in laser 3D printing of high strength aluminum alloys that offer a yield strength up to about 500 MPa, such as 7000 series, since they are prone to hot cracking[14,15] during laser layered deposition and solidification. Efforts for post processing, e.g., surface or thermal treatments, are required to obtain the desired material performance.

2.1.5 LAM of copper (Cu) and Cu based alloys

Copper and its alloys have been widely used for conducting materials in electrical engineering because of their excellent thermal and electrical conductivities[86]. Also, copper is widely used in manufacturing of tool inserts and cooling components of semiconductors because of its relatively low in cost and outstanding mechanical properties such as high corrosion resistance and machinability. Recently, Laser Additive Manufacturing (LAM) has emerged as a popular platform to accelerate novel material creation and build high performance products that have traditionally been impossible to fabricate because of the variety in material compositions and/or of their complex shapes. However, it is extremely difficult to directly deposit dense copper parts via LAM. Copper, with an inherently high laser reflectivity (>99%)[12] at the typical laser wavelength, i.e., 1060 nm, and its high thermal conductivity (390 W m^{-1} K^{-1}), requires a high energy input to fully melt the powder materials. Figure 2-1 shows the typical problems of insufficient melting of Cu-based powders[48]. While the improvement of powder melting was demonstrated using high energy input (from 325W to 425W), the poor surface morphologies still suggest that the difficulty of LAM of Cu.

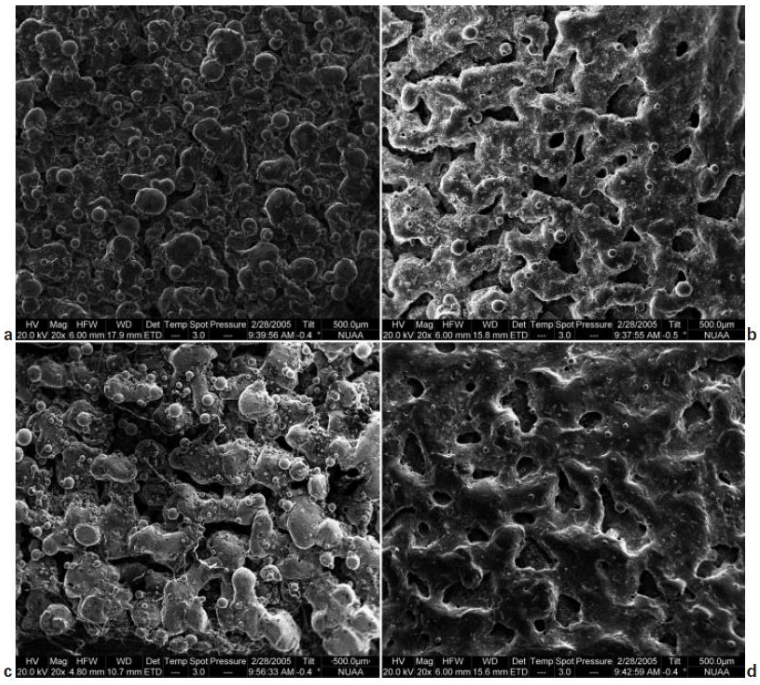

Figure. 2-1: Surface morphologies of laser processed samples at different energy densities. **a,** 350W with 0.04 m/s. **b,** 350W with 0.02 m/s. **c,** 425W, 0.06m/s. **d,** 425W with 0.03m/s.

Extensive research has been reported on the LAM of several different copper-based material systems including Cu-Cu3P[49], Cu-SCuP[50,51], $Cu_{75}H13$[52], WC-Cop/ Cu[53], W-Cu/Cu[28,54], Cu-CuSn-CuP[48,53], Cu84.5Sn8P6.5Ni1[55], Cu-30Ni[56], C18400 Cu[57], Cu-10Sn[58], Cu-Cr-Zr-Ti[59], and etc. Most studies have been carried on exploring the workable Cu-based materials and investigating the effects of the laser processing parameters on the microstructure evolution, sintering/densification behavior, and phase transformation of specimens during LAM. Major challenges arise from porosity, distortion, delamination, balling, and curling[4], resulting in a large amount of effort for post processing.

D. Gu et al[53] deposited WC-10%CO/Cu metal matrix composites by laser processing of composite powders produced via mechanical mixing. The influence of reinforcement contents, i.g. 20%, 30% and 40%, on the densification and microstructure evolution of the Cu matrix was

investigated. The results show that the optimal 30 wt. % reinforced SLM-ed parts provide a 90.3% theoretical density, a hardness of 391.9 (HV0.1), and a fracture strength of 256 MPa.

D. Gu et al[28] studied the densification behavior and microstructure evolution of laser sintered W-Cu components using different processing parameters, e.g. energy densities, hatching space, and powder layer thickness. The results showed that a sound densification level (>92% theoretical density) of the Cu components can be obtained under an energy density range from ~13 to 18 kJ/m combined with a scan speed less than 0.06 m/s. The author also suggested that narrowing a hatching space or decreasing a powder layer thickness to 0.15 mm are potential methods to benefit the printing quality, e.g., inter-layer bonding and surface roughness.

While SLM of a high dense bulk copper alloys are extremely difficult to achieve, Becker et al[10] demonstrated that various copper alloys with a density of 99.9% can be produced by SLM with a maximum powder of 1000W. The first components with internal cooling channel have been manufactured and currently being testing in industrial applications, as shown in Fig. 2-2.

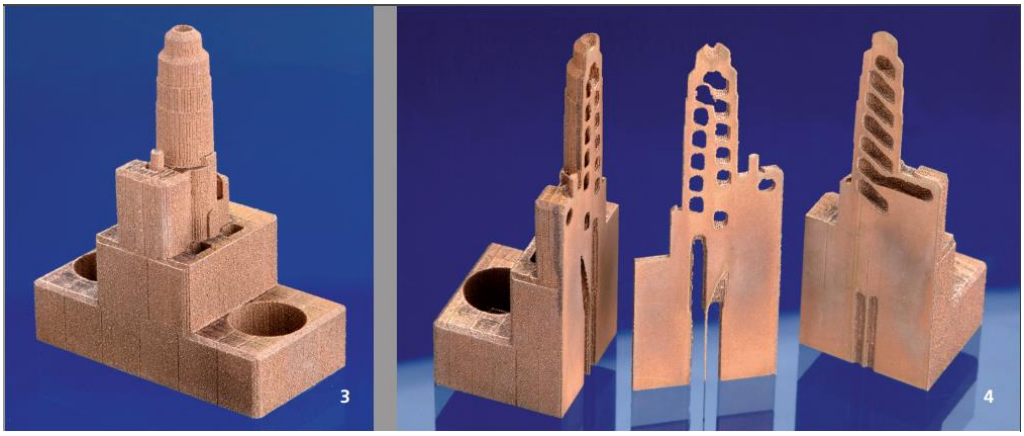

Figure 2-2: Tool inserts with internally located cooling structures were produced by additive manufacturing[10].

Liu et al[57] studied the feasibility of multi-material processing in SLM by producing tensile blocks of 316L stainless steel/C18400 copper alloy. The interfacial characterization of the samples

were studied via focused ion beam (FIB), scanning election microscopy (SEM), energy dispersive spectroscopy (EDS) and electron back scattered diffraction techniques (EBSD). While a well metallurgical bonding at the steel/Cu interface (Fig. 2-3a) and the porosity free from the side of stainless steel (Fig. 2-3c), cracks (Fig. 2-3b) were observed on the stainless side close to the interface. Moreover, significant porosities, as shown in Fig. 2-3d, were observed at the Cu side due to insufficient melting of powders. The defects later strongly affect the tensile testing because most of failure was occurred on the copper side. The author also characterized C18400 copper SLMed parts via tensile testing. The ultimate tensile testing (UTS) is only 49 ± 0.3 MPa, suggesting the difficulty of copper printing.

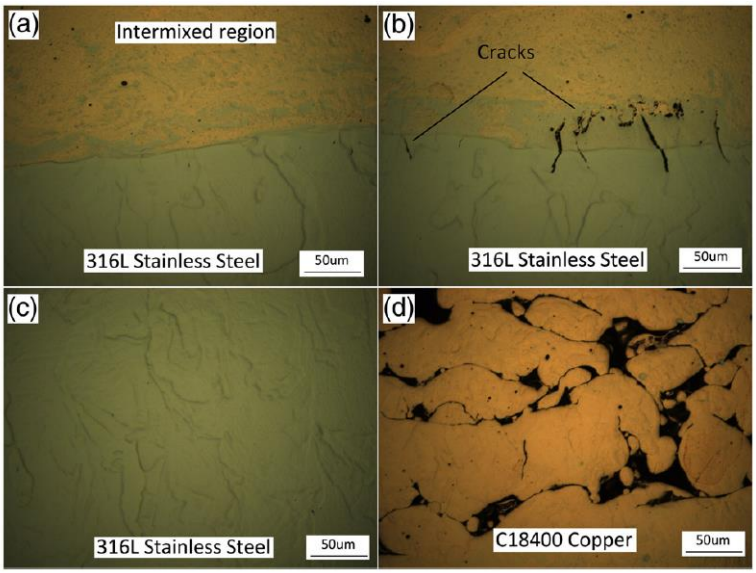

Figure 2-3: As polished cross sectional image of a steel/Cu sample[57] of a, Interfa**ce b,** cracks at the steel side **c,** steel bulk and **d,** copper bulk**.**

Song et al[60] demonstrated the possibility of SLMed W-Cu alloy thin wall parts that can be used as integrated circuit substrate, heat radiator, heat sink and etc. Three different type of micro powders, i.e., CuW25, CuSn10, and CuP8, were mixed using a stirring mixer under argon protection for 4 hours, followed by SLM process under different laser powders from 100W to

120W, scanning speeds from 200 m/s to 700m/s, a scanning interval of 0.08mm, a spot size of 70 μm, and a layered thickness of 25 μm. While hundreds of thin-walled electronic radiators were produced using SLM, as shown in Fig. 2-4a, problems such as defects or insufficient melting of powders were observed as Fig. 2-4b.

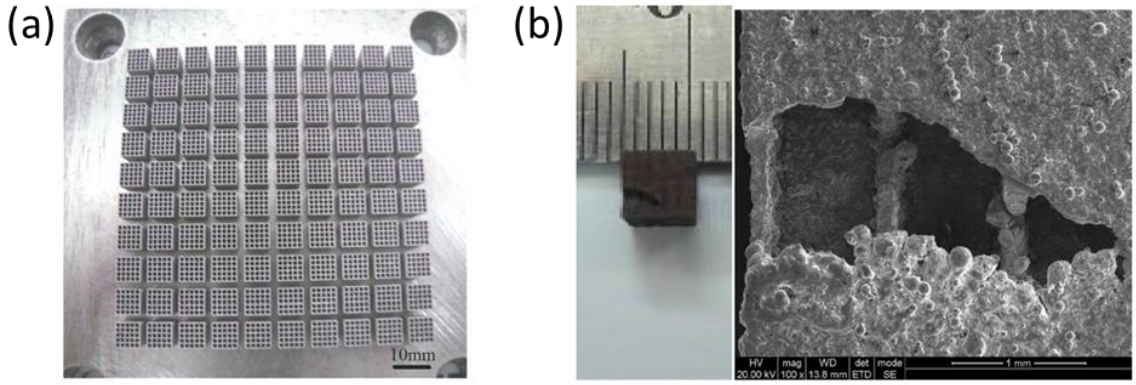

Figure 2-4: a, Mass production of thin wall heat sink using SLM. **b,** Defects caused by improper processing parameters.

Scudino et al[58] produced high dense (99.7%) bulk Cu-10Sn bronze samples using SLM, followed by microstructure and mechanical characterization of the specimens. The SLM-ed specimens display a refined microstructure consisting of dendrites of the α-Cu(Sn) phase along with an interdendritic (α+δ)-eutectoid. The room temperature tensile tests, as shown in Fig. 2-5, reveal that a yield strength of 220 MPa and an ultimate strength of 420 MPa from SLM-ed sample, whereas a yield strength of 120 MPa and an ultimate strength of 220 MPa from the casting sample. Also, the ductility of the SLM-ed parts are 17% compared to the casting sample (7%), which can be ascribed to the microstructure refinement induced via laser high cooling rate.

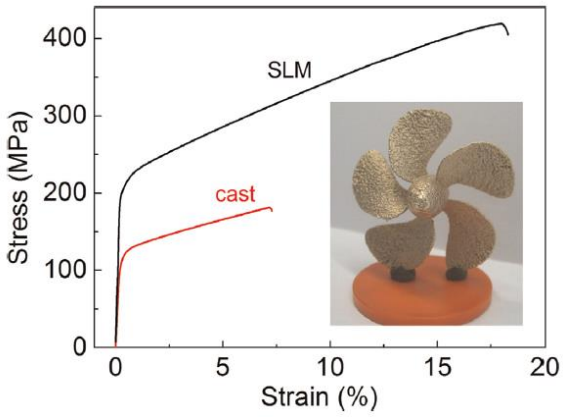

Figure 2-5: Room-temperature stress-strain curve under tensile testing for the cast and SLM Cu-10Sn bronze. (Insert) Cu-10 bronze propeller produced via SLM.

Popovich et al[59] fabricated the production of Cu-Cr-Zr-Ti alloy specimens via SLM, as shown in Fig. 2-6b. The samples were then under heat treatments of an annealing at 980 °C for 30 mins and an aging at 480 °C for 3 hours. The resultant microstructure of the specimens consists of grains along build direction with the size in the range from 30 to 250 μm. The samples perform a room temperature ultimate tensile (UTS) of 195-211 MPa with 11-16% elongation, approximately 20-25% lower than the hot-rolled samples. Porosities in SLM samples were observed, as shown in Fig. 2-6a.

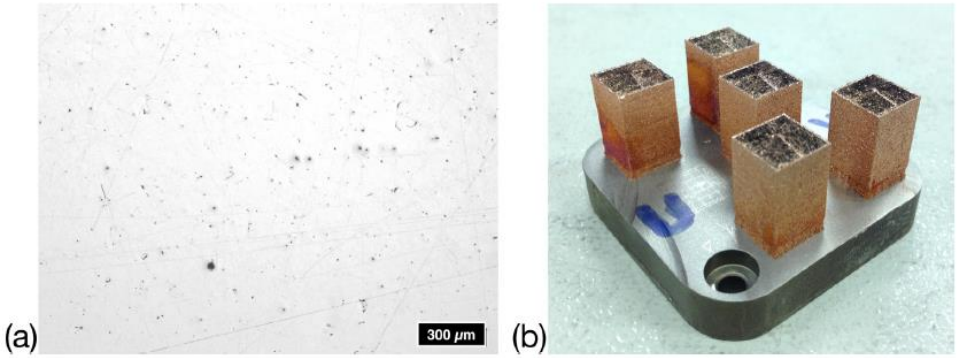

Figure 2-6: a, Microstructure of Cu-Cr-Zr-Ti SLM specimen. **b,** Bulk specimens for microstructure studies in **a.**

Karden et al[61] demonstrated the fabrication of pure bulk coppers (Fig. 2-7a) with a thin wall structure featuring thickness below 11 µm using SLM with an ultrashort laser pulse mode (ULP), which could offers a possibility to control the thermal behavior of molten flow. A spot size of 35 µm and a pulse duration of 500fs were used. The fabricated specimens (2×2×1.4 mm^3) exhibit a porous morphology, as shown in Fig. 2-7b to d. Future research will be focused on powder size preparation.

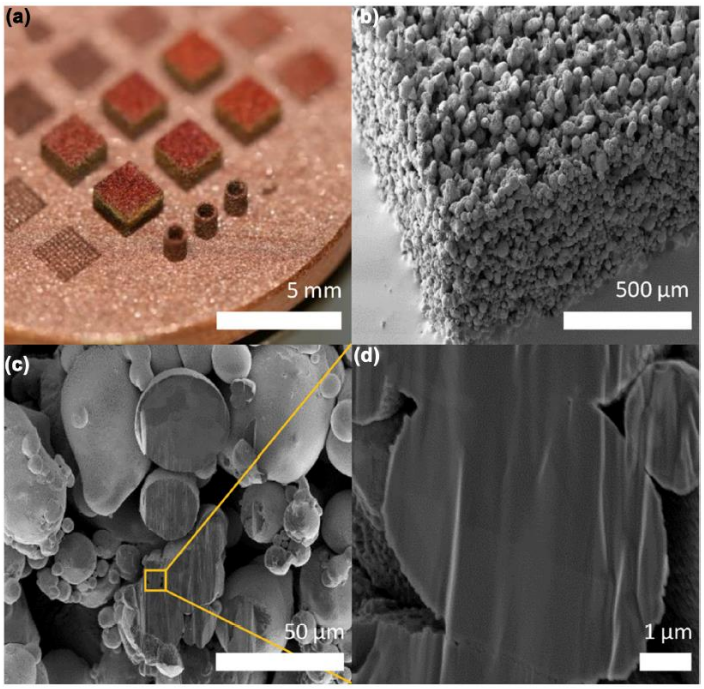

Figure 2-7: A copper sample using SLM with ULP mod. a, Different 3D structures. **b,** A porous structure was observed by SEM. **c,** SEM image was obtained after etching of **c** using Focused Ion Beam (FIB). **d,** Magnified image of **c.**

2.2 Metal Matrix Nanocomposite

Nanocomposite material containing two or more different phases has a potential opportunity to obtain enhanced material properties. Introduction of nanoelements into a base matrix enables a nanocomposite material to possess unusual properties such as chemical, physical, and mechanical properties, which have received a great attention in recent years. Recently, metal

matrix nanocomposite (MMNCs) are being investigated worldwide owing to their promising properties which meet the demand for numerous functional applications[16,17,19,21,22,32,34,87-92]. Several material systems have been experimented. The reinforced nanoelements include nanoparticle, nanofiber, carbon nanotube and so on, while the base matrix are metallic materials such as aluminum, nickel, copper, iron, and titanium. These nanocomposite materials have been widely used in the field of aerospace, automobile, biomedical, and architecture industries.

However, even a large amount of studies are focusing on research of MMNCs, there remain several challenges associated with MMNCs fabrication including how to achieve uniform dispersion and well distribution of nanoparticles, and how to prevent chemical reactions of nanoparticles. The dispersion and distribution of nanoparticles inside the matrix are crucial factors to determine the material properties of the MMNCs. It is well known that mechanical properties can be tremendously improved with uniform nanoparticle dispersion and distribution in the matrix. However, agglomeration of nanoparticles inside the matrix has always observed, decreasing the material performance of MMNCs. Moreover, nanoparticles are often pushed to the grain boundaries by solidification fronts, thereby depleting the nanoparticles from the crystalline grains[93]. In addition, chemical reaction of nanoparticles with matrix in MMNCs is also a challenging issue. It is difficult to avoid the chemical reaction at high processing temperature because such small nanoparticles normally are more reactive than that of the base matrix. To overcome these challenges, it is important to carefully consider the selection of nanoparticles and the processing parameters to realize uniform dispersion of nanoparticles and prevent the potential chemical reactions.

There are various well-developed manufacturing methods to fabricate MMNCs focusing on the improvement of dispersion and distribution of nanoparticles. These methods can be

categorized into two major groups: in-situ and ex-situ. The in situ processes refer to the methods leading to the generation of ceramic nano-compounds by chemical reaction while the ex-situ processes consist of adding nano-reinforcements to the liquid or powdered metal, e.g., solidification processing, electrodeposition, ball milling, powder metallurgy, laser additive manufacturing[4,94]. In particular, ultrasound-assisted casting plays a particularly promising role for its high potential productivity[26]. By combining the solidification processing with ultrasonic nonlinear effects, i.e., cavitation and acoustic streaming, uniform dispersion of nanoparticles in molten metal can be achieved. The mechanical properties of the obtained MMNCs were significantly enhanced compared with that of the base alloys[26,27]. In addition, recently study showed that a dense uniform dispersion of nanoparticles in matrix can be achieved through a nanoparticle self-stabilization mechanism[19]. Although it is still difficult to realize well dispersion of different types of nanoparticles in matrix, this method provides highly possibilities for overcoming long-standing challenges in practice. Electrodeposition is a popular technique to fabricate MMNCs coatings with improved material properties such as wear and corrosion resistance[23-25,95]. This cost-effective and high-throughput process is able to obtain a uniform dispersion and distribution of nanoparticles by carefully tuning the electroplated parameters.

Laser cladding(LC)[96-99]and Laser surface alloying(LSA)[100-103]are surface modification processes which can be used to fabricate MMNCs coating. A great variety of nanopowders were added into the conventional cladding powders forming a nanocomposite powders, followed by processing of high energy laser to form a nanocomposite coating on the substrate. It was shown that the nanoparticles are able to significantly refine the primary phases and even precipitation phases in some systems. Thanks to the microstructure refinement and nanoparticle enhancement,

improvements of material properties were often observed, including hardness, wear resistance, oxidation resistance, thermal shock resistance, corrosion resistance, and cracking resistance.

Additive manufacturing are also used to fabricate nanocomposite materials. Typical additive manufacturing processes for nanocomposite fabrication include three dimensional printing (3DP), selective laser sintering (SLS), fused deposition modeling (FDM), stereolithography (SL), direct laser metal sintering (DMLS), and selective laser melting (SLM) and so on[1,4,41]. Among these additive manufacturing process, laser additive manufacturing is able to fabricate metallic components with complex three-dimensional geometries from metal powders directly. The base materials that have been experimented so far include pure Ti, TiAl alloys, iron, steel, Al alloys, and superalloy. The reinforced element can be either introduced by ex-situ additions or produced by in-situ reactions, which include TiC, SiC, Al_2O_3 and intermetallics[4,28,29,31-35,101]. The enhanced material properties, such as hardness, strength, and oxidation resistance, were performed. However, chemical reaction, phase transformation, and agglomeration of nanoparticles were also observed, where significant research efforts are needed.

2.3 Additive Manufacturing of Nanocomposite

Combining nanotechnology with additive manufacturing has a great opportunity to create an entire new nanocomposite material with unique properties that meet various applications such as aerospace, automotive, biomedical industries and so on. In this section, several additive manufacturing methods integrated with nanotechnology will be introduced. Literature review will be much focused on laser additive manufacturing of metal matrix nanocomposite, which this study much interests in.

2.3.1 Three Dimensional Printing (3DP)

2.3.1.1 Process description

3DP is an additive manufacturing in which a thin distribution of powder is spread over the surface of a powder bed and a polymer binder is selectively jetted onto the powders where the object is to be built. A piston below the powder bed can precisely lower the part so that the next fresh layers can be spread on the top of the previous layer. The binder is again selectively jetted onto the powders following the pre-designed pattern. The layer-by-layer process repeats till the part is fabricated[104].

2.3.1.2 Nanocomposite via 3D printing

Bai et al. added silver nanoparticles (30nm) into water-based binder to prepare a nanosilver suspension for 3DP[105]. The nanoparticles inside the suspension were sintered together at low temperature (300°C) to bond the micro silver powders during 3DP process. The nanoparticles can provide a bonding strength continuously during the sintering, resulting in a higher tensile strength of the final printed silver part compared to that of the pure part without using nanosilver suspension. It was demonstrated that the nanosilver suspension printed parts have less shrinkage, distortions, and higher ductility than that of pure binder printed part.

Czyzewski et al. fabricated conductive components containing carbon nanofibers(CNF) via 3DP technology[106]. CNF was added into an epoxy resin binder so that the build parts can obtain the electrical conductivity after the 3DP process. The plaster-based powder was used in this study. For the surface resistivity, the printed part with the addition of CNF (<4 wt. %) has lower value when compared to the part without introduction of CNF. It is found that the printed part containing agglomeration of CNF has lower electrical resistivity than the part with dispersion of CNF. A percolation theory was given to explain this unexpected result.

2.3.2 Stereolithography (SL)

2.3.2.1 Process description

SL is one of the additive manufacturing in which an ultraviolet laser is used to selectively solidify the liquid photocurable polymer. In the process of SLA, the first layer of the built part mounted on the platform is selectively solidified by a scanning laser beam. The pattern of each layer can be traced from a CAD model which is translated to a STL file during the printing process. Once the first layer of the part is solidified, the platform can precisely lower a certain amount of the part, leading to the next uncured layers of photocurable polymer can be applied on the top of the previous layer for the next scanning cycle. The process is repeated, layer-by-layer, until the part is complete[107].

2.3.2.2 Nanocomposite via Stereolithography

Wozniak et al. developed UV curable transparent SiO_2 nanodispersions for SL process by considering parameters including Van der Waals forces and hydrogen bonding between monomer end group and silica surface[108]. Five types of monomers (i.e., 4HBA, HEA, butyl acrylate, M200 and M282-PEGDA) with different refractive indices closed to SiO_2 were selected to minimize the Van der Waals attraction. Nanodispersions containing 10 vol.% to 40 vol.% SiO_2 nanopowders (40-80 nm) in different monomers were prepared. The viscosity of the obtained nanodispersion was suitable for SL process. Three types of photoinitiator (TPO, ITX, LTM) were used for the UV curing. Results showed that the sintered samples made with >5% TPO were mechanically robust but crystalline, and the samples made with 5% ITX were transparent but with poor mechanical properties. Finally, the samples made with 5% LTM were both transparent and medium mechanical properties.

Sandoval et al. added mutli-walled carbon nanotubes (MWCNTs) into SL epoxy-based resin and processed the resin to fabricate a complex three dimensional parts via SL with a laser power of about 55mW, a critical exposure (E_c) of 60 mJ/cm^2, and a penetration depth (D_p) of 6.5 mm[109]. The mixture were prepared by ultrasonication process for 1 hour to improve the dispersion of MWCNTs. Small concentration of MWCNTs (0.05 wt.%) inside the printed part results in the improvement of mechanical properties, i.e, tensile strength, fracture strength, and hardness. SEM results showed MWNCTs were well bonded inside the SL resin.

Kumar et al. reported the mechanical properties of polymer nanocomposite reinforced by cellulose nanocrystals (CNCs)[104]. The photocurable stereolithographic resins (STRs) were mechanically mixed with 1.0 wt. % CNCs by the help of a magnetic stirrer. Rheological studies of the mixture were performed. Results showed that the mixture with a lower concentration of reinforced elements (less than 5%) were still able to be processed. Mechanical properties of the nanocomposite were significantly improved as the concentration of reinforced CNCs increase.

2.3.3 Fused Filament Fabrication (FFF)/ Fused Deposition Modeling (FDM)

2.3.3.1 Process description

Fused Filament Fabrication (FFF) or Fused Deposition Modeling (FDM) is an additive manufacturing process which the part is deposited by continuously feeding a thin filament of a thermoplastic polymer or wax from a heated nozzle. The typical thickness of the layer is 0.25mm. Deposited materials include polycarbonate (PC), acrylonitrile butadiene styrene (ABS), polyphenylsulfone (PPSF), PC-ABS blends, and PC-ISO[107]. The heated filament can be solidified quickly after it exist the heated nozzle because the filament in general is heated only slightly above the molten point.

2.3.3.2 Nanocomposite via Fused Filament Fabrication (FFF)/ Fused Deposition Modeling (FDM)

Shofner et al. fabricated nanofiber reinforced polymer nanocomposite by FDM[110]. 10 wt. % Vapor-growth carbon fibers (VGCFs) with an average diameter of 100 nm and a length of 100 μm were mixed with acrylonitrile – butadiene – styrene (ABS) copolymer using heated press and further granulated for the starting material for filament extrusion. The nominal diameter of the filament is 1.7mm. SEM images showed that homogenous dispersion of VGCFs inside the matrix filament after the mixing. Mechanical properties of composite material (e.g., tensile tests, dynamic modulus) was increased an average of 39 and 60% compared to the pure ABS deposited part. In addition, the fracture behavior of the nanocomposite after tensile tests indicated that the addition of VGCFs decreased the chain mobility in the polymer.

Chartoff et al. presented a review article for the fabrication of functionally graded polymer matrix nanocomposite[111]. The author demonstrated that adding reinforced nanoelement, i.e., ceramic particles, into low viscosity polymer matrix enables to produce functional polymeric parts. Gradient refractive index lenses (GRIN) used for military application can be fabricated by FDM method because the varied composition of the lenses can be realized by the layer-by-layer process. Several references were summarized in conclusion section indicating that GRIN lenses can be deposited by adding various nanoparticles with different size and concentration into polymer matrix.

FDM can be used to fabricate biocompatible nanocomposite materials. Kim et al. produced bone tissue engineering nanocomposite scaffolds via FDM[112]. The scaffolds containing poly(D,L-lactide:glycolide) (DL-PLGA) and β-tricalcium phosphate (β-TCP). Two different scaffolds were either coated with hydroxyapatite (HA) or uncoated with HA to study the biocompatible effect. The SEM results revealed that the nanocomposite containing DL-PLGA and β-TCP nanoparticles.

In vivo test were performed. The scaffolds were implanted into rabbit and the results showed that the scaffolds were still conductive and biodegraded over 12 weeks. The HA coating did not cause significant impact on the scaffold degradation and bone regeneration of the tested rabbit. In addition, magnetic nanocomposite scaffolds consist of poly(ε-caprolactone) and poly(ethylene glycol) were fabricated by FDM and SL[113]. SEM, X-ray microcomputed tomography were performed. The ability of the printed scaffolds to absorb magnetic nanoparticles was also tested. The results showed that FDM and SL are suitable to fabricate a thin scaffold layer with fined structure for the bone regeneration.

2.3.4 Selective Laser Sintering (SLS)

2.3.4.1 Process description

A laser beam is used to selectively fuse the heat-fusible powders into a solid object. The part is built on a platform. The laser can traces the pattern from a CAD model and fused the first layer of the pattern. The platform is further precisely lowered a certain amount of height so that the following second powder layers can be reapplied. The process is repeated for subsequent layers till the part is completely fabricated[107]. A great variety of powdered materials can be used in this process including plastics, metals, metal alloy, polymer-metal material, and combination of metal and ceramics.

2.3.4.2 Nanocomposite via Selective Laser Sintering

Kim et al. studied the effect of clay nanoparticles on thermalphysical properties and mechanical properties of polymer nanocomposite powders for SLS process[114]. The polymer base for nanocomposite was neat polyamide 6 (N6) and the reinforced nanoparticles are 5 wt. % clay nanoparticles. The average diameter of nanocomposite powders after mechanical mixing were 90-160 μm. Thermal transition temperature was determined by Differential Scanning Calorimeter

(DSC), and the strain-rate of the polymers was measured by standard MFI test (ASTM 1238D). The results showed that after adding clay nanoparticle, the values of sintered fusion and heat crystallization were increased because the nanoparticles increase the clay-polymer chain interactions. The melt flow characteristics of nanocomposites showed higher MFI than that of pure N6, indicating that the higher viscosity were performed after introduction of nanoparticles. The density behavior of nanocomposite powders showed a lower final density than that of standard polymer because the clay nanoparticles hinder the polymer flow. It was believed that sintering of the nanocomposite powders require higher holding temperature than the pure N6 for the SLS process.

Zheng et al. studied the effect of Al_2O_3 nanoparticles (60 nm) on the mechanical properties of Al_2O_3/ polystyrene (PS) nanocomposite produced by SLS[115]. The nanoparticles were coated with PS (50 μm) (i.e., Al_2O_3/PS core-shell nanoparticles) by emulsion polymerization method. Three types of mixed powders were studied: nano-Al_2O_3/PS, Al_2O_3/PS core-shell nanoparticles, and pure PS. All experimental samples were conducted by SLS which working parameters were: a fixed laser power of 24.5W, a scan speed of 1100 mm/s, a scan space of 0.2mm, and a layer thickness of 0.1mm in air atmosphere at room temperature. After SLS, the SEM images showed that many porosities and voids inside the matrix for the samples of pure PS and nano-Al_2O_3/PS. Agglomeration of nanoparticles occurs due to high surface energy. However, for the Al_2O_3/PS core-shell nanoparticles, the SEM results showed a uniform dispersion of nanoparticles inside the matrix. It was believed that during SLS, the outside PS coating on Al_2O_3 nanoparticles are able to serve as a stable hinder layers and thus inhibit the agglomeration of Al_2O_3 nanoparticles. Mechanical properties of nanocomposite, i.e., impact strength (50% increased) and tensile strength (300% increased), were improved compared to the sample of nano- Al_2O_3/PS, and pure PS. In

addition, several studies fabricated polymer nanocomposite via SLS mainly focused on the improvement of mechanical properties[112,116,117]. The base matrix includes polyamide (PA) powder (e.g., PA6, PA12) while the reinforced elements include graphite nanoplatelets (GNP), yttrium stabilised zirconia, ceramic, and clay-based material. These material systems, i.e., nanocomposite powders, processed by SLS showed the possibilities of the enhancement of mechanical properties comparing to the pure base material.

Duan et al. fabricated three dimensional bionanocomposite scaffolds via SLS for bone tissue regeneration[118]. Two different nanoparticles, Calcium phosphate (Ca-P) and carbonated hydroxyapatite (CHAp), were added into two kinds of microsphere, PHBV (poly hydroxybutyrate–co-hydroxyvalerate) and PLLA (poly(L-lactic acid), respectively. The nanoparticles with size in a range of 10-30 nm were synthesized by nanoemulsion method. The nanoparticles were uniformly dispersed in microspheres solution with an assistance of ultrasonification. After evaporation of the solution, the mixing powders were processed by SLS with parameters: a laser scan power of 13-15W, a scan spacing of 0.1-0.15 mm, temperature of 35-45 ˚C, and a scan speed of 1257 mm/s. After SLS, the nanocomposite scaffolds with a size of 8.3 mm (L) × 8.3 mm (W) × 4.4 mm (H) were successfully fabricated. Compression test and in vitro biological evaluation test were performed. Compression tests for nanocomposite scaffolds were conducted under both dry and wet condition to determine the mechanical properties. Results showed that the compressive strength and modulus of nanocomposite scaffolds were higher than that of pure polymers in dry conditions. But after putting sample in the wet conditions for 21 days, the mechanical properties were slightly lower than the pure polymers. Human like cells material (SaOS-2) were used to determine the biological evaluation of nanocomposite scaffolds. After three

days of culture time, almost no dead of testing cells for four types of nanocomposite scaffolds, indicating the high cell viability on the SlS-ed scaffolds.

2.3.5 Laser Additive Manufacturing of Metal Matrix Nanocomposite

2.3.5.1 Direct Metal Laser Sintering (DMLS)

Process description

The DMLS is an additive manufacturing process that enables the rapid production of complex three-dimension geometry directly from metal or metal alloy. The DMLS process is similar to the SLS (i.e., layer-by-layer process). Each thin powdered layer is solidified by selectively laser fusing. After finishing the first layer, a following fresh layer of the powders is deposited and the laser scanning process is repeated. Various material systems (e.g., Fe, Fe-alloy, Ti, Cu-based, tin, stainless steel) have been developed for DMLS.

Metal Matrix Nanocomposite via DMLS

Titanum matrix: Chang et al. produced a Ti reinforced Carbon nanotube (CNTs) nanocomposite via DMLS[119]. The microstructure of the nanocomposite, i.e., densification, distribution, and the material performance, were reported. A processing relationship among laser intensity, microstructure, and material properties, i.e., hardness, and wear rate, was established. A 96.8% density of the nanocomposite was obtained using proper laser intensity (700 J/m), resulting in both the hardness and elastic modulus increase approximately 2.5- and 3.4- fold than that of the pure part. However, as lower intensity applied, the properties were gradually reduced due to the presence of CNT and the poor densification level. In addition, a considerably low friction coefficient of 0.23 and a reduced wear rate of 3.8×10^{-5} mm3 /(N m) were achieved, which can be attributed to the presence of the uniformly dispersed CNT .

Copper matrix: Gu et al. fabricated WC-Co/Cu nanocomposites using DMLS. The irregular shaped WC-10 wt. % Co nanoparticles were mixed with 99% purity Cu powder (15 µm) by ball milling method[120]. After ball milling, the average size of nanoparticles were less than 50 nm. The experiment were conducted using a continuous wave CO_2 laser with a spot size of 0.3mm, a laser power of 700W, a scan speed of 0.05m/s, a powder thickness of 0.20mm, and a scan line spacing of 0.15mm. The powders were supplied by an automatic powder delivery system. Eventually, specimens with dimensions of 50 mm × 10 mm × 9 mm were successfully prepared. XRD showed that the Cu and WC phases were remained inside the matrix after laser melting and a-Co phase were also identified. SEM images showed the reinforced WC nanoparticles were homogenous distributed inside the matrix, but some clusters were formed which the author did not mention. The mechanical properties were measured by nanoindentation tester at room temperature. The hardness and elastic modulus were improved from 1.4-1.6 GPa and 130.5-201.5 GPa to 3.47 GPa and 613.42 GPa, respectively.

Iron matrix: Lin et al. studied the feasibility of uniform distribution of carbon nanotubes inside the Iron matrix during laser sintering[121]. Magnetic stirring with an assistance of a dispersing agent (i.e., Polyvinyl alcohol) was used to mix the mutliwall carbon nanotubes (MWNTs) with an outside diameter 8-15 nm, and iron powders (average of diameter of 4 µm) inside the water solution. The mixing powders were then pre-coated on a mechanically polished substrate. Laser sintering experiment was performed under a N_2 gas filled chamber to avoid the sample oxidation. The processing parameters include a scanning speed of 2 mm/s, an output laser power of 100W, and a beam size of 0.8mm. Simulation results showed that the concentration of MWNTs has a higher effect on the temperature field during laser sintering while the size of MWNTs has a relatively lower effect on the temperature field. In addition, simulation results from COMSOL

showed that the MWNTs inside the matrix material can still be survived after the laser sintering. The results from SEM, TEM, and XRD showed that the MWNTs were successfully integrated into the matrix material. In addition, the surface micro hardness of 2 wt.% MWNTs reinforced nanocomposite showed a higher hardness (605 VHN) compared to the sample without the addition of MWNTs.

2.3.5.2 Selective Laser Melting (SLM)

Process Description

Recently, selective laser melting has received increasing attention for producing MMNCs because this process has capability to rapidly generate three-dimensional parts with very complex geometries from metallic powder directly. SLM is one of the additive manufacturing processes in which a moving high energy laser heating source is used to create components based on layer-by-layer manner. The thin metallic powder layer mounted on a platform is selectively melted and further the following powdered layer is laid on the top of the first layer, followed by laser melting again. The process is repeated until the object is complete[12,122].

Metal Matrix Nanocomposite via SLM

Several studies have been reported on fabrication of MMNCs via SLM. The most of materials developed so far include Titanium[29] , Al based materials[34,89], stainless steel[123], and so on. Mainly reports were focused on the feasibility of workable based material and investigating the effects of the processing parameters on the microstructure sintering/evolution/densification behaviors, and phase transformation of specimen during SLM. Enhancement of the material performance has been shown because of the presence of nano-element. However, major challenges such as balling, porosity, hot cracking, and oxidation have been observed[4]. Reviews for typical materials are discussed in this section.

Titanium matrix: Gu et al. experimentally studied the fabrication and microstructure characterization of Ti-Al matrix nanocomposite reinforced by in-situ formed TiC nanoparticles[29]. The author used high energy ball milling to prepare nanocomposite powders in which micro powders (50 at. % Ti, 25 at. % Al, and 25 at. % graphite) were first mechanically alloyed under argon atmosphere. The nanocomposite powders (TiC/TiAl) were expected to be formed with a molar ratio of 1:1 during the ball milling. XRD showed that TiC and Ti(Al) solid solution were formed. Estimated size of TiC and Ti(Al) were ~12 nm and ~7 nm, respectively. The nanocomposite powders with a thin layer of thickness (0.15mm) were further processed by self-developed SLM utilizing a CW Gaussian CO_2 laser with a wavelength of 10.6 μm, a spot size of 0.30 mm, a power of 800 W, a scan speed of 0.10 m/s and a scan line spacing of 0.15 mm. $TiAl_3$ and Ti_3AlC_2 were formed after laser processing. It was believed that $TiAl_3$ phase tends to precipitated primarily after laser processing, and a small fraction of TiC tends to react with TiAl, resulting in the formation of Ti_3AlC_2. After SLM, the final nanocomposite consists of the phase of $TiAl_3$, Ti_3AlC_2, and TiC nanoparticles.

Aluminum matrix: LAM of Aluminum alloys matrix such as AlSi10Mg and Al7075 have been studied. Li et al., produced AlSi10Mg reinforced TiB_2 nanoparticles using SLM[89]. The gas atomized in-situ nano-TiB_2 decorated AlSi10Mg nanocomposite powder was prepared for SLM (Detailed information of powder is described at next chapter). The printed nanocomposite specimens (10 x 10 x 6mm) were conducted under a wavelength of 1060 μm, a power range of 200 to 300W, a range of scan speed from 800 to 2000 mm/s, a hatching space of 105 μm, and a powder layer thickness of 30 μm. A high purity (99.99%) argon gas atmosphere flow was used during the whole SLM process to minimize the oxidation. The nanocomposite sample shows a tensile strength of 530 ± 16 MPa with ductility approximately 15.5 ± 1.2%, a microhardness of

191 ± 4$HV_{0.3}$, which are higher than most conventional wrought and tempered Al alloys. Martin et al. successfully demonstrated high strength Al7075 can be laser printed by decorating ZrH_2 nanoparticles[124]. The selected nanoparticle was able to introduce heterogeneous nucleation and promote equalized grain growth, thereby reducing stresses generated during solidification. The nanoparticles were selected using data mining software that computes crystallographic lattice spacing and density to offer a low-energy nucleation barrier. Different SLM-ed Al metal alloys, e.g, Al7075 and Al6061, with electrostatically assembled grin-refining nanoparticles, i.e., TiB_2, WC, ZrH_2, were presented in this study. The mechanical properties, e.g., tensile strength, of the resulting printed Al 7075 specimen (after T6) were superior to those sample without the grain refiner and comparable to wrought Al 7075 metal.

Gu et al. reported a novel ring-structure nanoscale TiC reinforcement with a regular distribution in AlSi10Mg matrix can be realized via SLM[34]. The SLM-ed TiC/AlSi10Mg nanocomposite offers a microhardness of 188.3 $HV_{0.1}$ and a tensile strength of 486 MPa with an elongation of 10.9%, which can be attributed to the combined effects of grain refinement and grain boundary strengthening caused by the TiC reinforcement.

Dadbakhsh and Hao et al. investigated the possibility of *in-situ* composites on various Al alloys (Al, AlMg1SiCu and AlSi10Mg) with SLM method[39]. Each alloy powder (40 μm) was mechanical mixed with 15 wt. % Fe_2O_3 powder (< 53 μm) at least 30 mins using a test sieve shaker, showing a homogenous mixing with uniform reddish color powders. Based on their parametric study, suitable processing parameters were found: a spot size of 0.16 mm, a power of 74 W, a scanning speed of 0.20 m/s and a scan line spacing of 0.05 mm. After SLM, in-situ reaction and solidification enables the formation of nanoparticles (~50- 100 nm) including Al-Fe, α-Al_2O_3, Al-Fe-Si intermetallics and Si crystals. The microharnesses of the SLM-ed composites were

significantly improved and higher than that of pure base materials fabricated by traditionally manufactured method (e.g., casting). It was believed that such improvement is associated with the microstructure refinement from rapid solidification and both nanoparticle reinforcing effect

Iron matrix: Song et al. fabricated fully dense nano/micro-scaled SiC reinforced iron matrix composites by SLM[40]. Characterization methods including SEM, XRD, and TEM were used to study the surface morphology, phase structure, and microstructure of the parts. Fe powder with an average particle size (D_{50}) of 20 μm, and hierarchical SiC powder (micro- and nano-scaled) with an average particle size of about 0.7 μm were used. The processing parameters of SLM include a continuous-wave ytterbium fiber laser (1064 -1100 nm) with a laser beam diameter of 34 μm, a laser power of 100 W, a scan speed of 0.33 m/s, and a scan line spacing of 40 um. From the SEM images, it was found that after addition of SiC into the Fe matrix, the obvious liquid front was disappeared and some small particles were seen at the surface. It was believed that the melt flow became less intensive due to the change in local melt instability and viscosity, i.e., higher viscosity after addition of SiC. The formation of reaction products, i.e., Fe_3C, was observed from TEM and XRD results. It was believed that a portion of SiC nanoparticles reacted with Fe during the process and thus formed Fe_3C, while the rest of SiC still remained in the microstructure with the size in micro- and nano-scale. In addition, the structural of Fe matrix was modified with the SiC particles, resulting in the presence of nanosized iron grains and amorphous iron. Tensile tests display a much higher strength of the SLMed Fe/SiC (764±15 MPa) than that of the SLM-ed pure Fe.

Stainless steel matrix: AlMangour et al. presented a bulk TiB2/316L stainless steel nanocomposite by SLM[125]. The nanocomposite powders with different volume percentage of reinforced TiB2 nanoparticles were fabricated using ball milling method, followed by SLM

process. The microhardnesses, yield strength (from microcompression), coefficients of friction, and wear rates of the SLM-ed samples were presented. The microstructure results showed that the sample with an optimal TiB_2 reinforced content, i.e., 10 vol. %, offers homogenous nanoparticles dispersion and ring-like structures along the grain boundaries. While porosities were observed from the nanocomposite with 15 vol.% TiB_2 reinforcement, the sample still showed a higher wear resistance compared to those sample without TiB_2 nanoparticles.

2.3.5.3 The role of nanocomposite powder

2.3.5.3.1 Fabrication methods

Ball milling

For laser additive manufacturing, nanocomposite powders can be prepared by ball milling method[28,31-34,37,38,125]. Different types of micropowder with different sizes, i.e., matrix powder and reinforced powder, inside the ball mill system were grinded and blended by rotation of grinders (e.g., stainless steel grinding balls). The size reduction of the micropowders can be realized by the impact and attrition. The rotation speed, grinding (milling) time, temperature, and working atmosphere, e.g., air, argon, will determine the final mixture. Eventually, after ball milled, the nanoscale particles can be uniformly dispersed throughout the matrix particles. Figure 2-8 shows an example of nanocomposite powders in which TiC nanoparticles (50 nm) were dispersed inside the Ti matrix particles[33].

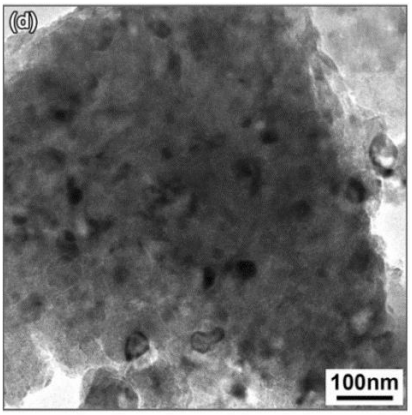

Figure 2-8: TEM image of nanocomposite powders (TiC/Ti)

Mechanical Mixing

Micropowders and nanopowders can be directly mechanical mixed using methods such as milling or mechanical shaker. Gu et al. used a 4 vario-planetary mill machine to mix TiC nanoparticles (50 nm) and Ti (22.5 μm)[33]. The working parameters include mixing time, rotational speed of supporting disk and grinding bowls. After milling, the ultrafine TiC nanoparticles were uniform dispersed around Ti particles surface, as shown in Figure 2-9. These powders prepared by mechanical mixing method were different from the powders produced by ball milling method because the powders did not experience deformation during the mechanical mixing process. Dadbakhsh et al. mixed the Al, AlMg1SiCu and AlSi10Mg (40 μm) with 15 wt% Fe_2O_3 powder (below 53 μm) by a test sieve shaker for blending and vibration the mixture at least 30 mins[39]. After the mixing process, the reddish color of the powders was obtained, meaning that Fe_2O_3 were adhered to the surface of the Al and Al-alloy particles.

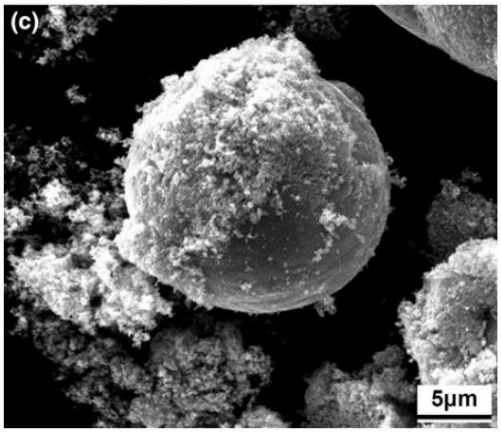

Figure 2-9: SEM image of mechanical mixing nanocomposite powder (TiC/Ti) prepared by mechanical mixing method.

Gas atomization

Recently nanocomposite powders produced by gas atomization have become a potential candidate for LAM. Before gas atomization, the master nanocomposites were first fabricated via in-situ reaction casting method. Reactive salts were added into the molten metal during mechanical stirring, followed by adding other designed elements. The nanocomposite powder was then produced by gas atomization using the master materials. The fabricated powders have a uniform spherical shape, a good nanoparticle distribution in matrix micropowders (Fig. 2-10) and a highly coherent interface between the nanoparticle and the matrix[89,126]. It is expected that the addition of ceramic nanoparticles improve the laser absorption, which also benefit the processing window of LAM.

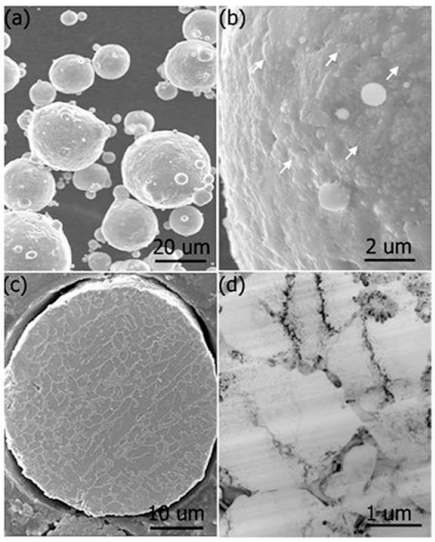

Figure 2-10: SEM images of gas atomized nanocomposite powders.

Self-assembly

Nanocomposite powders can be produced using self-assembly method[127], which developed from previous study. By simply tuning *x*, the volume ratio between nanoparticles and liquid metals, the powders with different structures can be fabricated, as shown in Fig. 2-11. The novel powder structures can be manipulated by self-assembly molten metals and nanoparticles in immiscible liquids driven by reduction of free energy. The author mainly focused on the mechanisms of powder fabrication without investigating the laser interaction with the powders. This dissertation is motivated by studying the effects of produced powder on LAM. Detailed fabrication and results are described in the Chapter 3.

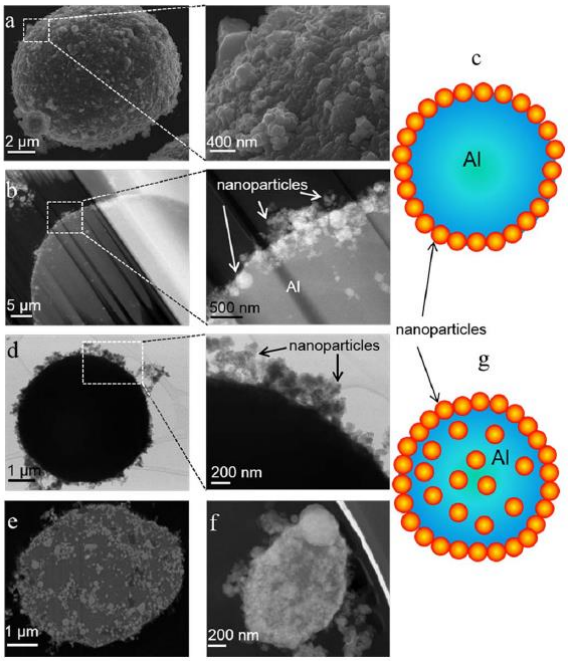

Figure 2-11: Nanocomposite powders produced with different composition of volume ratio (x). a-c, x=0.05. **d-g,** x=0.25[127].

2.3.5.3.2 Enhancement of material properties

Various nanoparticles were added into matrix micropowder with the aim of improving mechanical properties of MMNCs. The improvement of hardness, strength, and wear resistance were commonly observed[9,31-34,37-39]. The mixture of nanopoweder (TiC and TiB_2) reinforced stainless steel SS 316L nanocomposites with ball milling were processed by SLM[37,38]. The size of nanopowder after ball mill is from 60 nm to 120 nm. The results show increased hardness and oxidation resistance compared with the reference sample prepared from 316L steel powder. Additionally, Song et al. applied SLM process to fabricate fully dense nano/micro-scaled SiC reinforced iron matrix composites[40]. The Tensile tests show a much higher strength of the SLMed Fe/SiC (764±15 MPa) than that of the SLMed pure Fe. Moreover, Dadbakhsh et al. reported improved hardness of SLM-ed Al and Al-alloys matrix nanocomposite after using balled milled nanocomposite powders, i.e., 15 wt. % Fe_2O_3 powder[39].

2.4.5.4 Challenges and issues of nanocomposite powder

There exist a number of challenges in the LAM of nanocomposite powders. For example, adding the secondary nanoscale particles into the process would deteriorate the matrix powder flowability[4], posing a difficult to the powder spreading process in LAM. Also, the reflectivity of the nanocomposite powder is different from the matrix powder due to the different laser absorptivity between matrix material and reinforced nanoelements. This may affect or complicate the melt pool behavior due to the different thermal history[128]. To overcome these issues, research shows that the flowability can be improved by having powder with a spherical morphology[85]. Preheating the powder bed is able to improve its laser absorptivity[71]. Finally, nanocomposite produced via LAM has long term challenges of nanoparticle agglomeration and the balling effect[28,33,115,129,130]. These agglomeration behaviors arise from surface effect of nanoparticles. The balling effect arise from improper working parameters such as low laser power and high scan speed[131], resulting in a poor densification and a surface morphology. Figure 2-12 shows an example of typical images of balling effect after SLM process[33]. Gu et al. experimentally proposed a control mechanism to alleviate the balling phenomena[131]. It suggested that high energy density of laser (i.e., higher laser power, lower scan speed, small amount of layer thickness) is possible to decrease the tendency of balling effects. However, it is still difficult to disperse the reinforced nanoelements uniformly inside the matrix.

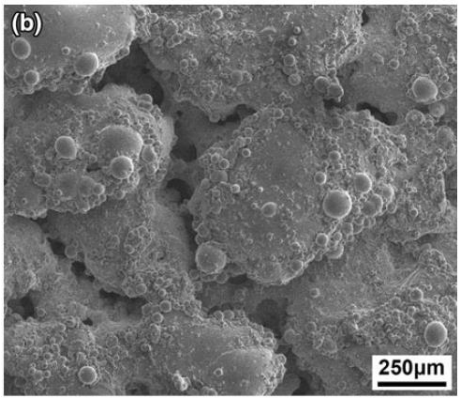

Figure 2-12: SEM image of balling effect after SLM.

Extensive researches have been focused on optimization of laser processing parameters. The ball milled nanocomposite powders were prepared and further processed the powders to form nanocomposites via SLM[31-34]. Particles with different size in micro and nano scale were chosen to form the nanocomposite powders. Results from their recent study showed that Ti/TiC nanocomposite powders were formed with a uniform particle size of 5.8 μm, and TEM showed the TiC nanoparticles with a mean size below 50 nm were uniformly dispersed within the interior Ti matrix[33]. SLM experiments were conducted under argon protection using an Nd:YAG laser (1.064 μm) with a spot size of 70 μm, a scan speed of 0.1–0.4 m/s, a power of 100 W and a hatch spacing of 140 μm. The results showed that with increasing laser energy density, i.e., scan speed decreases, the densification level of a SLMed part was increased. In addition, the SEM image showed that the TiC phases formed lamellar structures with a thickness below 100 nm after SLM. The TiC phase lamellar structures were slightly coarsened and aggregated with increasing energy density. However, for the lower energy density, the poor densification of the structure was performed. Microstructures processed by low and high density are shown in Figure 2-13. It was believed that the formation of lamellar structure was due to the melting and the precipitation of TiC nanoparticles. Since the TiC nanoparticles were relatively uniform dispersed in the interior of Ti matrix, the TiC nanoparticles did not expose to laser directly during the initial stage of laser

melting the. After Ti with sufficient wetting of surrounding Ti liquid, the TiC nanoparticles became melted, followed by a re-precipitation process to form a desired nanostructure. Tribological study showed that with increasing scaning speed the coefficient of friction and wear rate first decreased and then increased. Finally, by combing the sufficient high SLM densification rate and the formation of TiC reinforced nanostructure, the tribological property was considerably improved.

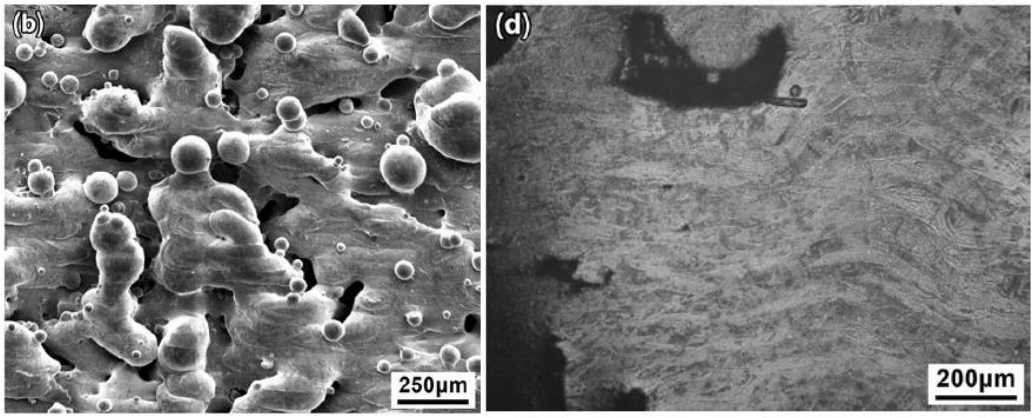

Figure 2-13: Microstructure of SLMed TiC/Al-alloy parts with different laser energy density. Left: low energy density. **Right:** high energy density.

On the other hand, nanocomposite powder prepared by another method, i.e., directly mechanical mixing of TiC powder (50 nm) and Ti powder (22.5 μm), was also processed for SLM[33]. However, the results of densification behavior and tribological properties from mechanical mixing powder were slightly worse than those from ball milled powder. It was believed that the method caused the TiC nanoparticles were only distributed around the Ti matrix powder surface. In this case, they believed the TiC nanoparticles exposed to the laser directly and underwent a simultaneous melting as the Ti powder, resulting in a melt instability in the molten pool. This instability induced a so called balling effect which decreased the densification level of the nanocomposite.

Nanoparticles will be pushed to the grain boundary after the laser processing. The TiC nanoparticles were distributed along the aluminum grain boundaries to form a ring structure after SLM[34]. Nanocomposite powders with Al-based metal matrix material and nanopowder (TiC) were prepared using ball milling method, followed by SLM process. Results showed that the ring-structured TiC reinforcement with a regular distribution was formed along the grain boundaries of the matrix with increasing energy density, as shown in Figure 2-14. It was believed that Marangoni flow induced capillary forces for liquid flow, resulting in a torque around the particle. In other words, Marangoni flow tends to rotate the TiC nanoparticles in the molten pool, providing a possibility to rearrange the TiC nanoparticles distribution along the grain boundaries.

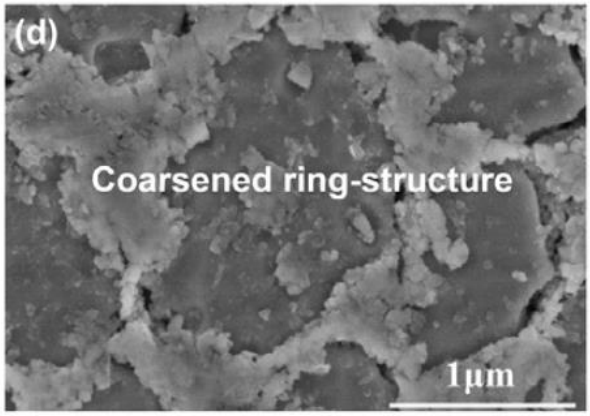

Figure 2-14: Ring-structure TiC reinforcement were distributed along with the grain boundaries of the Al-base matrix

2.4 Effects of nanoparticles on Nanocomposite material

2.4.1 Thermophysical properties

2.4.1.1 Heat Capacity

Heat capacity or thermal capacity equals to the ratio of the heat added to or removed from an object to the resulting temperature change[132]. The heat capacity of a material is a function of its phase or structure. Therefore, adding nanoparticles into matrix can modify the microstructure and

thus potentially tune the heat capacity of the material. Nelson et al. and Tiznobaik et al. studied the effects of nanoparticles on heat capacity of different material systems including molten slats and polymers[133,134]. The results obtained from electron microscopy showed that the heat capacity could be significantly increased because the nanoparticles modified the microstructures of the molten salts, resulting in the contribution of the enhancement of the heat capacity}[134]. Ma et al. theoretically predicted and experimentally measured the specific heat capacity of Al_2O_3/Ni nanocomposite[21]. The measurements were conducted by differential scanning calorimetry (DSC). The experimental results of specific heat measurements at room temperature showed a large difference from the predicted results. It was believed that the introduction of Al_2O_3 into Ni matrix does not significantly modify the specific heat in this study.

2.4.1.2 Thermal Conductivity

Thermal conductivity of a material could be modified by adding nanoparticles with different type, size, geometry, concentration and so on. Recent studies showed that incorporation of nanoparticles into matrix has performed either enhance or reduce thermal conductivity of the matrix[135-137]. For the enhancement of thermal conductivity, if the reinforced nanoparticles themselves have higher carrier (electrons and holes) concentration than that of base matrix material, adding nanoparticles inside to that matrix is possible to increase the overall carrier concentration of the material, resulting in a higher effective thermal conductivity of the matrix[135]. On the other hand, reducing the thermal conductivity below the base matrix by nanoparticles was also possible[136-138]. Scattering of electrons and phonons were performed due to the introduction of nanoparticles. A material with different wavelengths of phonon can contribute different amount of thermal conductivity. Short wavelength phonons in the material can be efficiently scattered by the small impurity atoms, while mid-long wavelength phonons are less scattered and can still able to

transport heat, thereby contributing to the heat conduction of the material[138-140]. Therefore, by incorporating nanoparticles with larger characterize length than that of impurity atom into matrix, mid- and long-wavelength phonons are additional scattered by the nanoparticles, significantly reducing the thermal conductivity which is lower than the base matrix. A schematic of carrier transport is shown in Figure 2-15[138]. Ma et al. theoretically predicted and experimentally measured the thermal conductivity of Al_2O_3/Ni nanocomposite[21]. The predicted model suggested that with extreme small size of nanoparticles the thermal conductivity can be significantly decreased because of the scatting of energy carriers and higher thermal interfacial resistance. The experimental results showed that the thermal conductivity of the Al_2O_3/Ni nanocomposite was decreased as the concentration of nanoparticles increased.

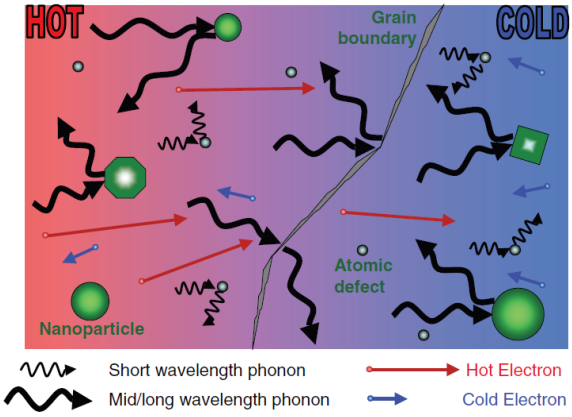

Figure 2-15: Schematic of phonon scattering mechanisms. Nanoparticles and grain boundaries play an effective role in scattering mid- and long-wavelength phonons

2.4.1.3 Viscosity and Surface Tension

Measuring the viscosity and the surface tension of molten metal matrix nanocomposites (MMNCs) accurately have been a long-standing challenge probably due to the high processing temperature of the metal. It is highly possible that adding nanoparticles into a material can enhance its viscosity. Extensive experimental studies have shown that nanofluids containing nanoparticles

possess higher viscosity than their base fluids, which give us a fundamental understanding on the effects of nanoparticles on viscosity of the nanofluid. Corcione et al. proposed an empirical correlation based on a large amount of experimental results[141]. Various nanoparticles (e.g., titania, silica, alumina, and copper) with size from 25 nm to 200 nm combined with different base fluids (e.g, ethylene glycol, propylene, ethanol, and water) were summarized. The fractions of nanoparticle are from 0.01 vol. % to 7.1 vol. %. Eventually, the experimental-fit correlation is shown:

$$\frac{\mu_{eff}}{\mu_f} = \frac{1}{1 - 34.87(d_p/d_f)^{-0.3}\varphi^{1.03}} \quad \textbf{(2-1)}$$

,where μeff the effective dynamic viscosity of a nanofluid, μf the dynamic viscosity of the base fluid, and dp the nanoparticle diameter. The df is the equivalent diameter of the base fluid molecule which can be expressed:

$$d_f = 0.1\left(\frac{6M}{N\pi\rho_f}\right)^{1/3} \quad \textbf{(2-2)}$$

,where M the molecular weight of the base fluid, N the Avogadro number, and ρf the mass density of the base fluid.

Eq. (2-1) clearly shows that the size, volume fraction of nanoparticles play an important role in the viscosity of the nanofluid. The effective viscosity of the nanofluid increases as the size of nanoparticle decreases and the volume fraction increases for a given base fluid.

On the other hand, surface tension is important in laser additive manufacturing since it is the driving force for melt pool flows. The effect of nanoparticles on surface tension (vapor-liquid interface) is complex and relative undeveloped[142-144]. Previous study showed that adding Bi_2Te_3

nanoparticles with different concentration and size into aqueous nanofluids is able to modify the surface tension of the liquid. The measurements of the effective surface tension were decreased greater than 50%[142].

However, above discussions were based on other material systems, which may not suitable for the case of MMNCs. Ma et al. experimentally measured the effective viscosity and surface tension of Al_2O_3/Ni nanocomposite simultaneously using oscillation drop method[22]. The experimental results showed that the adding nanoparticles into base material can increase the viscosity but decrease the surface tension of the MMNCs. It was explained as the solid nanoparticles inside the base material increase the viscosity and the introduced nanoparticles reduce the metallic bond of the base matrix, resulting in the reduction of the surface tension.

2.4.2 Electrical properties

Electrical conductivity is a function of the product of carrier density and the carrier mobility. Recent studies show that presence of nanoparticles can either suppress or enhance the electrical conductivity depending on nanoparticle radius (size less than 5 nm), volume fraction and band offset[139,145-148]. Results show that over 1% volume fractions of nanoparticles produce multiple scattering effects which significantly affect electron transport, thereby decreasing the electrical conductivity[146]. On the other hand, electrical conductivity can be increased if nanoparticles with small size could scatter phonons, but at the same time does not significantly shorten the mean free path of electrons (MFP_e), and could contribute free electrons/holes, i.e., ionized, to the matrix[139]. The fundamental reason behind the synergic effect of the concentration, geometry, size, and type of nanoparticles on the electrical conductivity of the composite is extremely complicated and not well understood.

The primary difficulty for electron transport prediction is that the presence of nanoparticles result in the characteristic lengths between nanoparticles and bulk matrix material are shorter than the electron de Broglie wavelength[149], meaning that the prediction by standard analysis using Boltzmann equation may not accurate. Some of important characteristic lengths are illustrated in Figure 2-16, which shows a schematic image of a nanocomposite with electron wavelength, grain size, and mean free path. Additional scattering of carriers (i.e., multiple scattering) occurs at internal interface within matrix due to the introduction of nanoparticles, leading to the mean free path of electron is smaller than its wavelength. As a result, some predictions from Boltzmann equation may give inaccurate theoretical analysis because the requirement of Boltzmann equation is the mean free path of electron should much larger than the wavelength. While some theoretical predictions of the influence of the particles on effective electrical conductivity in composite have been developed[18,150,151] reliable predictions of electrical conductivity in nanocomposite still questionable. Hence, it is necessary to have more careful examination of carrier transport in nanocomposite material.

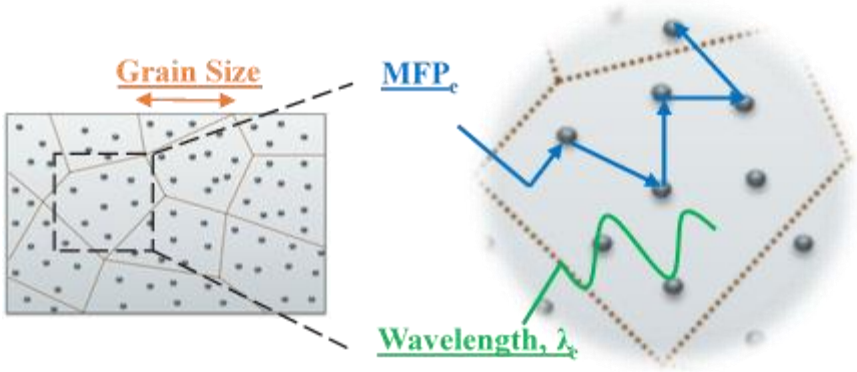

Figure 2-16: Schematic of a nanocomposite reinforced by nanoparticles along with important characteristic lengths

It is clear that the scattering factor and size of nanoparticle play an important role in electron transport that critically affects electrical conductivity of the composite material. If the MFP_e is much smaller than the characteristic length of each nanoparticles inside the matrix and the nanoparticle sizes are smaller than the MFP_e, the nanoparticles could be considered as scattering centers and the leakage of the electron wave function inside the nanoparticles could be ignored[152], while if the size of nanoparticles is small and the distance between the nanoparticles is smaller than MFP_e, multiple scattering of the carries becomes an important issue. As mentioned before, once the MFP of electron becomes comparable or smaller than the electron wavelength, the validity of Boltzmann equation becomes questionable and more powerful tools such as non-equilibrium Green's functions are required to take account of electron wave effects in the nanocomposite[149]. At this point, detailed understanding of multiple scattering of electron transport in nanocomposite is still not well developed and thus there is a great need for studying electron transport in more detail.

2.4.3 Strengthening Effect

The strengthening effects of nanoparticles in MMNCs include Orowan strengthening, dislocation density difference due to mismatch of thermal expansion (CTE) coefficient, load bearing transfer and Hall-Petch strengthening effect. The strengthening effects involved in the Nanocomposite are discussed below.

2.4.3.1 Orowan strengthening

Orowan strengthening plays a significant role in MMNC because the space of the nanoparticles inside the matrix are very close, which could impede the movement of dislocations. Previous studies show that highly-dispersed nanoparticles with a size smaller than ~100 nm can

considerably raise creep resistance, even with only a small fraction (<1%)[115,153]. The Orowan-Ashby equation can be used to describe the Orowan strengthening ($\Delta\sigma_{Orowan}$) effects[154].

$$\Delta\boldsymbol{\sigma_{Orowan}} = \frac{\mathbf{0.13}\boldsymbol{G_m b}}{\boldsymbol{\lambda}} \boldsymbol{ln}\frac{\boldsymbol{r}}{b} \quad \textbf{(2-3)}$$

$$\boldsymbol{\lambda} \approx \boldsymbol{d_p}\left[(\frac{\mathbf{1}}{\mathbf{2}\boldsymbol{V_p}})^{\frac{\mathbf{1}}{\mathbf{3}}} - \mathbf{1}\right] \quad \textbf{(2-4)}$$

where r is the particle radius, and λ is the interparticle spacing shown in Equ. (2-4)[155], d_p is particle diameter, **b** is the Burger's vector and G is the matrix shear modulus.

2.4.3.2 CTE Mismatch

During the material processing, the formation of geometrically necessary dislocations (GND) are occurred because of the mismatch in coefficient of thermal expansion (CTE) between the reinforcements and the metal matrix. As a result, these enhanced density dislocation are able to contribute the strength of the MMNCs. This strengthening effect can be described[156]:

$$\Delta\boldsymbol{\sigma_{CTE}} = \sqrt{\mathbf{3}}\boldsymbol{\beta G} b\sqrt{\frac{\mathbf{12}\Delta\boldsymbol{\alpha}\Delta\boldsymbol{T}\boldsymbol{V_p}}{b\boldsymbol{d_p}}} \quad \textbf{(2-5)}$$

,where β is a constant, Δ α is the difference of the CTE between the hard particles and the matrix, ΔT is the temperature difference between testing and processing temperature. One thing should be noted that when the nanoparticles are too small, there are no enough strain can be generated and thus the CTE mismatch might be neglected[19].

2.4.3.3 Load Bearing Transfer

When an external load is applied, the load can be transferred from the soft matrix to the hard particles, contributing to the strengthening of the base matrix. This strengthening effect can

be predicted by a common used modified model[157]. The yield strength increment ($\Delta\sigma_{Load}$) due to load bearing transfer can be expressed as follow:

$$\Delta\boldsymbol{\sigma_{Load}} = \mathbf{1.5}\boldsymbol{V_p\sigma_m} \quad \textbf{(2-6)}$$

,where V_p is the volume fraction of particles and σ_m is the original yield strength of matrix.

A strong interfacial bonding between particles and matrix is necessary for the strong long bearing transfer, because only the strong interface allows the load to be transferred from soft matrix to hard particles for the strengthening.

2.4.3.4 Hall-Petch strengthening

The nanoparticles inside the MMNCs can be treated as pinning points, which can stop or inhibit the grain growth during recovery, recrystallization and heat treatment. As the concentration of nanoparticles is increased and the diameter of nanoparticles is decreased, the microstructure of the MMNCs can be further finer. This strengthening effect can be estimated by[156]

$$\boldsymbol{d_m} = \frac{\boldsymbol{4\alpha d_p}}{\boldsymbol{3V_p}} \quad \textbf{(2-7)}$$

,where α is a proportional constant, d_m is the average grain size.

The grain size has a significant influence on metal strength since grain boundaries can hinder the dislocation movement. The reason is that adjacent grains have different orientation, and the different orientation result the dislocations must change the orientation when moving from one grain into another grain. Therefore, it requires more energy for the dislocations to move to another

grain, resulting in the dislocations movement in a continuous slip plane can be prevented. This is the reason why a refined microstructure can have higher strength because of the grain refinement. The equation for describing the Hall-Petch strengthening effect is[158]

$$\Delta\boldsymbol{\sigma_{H-P}} = \boldsymbol{k}(\boldsymbol{d_m^{-\frac{1}{2}}}) \quad \textbf{(2-8)}$$

,where k is the strengthening coefficient, d_m is average grain size of matrix sample in the nanocomposite sample.

2.5 Effects of nanoparticles on LAM

2.5.1 Reflectivity

The laser reflectivity of metal powder bed in LAM has been intensively discussed by King et al[159]. However, the effects of nanocomposite powder reflectivity on LAM remain to be understood. It is of the key factors for LAM because the reflectivity directly determines the amount of energy the powder can absorb at the certain laser wavelength, i.e., 1060 μm, for common SLM. Adding nanoparticles into LAM process can modify the laser reflectivity of the matrix powder[89,126] due to the higher or lower reflectivity of the ceramic nanoparticles. The studies presented that the nanocomposite powder, e.g., 7 vol.% TiB_2/AlSi10Mg and TiB_2/Al3.8Cu1.3Mg, showed increased lase absorptivity compared to the pure matrix powder, which further benefits the LAM process window. More rigorous studies are necessary because the reflectivity measurements were obtained under room temperature, which is different from real laser processing temperature.

2.5.2 Thermal conductivity

The effective thermal conductivity of a loose powder bed is a critical factor for LAM. Yuan et al. proposed numerical models simulating the effective thermal conductivity of nanocomposite powder bed (AlSi10Mg mechanically mixed with 5 vol.% TiC nanoparticles) in SLM[35]. The

results from experimental data and the theoretical predictions indicate that the effective thermal conductivity of the powder bed is proportional to the thermal conductivity of gas trapped in the pores, and also relied on the powder size. Since the powder size in SLM is about several tens of micrometers, the effective thermal conductivity is of the order of five to ten times to the air[160]. This large difference results in the effectively thermal conductivity is mainly determined by the relative density of the powder bed and less by the powder.

2.5.3 Viscosity and surface tension

It would be difficult to measure the dynamic viscosity and surface tension of the molten pool of nanocomposite during LAM. From literature, the dynamic viscosity of the melt within the molten pool can be defined by[4]

$$\mu = \frac{16}{15}\left(\frac{m}{kT}\right)^{1/2}\gamma$$

,where m is the atomic mass, k the Boltzmann constant, T the temperature and γ the surface tension of the liquid. It is clear that the viscosity of the solid/liquid composite system is dependent on the processing temperature. The surface tension can be estimated by calculating the interfacial energy among solid-liquid, solid-vapor, and liquid vapor. However, the in-situ viscosity and surface tension of the molten pool during LAM are still difficult to obtain.

2.6 Summary

Laser additive manufacturing of typical metals have been reviewed. With proper process optimizations, some conventional materials, e.g., aluminum, titanium, stainless steel, superalloy, with reasonable properties could be obtained. However, a great number of challenges have arisen while exploring the potential workable metals and alloys to achieve desired properties. For example, it is extremely difficult to directly print conventional Al7075 or pure copper. Problems such as absence of porosities, poor surface morphologies or cracking have been observed due to

improper processing parameters (energy density, scanning patterns; powder thickness) or intrinsic nature of the materials (thermal conductivity or reflectivity), which deteriorates the resulting material performance.

Recently the idea of Metal Matrix Nanocomposite (MMNC) introduced to LAM would provide a new pathway to tackle the great challenge. MMNC has emerged as an important class of metallic material because it has a great potential to obtain significantly enhanced material properties such as electrical, physical, mechanical, and chemical properties. Various manufacturing methods have been introduced. Among all the methods, the fabrication of MMNCs via laser additive manufacturing has just emerged as a new research area.

Research progresses on typical additive manufacturing of nanocomposite were reviewed. The fabrication of polymer nanocomposite and metal matrix nanocomposite via additive manufacturing processes were introduced. Direct metal laser melting (DMLS) and selective laser melting (SLM) are the most popular laser additive manufacturing for fabrication of MMNC. So far, the base materials that have been experimented including pure Ti, TiAl alloys, iron, steel, Al alloys, and superalloy. Various nanoparticle reinforcements can be either introduced by ex-situ additions or produced by in-situ reactions. The nanoparticles include TiC, SiC, Al_2O_3, and intermetallics. Even though mechanical properties (e.g., hardness, strength, wear resistance) were successfully enhanced and demonstrated, there are still unresolved problems such as densification, chemical reaction and nanoparticle agglomeration. Nevertheless, little researches on improving the distribution and dispersion of nanoparticles have been reported.

Nanocomposite powders prepared by different methods have been introduced. These powders with different morphology result in different microstructures after LAM. Some studies experimentally proposed a processing map to improve the dispersion of nanoparticles but still lack

of fundamental understanding of particles interaction during the laser processing. Current reports are mainly focused on investigating the microstructure evolutions and improving the material properties. However, the underlining physics of the process was not well studied, especially the laser absorption of powders during laser additive manufacturing.

The effects of nanoparticles on material properties and LAM were reviewed in this chapter. While theoretical models were proposed from various studies to simulate the nanoparticle effects during the LAM process, more carefully experimental examination and rigorously study are still needed to validate the predictions. For example, nanoparticles could change laser-mater interaction (e.g., absorptivity), thermophysical properties (e.g., surface tension, viscosity, and thermal conductivity) of the matrix material during layer-by-layer laser processing. These modified properties will affect the resulting performance of deposited material such as microstructure and mechanical properties.

In summary, this chapter reviews conventional materials successfully additively manufactured, followed by presenting a great number of challenges arisen while laser printing metals or metal alloys. MMNCs have been introduced to tackle the challenges in LAM but most studies mainly investigated the resulting mechanical properties. There is a great need to obtain the knowledge of the nanoparticle effects on laser absorption during laser processing. It is also necessary to understand how to successfully laser deposit materials with well nanoparticle dispersion and distribution. The knowledge will provide us remarkably valuable insights and guidance on how to improve the mechanical performance during LAM of MMNCs.

CHAPTER 3 FABRICATION OF MMNC POWDERS

3.1 Experimental method

The metal matrix nanocomposite (MMNC) powder is one of the key factors for a laser melting process to obtain a desired component. From literature, common MMNC powder preparation techniques (e.g., direct mixing, ball milling, and gas atomization) are used to obtain the desired final powder shape and size to ensure that the ceramic nanoparticles were well mixed with matrix powders. In this study, to obtain a homogenous mixture of the initial powders before laser processing, a novel self-assembly method described in the previous report[127] was applied to produce the MMNCs powders. Two fabrication techniques, i.e., ultrasonic processing and mechanical mixing, are used to produce MMNCs powders for Laser Additive Manufacturing (LAM). The techniques were chosen because of their low cost, simple setup, potential scalability and capability of high volume nanoparticle incorporation.

3.1.1 Nanoparticle self-assembly with assistance of ultrasonic processing

3.1.1.1 Fabrication of aluminum matrix nanocomposite (AMNC) powders

To produce the AMNC powders, premixing of NaCl and KCl salt powders (from Fisher Chemical, ≥99.0%), TiC nanoparticles (with an average size of 40-60 nm, from US Research Nanomaterials, ≥99.0%) and Al microparticles (with an average size of 20 μm, from Sigma-Aldrich, ≥99.0%) was carried out in a mechanical shaker for 30 mins. Then, the mixture was dehydrated in a vacuum furnace at 120 °C for 10 mins. The mixture was melted at 820 °C under argon protection in a graphite crucible with an outside diameter of 58 mm and a height of 88 mm. An ultrasonic niobium probe with a diameter of 12.7 mm and a length of 92 mm was then inserted 6 mm deep into the molten liquid, processing the melt for 15 mins before the samples were taken out of the furnace and cooled down in air. The cooled samples were then repeatedly dissolved four

times in 400 mL distilled water in an ultrasonic bath for 30 mins. The solution was filtered through filter papers with a mesh size of 2.7 μm (Whatman plc) using vacuum filtration under room temperature for 20 mins. Eventually the AMNC powders were obtained and collected from the top of the filter papers. These powders were dried and dehydrated in a vacuum furnace for 10 mins at 150 °C before their use in laser experiments. To control the nanoparticle loading in the AMNC powders, we tuned the volume ratio, *x*, of the TiC nanoparticles to the Al microparticles. The volume ratio between the powder mixture and the salt was maintained constant at 3%. For the AMNC powder with a volume ratio factor of x=0.25, this study mixed 1.57 g TiC nanoparticles, 3.6 g Al micro particles, 27.1 g NaCl, and 34.6 g KCl. For AMNC powder with a volume ratio factor of x=1, 4.39g TiC nanoparticles were mixed 2.4 g Al, 27.1 g NaCl, and 34.6 g KCl. Ultrasonic amplitude of 30 μm and 45 μm were used for processing of the materials with x=0.25 and x=1, respectively.

3.1.1.2 Fabrication of aluminum alloy (AlSi12) matrix nanocomposite powders

The fabrication procedures for AlSi12 matrix nanocomposite powder are similar to the processing steps of AMNC powders. NaCl and KCL powder salt were first mixed with $AlSi_{12}$ micro particles (with average size of 20 μm, from READE advanced materials) and TiC nanoparticles (with an average size of 40-60 nm, from US Research Nanomaterials, ≥99.0%) for 4 hours using mechanical shaking. After dehydration by vacuum oven, the ultrasonic processing was used to process the melt under a temperature of 820°C for 15 mins under argon protection. The samples were then cooled down to room temperature in a fume hood under air environment. Nanocomposite powders were collected on the filter papers after the washing process, i.e., ultrasonic bath followed by vacuum filtration. In this study, the AlSi12 matrix nanocomposite powders with different volume ratio of x (0.05 and 0.25) were designed for LAM.

3.1.2 Nanoparticle self-assembly with assistance of mechanical mixing

3.1.2.1 Fabrication of aluminum matrix nanocomposite (AMNC) powders

While the AMNC powders produced using ultrasonic processing have a full coverage of nanoparticles and excellent nanoparticle dispersion and distribution inside the matrix, the technique is limited to a small quantity fabrication due to its system setup and operation temperature. Thus, a novel scalable manufacturing method, i.e., mechanical mixing, is proposed to overcome these challenges. This method consisted of a high speed stirring apparatus with an assistance of molten salt overcomes the limitation of scalability. Furthermore, the advantages of this method include but not limit to its low cost, simplicity, and flexibility. During stirring, a rotary blade (graphite or stainless steel) with a certain complex shape forms a vortex in the melt. A high shear rate caused by stirring the melt leads to a good dispersion and distribution of nanoparticles in the molten salt. Nanoparticles were then self-assembled at the surface of the molten metal droplets and effectively distributed into the micro droplets (minor phase in this case), driven by the minimization of free energy in the immiscible liquid system. A schematic image of the system setup is depicted in Fig. 3-1.

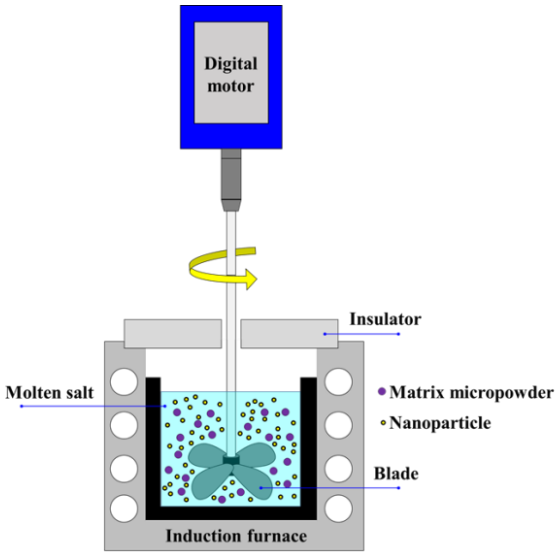

Figure 3-1: Schematic of mechanical mixing mechanism

To show the scalability of powder manufacturing, aluminum metal matrix nanocomposite (AMNC) powders with a mass of 50g were initially demonstrated. A premixing of NaCl and KCl salt powders (from Fisher Chemical, ≥99.0%), TiC nanoparticles (with an average size of 40-60 nm, from US Research Nanomaterials, ≥99.0%) and Al microparticles (with an average size of 20 μm, from Sigma-Aldrich, ≥99.0%) was carried out in a mechanical shaker for 4 hours. Al matrix powders of 20 μm (Sigma-Aldrich, ≥99.0%) were mixed with TiC nanoparticles (40-60 nm, from US Research Nanomaterials) with a volume ratio of 1 to 4. Two different volume fractions of the aluminum powders to the salt, i.e., 10 vol.% and 20 vol.%, were designed. Then, the mixture was dehydrated in a vacuum furnace at 120 °C for 10 mins. The graphite blade with a diameter of 2inch jointed with a titanium shaft with a diameter of 1/4inch and a length of 50 cm was securely clamped by the chunk of an ultra-torque digital stirrer (BDC1850, Caframo Canada) before the processing. The mixture was melted at 820 °C under argon protection in a graphite crucible with an outside diameter of 5.5 inch and a height of 6 inch. The graphite blade was then inserted one-third deep into the molten liquid from the bottom of the crucible, stirring the melt with a rotational speed of 1800 rpm for 15 mins before the sample was taken out of the furnace and cooled down under the protection of argon environment. The cooled samples were then repeatedly dissolved four times in 1000 mL distilled water in an ultrasonic bath for 30 mins. The solution was filtered through filter papers with a mesh size of 2.7 μm (Whatman plc) using vacuum filtration under room temperature for 20 mins. Eventually the AMNC powders with approximately 50g were obtained and collected from the top of the filter papers. These powders were dried and dehydrated in a vacuum furnace for 10 mins at 150 °C.

3.1.2.2 Fabrication of Copper matrix nanocomposite powders via wet mechanical mixing

Mechanical mixing is a potential candidate for copper nanocomposite powder fabrication. The graphite blade can sustain high temperature above 1100^0C without potential chemical reaction

during the stirring process. NaCl and KCL powder salt were first mixed with Cu micro particles (with average size of 20 μm, from Sigma-Aldrich, 99%*)* and tungsten carbide (WC) nanoparticles (with an average size of 150-200 nm, from US Research Nanomaterials, 99.9%) for 4 hours using a mechanical shaker. The volume ratio, x, of the WC nanoparticles to the Cu microparticles were designed as 0.1 and 0.25, respectively. The volume ratio between the powder mixture and the salt was maintained constant at 1%. The mixture was first melted at 800°C, i.e., melting point of NaCl, under argon protection in a graphite crucible with an outside diameter of 58 mm and a height of 88 mm. The standard graphite blade was then inserted one third deep into the molten liquid, stirring the melt with a speed of 1800 rpm till the melt temperature reached to 1150°C, followed by maintaining the stirring with 15 minutes. After processing of 15 minutes, the furnace was turned off while keeping the high speed stirring till the temperature of melt cooled down to 1000°C. The sample was taken out of the furnace and cooled down in air environment, followed by same cleaning procedures as mentioned in the section of AMNCs powders. The brass sieves with different mesh sizes of #35, #140 and #325 (McMaster-Carr) were applied to separate multiple particle sizes. Eventually, the powders with desired size were collected for LAM experiment.

3.1.2.3 Fabrication of copper matrix nanocomposite powders via dry mechanical mixing: The nanocomposite powders, Cu-WC (x=0.66), introduced in this subsection were mainly produced via a labmate, Mr. Gongchen Yao, for the following laser additive manufacturing experiment. Unlike "wet" mechanical processing, the "dry" mechanical mixing means the mixture was only processed slightly above the melting point of copper without any external mechanical stirring. To fabricate the Cu-WC nanocomposite powders, pure Cu powders (Sigma-Aldrich, 14-25 μm, 99%) and WC nanoparticles (US Research Nanomaterials, 150–200 nm, 99.9%) were mechanically mixed with a volume ratio of 3 to 2 using mechanical shaking (SK-O330-Pro) for 10 mins. The volume ratio, x, of the WC nanoparticles to the Cu microparticles were designed as 0.66, which corresponds to 40 volume percent of WC in the Cu matrix. The mixture was heated to 1230 °C in an induction heater under argon protection, followed by maintaining the temperature for 30 min before cooling in the furnace, after which the material had a loose structure and can be easily grinded to obtain nanocomposite powders. To remove free WC nanoparticles which were not incorporated into Cu, the powders underwent three rounds of soaking in DI water, during which free WC nanoparticles were poured out with water. The Cu-WC nanocomposite powders (x=0.66) were ready for LAM experiment after drying in a vacuum oven overnight.

3.1.3 Characterization

Characterization of micro/nano-structures of powder samples was carried out using scanning electron microscopy (SEM, Supra 40VP, ZEISS), energy dispersive X-ray spectroscopy (EDS/EDX) and focused ion beam FIB, Nova 600, FEI). EDS analysis was used to determine the phases and the distributions of each element at the surface or interior of nanocomposite powders. To reveal internal structure of MMNC powders, samples were characterized using two different methods. First, focused ion beam (FIB) was used to selectively ion-etch the powder samples,

followed by obtaining SEM images. Second, the powder samples were first mounted in epoxy resin for the standard grinding/polishing procedures. Grinding was done with 240, 400, 600, 800 and 1200 grit sand papers, followed by polishing of the samples with 1-μm Al_2O_3 polishing compounds. SEM characterization was conducted to reveal the cross sectional image of the powders. Powder distribution was measured using a light scattering particle analyzer (LS), followed by comparing with the powder size observed from SEM images. The reflectivity of powders at specific wavelengths was captured via an UV3101PC spectrophotometer (SHIMADZU Cop.) A wavelength range from 250 nm to 2500 nm was scanned with a spectral resolution of 2.0 nm. A standard barium sulfate $BaSO_4$ plate was used to perform a baseline correction over the required wavelength range to ensure a 100% reflectance. Powder samples were then mounted and sealed on a powder sample holder packed with the accessory barium sulfate $BaSO_4$ for the reflectance measurement. The kinetic measurement mode was applied to record and analyze the reflectivity using multifunctional UVProbe software (SHIMADZU Cop.). The powders without nanoparticles reinforcement were also measured for comparison purpose. Three LS and reflectivity measurements were repeated for each sample, so the average value and the standard deviation were calculated.

3.2 Experimental results

In this section, in depth characterization of nanocomposite powders will be introduced and discussed. The morphology, size distribution, and microstructure of the powder will be presented. Light scattering (LS) particle analyzer (LS13 320, Beckman Coulter) was used to determine the size distribution of the nanocomposite powders. Scanning Electron Microscopy (SEM, Supra 40VP, ZEISS) and focused Ion Beam (FIB, Nova 600, FEI) were utilized to study the surface and the inner microstructures of the spherical nanocomposite powders. The nanoparticle effects on

laser reflectivity at wavelength of 1070 nm (i.e., the laser wavelength used in this study) will be investigated by A UV3101PC spectrophotometer (SHIMADZU Cop.). Detailed information and results will be presented at the following sub-sections.

3.2.1 AMNCs powder produced via ultrasonic processing

3.2.1.1 Morphology, internal microstructure and size distribution

By simply tuning x, the volume ratio between TiC nanoparticles and liquid aluminum, AMNC powders with different TiC loadings (e.g., x=0.25; and x=1) can be fabricated. As shown in Fig. 3-2, the AMNC powders (x=0.25) are spherical with an average size of 11.3 ± 7.2 μm (See size distribution section). Most of the TiC nanoparticles assemble at the surface of the Al droplets at the beginning, as shown in Fig.3-2c, because of its favorable energy state.

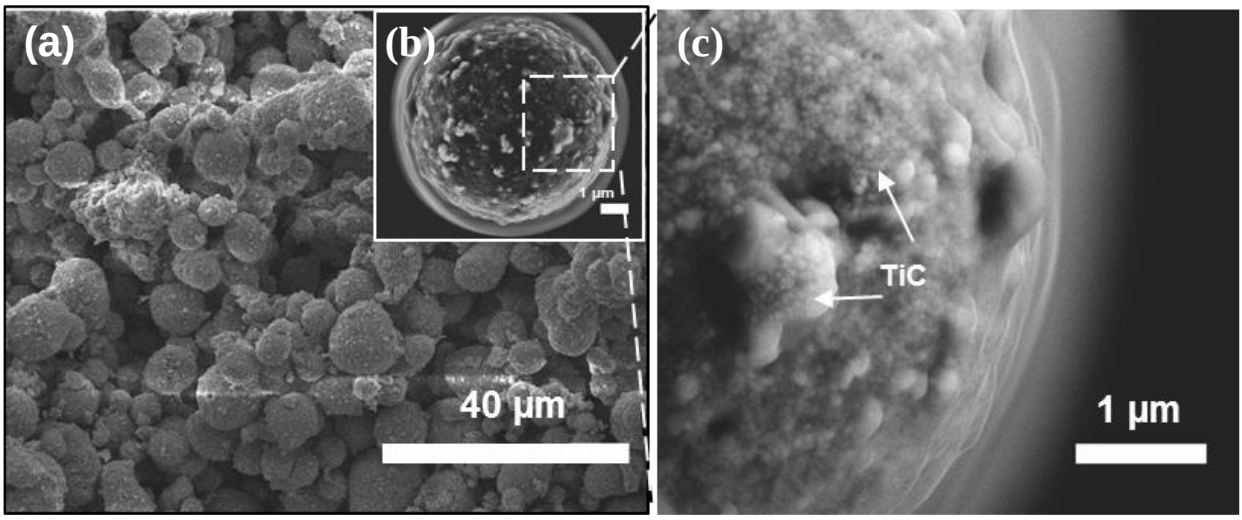

Figure 3-2: Morphology and microstructure of aluminum matrix nanocomposite (AMNC) powders. a, b, SEM images of AMNC powders with x=0.25. **c,** Magnified image of **b,** showing TiC nanoparticles coated on the surface of an Al micro particle.

As the x increases, the favorable energy state is not available for the additional TiC nanoparticles; hence the nanoparticles are forced to enter the Al droplets. The experiment was conducted at 820 °C, at which the TiC is chemical stable with Al and the wetting angle of TiC/Al

is less than 70°[161], using ultrasonic processing. To reveal the distribution and dispersion of TiC nanoparticles in the matrix powders, the samples were mounted on a silicon wafer, tilted to 52° and then etched by FIB with gallium ions. The images of the 52° tilted cross-sectional SEM powders were acquired to reveal the distribution and dispersion of the nanoparticles. The cross-section images in Fig. 3-3a and Fig.3-3b indicate that the TiC nanoparticles (shown as gray spots) were effectively pushed into and distributed inside the core of the Al powders. It is believed that spherical particles enable a better flowability and a higher packing density than irregularly shaped particles for LAM[85].

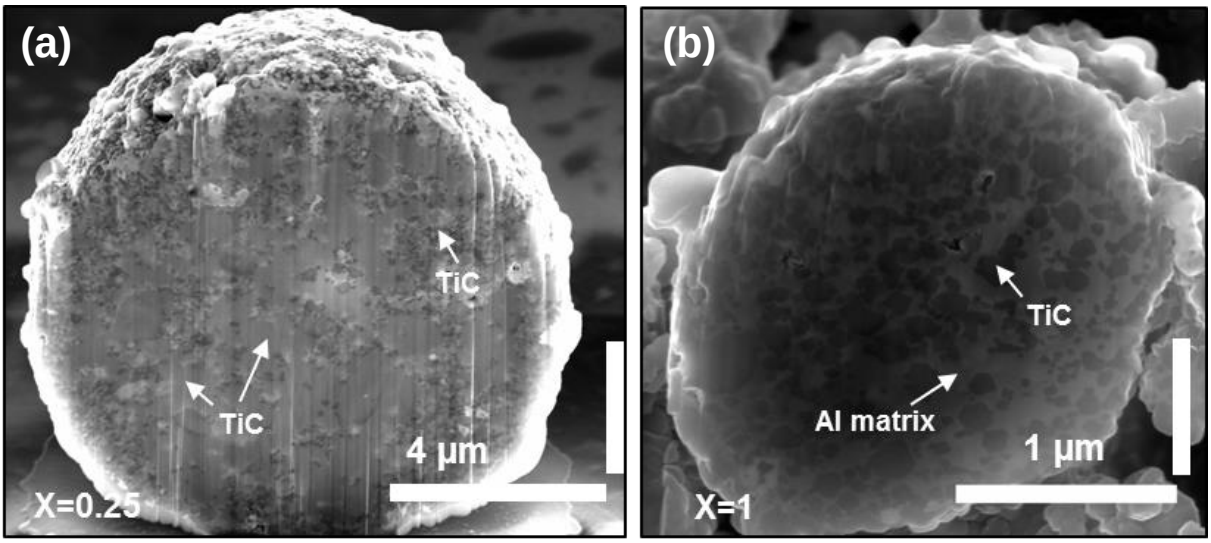

Figure 3-3: Internal microstructure of aluminum matrix nanocomposite (AMNC) powders. a, **b**, SEM images of the cross sections of samples with x=0.25 and x=1 respectively. The AMNC powders (x=1) have a higher loading of embedded TiC nanoparticles than the AMNC powders (x=0.25).

The size distribution of AMNCs powders were first characterized via SEM, as shown in Fig. 3-4(a) and Fig. 3-4(b). Light scattering (LS) particle analyzer (LS13 320, Beckman Coulter) were then used to validate the size distribution of the AMNCs powders, as shown in Fig. 3-4c and Fig. 3-4d. The powder distribution results from LS show the AMNC powders (x=0.25 and x=1)

have an average size of 11.3 ± 7.2 µm and 5.9 ± 4.6 µm, respectively, which the size ranges are comparable to the size observed from SEM images (Fig. 3-4a and Fig. 3-4b).

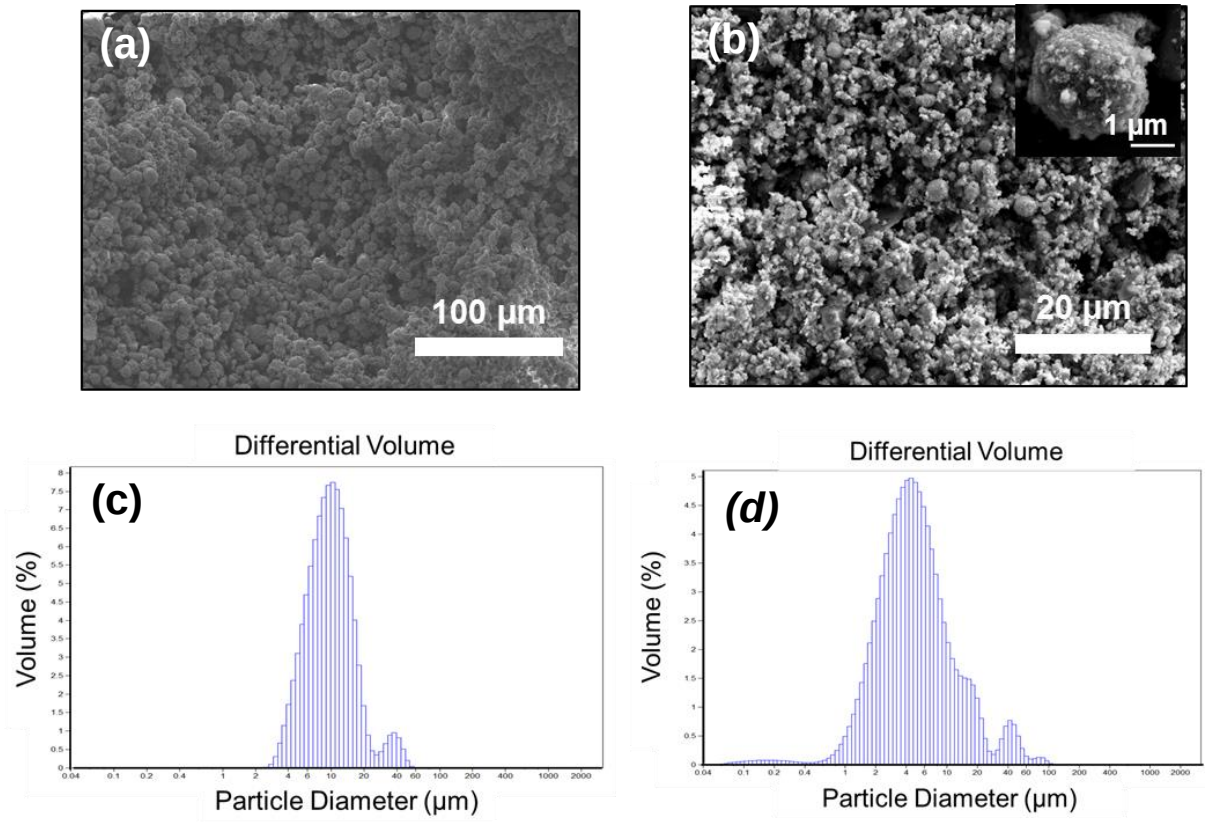

Figure 3-4: Size distribution of AMNCs powder. SEM images of AMNC powders from different volume ratios of **a**, x= 0.25 **b,** x= 1. **c**, **d**, Size distribution of AMNC powders for x=0.25 and x=1, respectively.

3.2.2.2 Laser Reflectivity

The surface-coated and uniformly dispersed TiC nanoparticles inside the AMNC powders can enhance laser beam absorption because of the high absorptivity of non-oxide ceramic nanoparticles[21,22,89]. The reflectivity measurements, as shown in Fig. 3-5a to Fig. 3-5b, illustrate that the reflectivity of AMNC powders with *x*=0.25 and *x*=1 are 14.58 ± 0.46% and 7.46 ± 0.47%, respectively, at the laser wavelength of 1070 nm for the LAM process in this study. The reflectivity

of AMNC powder is significantly lower than that of pure aluminum powders (58.12 ± 0.81%), which enhances the energy efficiency of laser processing by almost one order of magnitude.

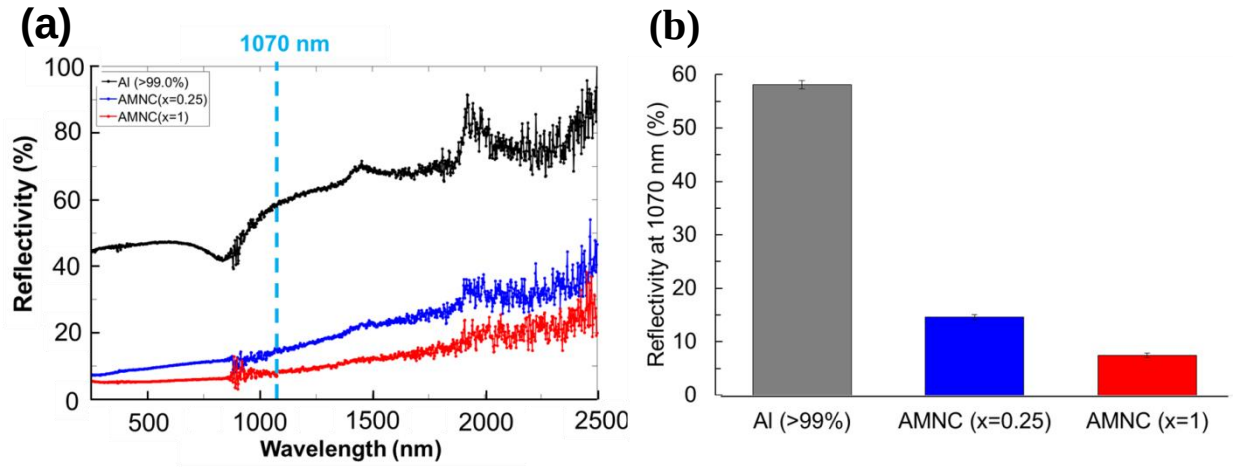

Figure 3-5: Reflectivity of aluminum matrix nanocomposite (AMNC) powders. a, Reflectivity of aluminum powders without and with nanoparticles. The dashed vertical line indicates the laser wavelength at 1070 nm. **b,** Comparison of the reflectivity at the wavelength of 1070 nm for aluminum powder samples with and without nanoparticles**.**

3.2.2 AlSi12-TiC powders produced via ultrasonic processing

3.2.2.1 Morphology, internal microstructure and size distribution

To demonstrate the powder fabrication method, i.e., ultrasonic processing, can be readily extended to another aluminum alloy powder system for LAM, the commercial gas atomized AlSi12 micropowders were selected. The volume ratio of x=0.05 and x=0.25 were designed (See section 3.1.1.2). Figure 3-6a and Fig.3-6b show the $AlSi_{12}$-TiC (x=0.05) nanocomposite powders with a spherical shape have an average size of about 11.07±3.64 µm, as confirmed by LS results and SEM images. In addition, it can be seen that these spherical AlSi12-TiC nanocomposite powders are fully coated with TiC nanoparticles, as shown in the white spots and arrows in Fig. 3-6c and Fig. 3-6d, using ultrasonic processing method. To further reveal the internal structure, the

powders were embedded in an epoxy resin for standard grinding and polishing procedures (See section 3.1.3), followed by SEM characterization. A cross-sectional image (Fig.3-6b) reveals that the TiC nanoparticles were effectively pushed into the AlSi12 micropowders, showing that even with only small amount of nanoparticles in the Al matrix (about 5vol.%), i.e., x=0.05, the molten salt are still able to free the oxide layer of aluminum droplet and push the TiC nanoparticles into the Al matrix.

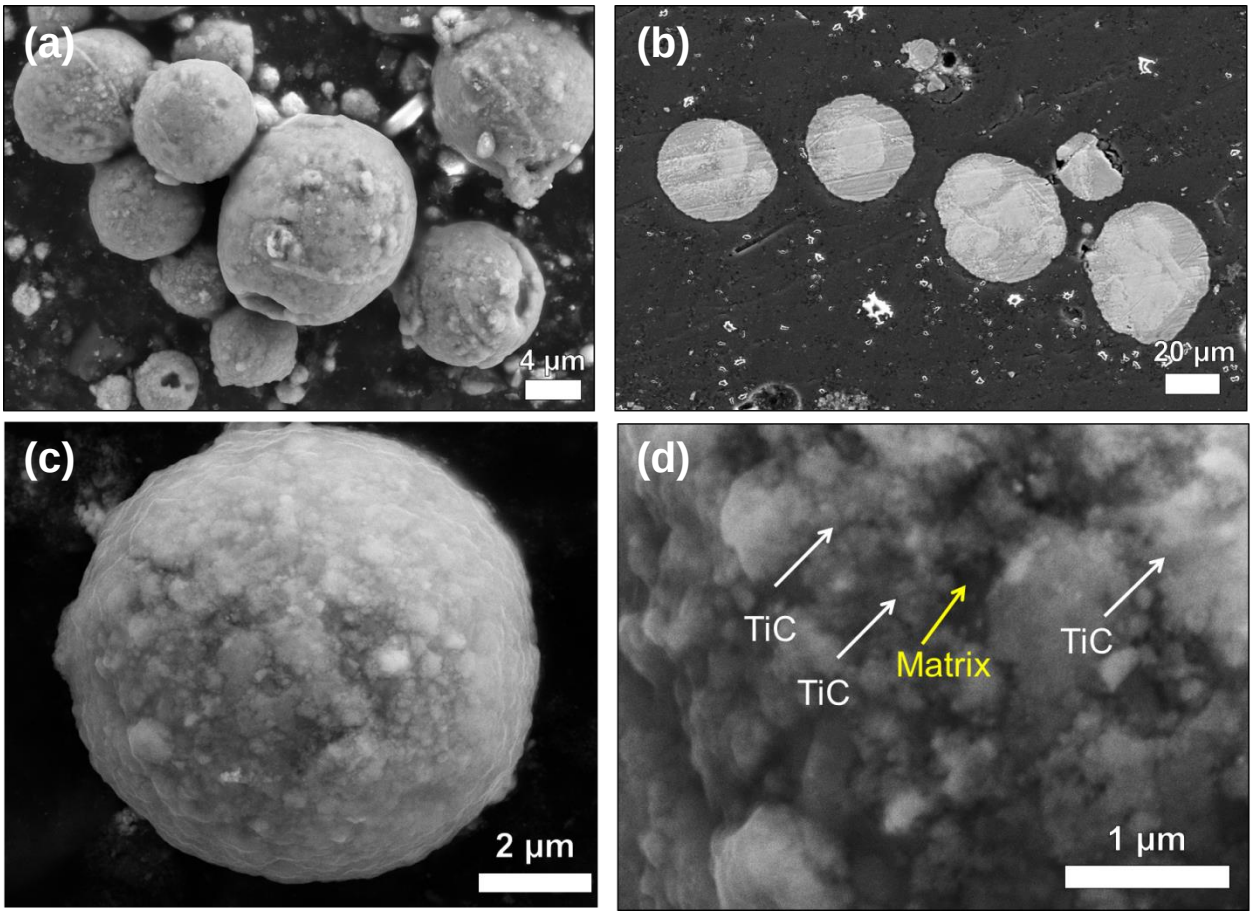

Figure 3-6: Morphology and microstructure of AlSi12-TiC nanocomposite powders. a, SEM images of AlSi12-TiC (x=0.05) powders. **b,** Internal microstructure. **c**, SEM image of a spherical $AlSi_{12}$-TiC powder **d**, Magnified image of **c**, showing TiC nanoparticles was coated on the surface of an AlSi12 micro particle.

Similarly, $AlSi_{12}$-TiC (x=0.25) nanocomposite powders shows spherical powder morphology as the powders of $AlSi_{12}$-TiC (x=0.05) and AMNCs. A SEM image (Fig. 3-7a) reveals that the spherical AlSi12-TiC (x=0.25) powders have an average size of 15.84 ± 6.2 µm. The internal microstructure characterization (Fig. 3-7b and Fig. 3-7c) shows that the TiC nanoparticles are distributed in AlSi12 matrix without forming large clusters. A closed examination (Fig. 3-7c) indicate the Si phase (yellow arrows) was refined by TiC nanoparticles (white arrow), which the elements were confirmed by EDS analysis. The size of Si phase was refined to nanoscale (about 500 nm) after introducing the TiC into the matrix powder.

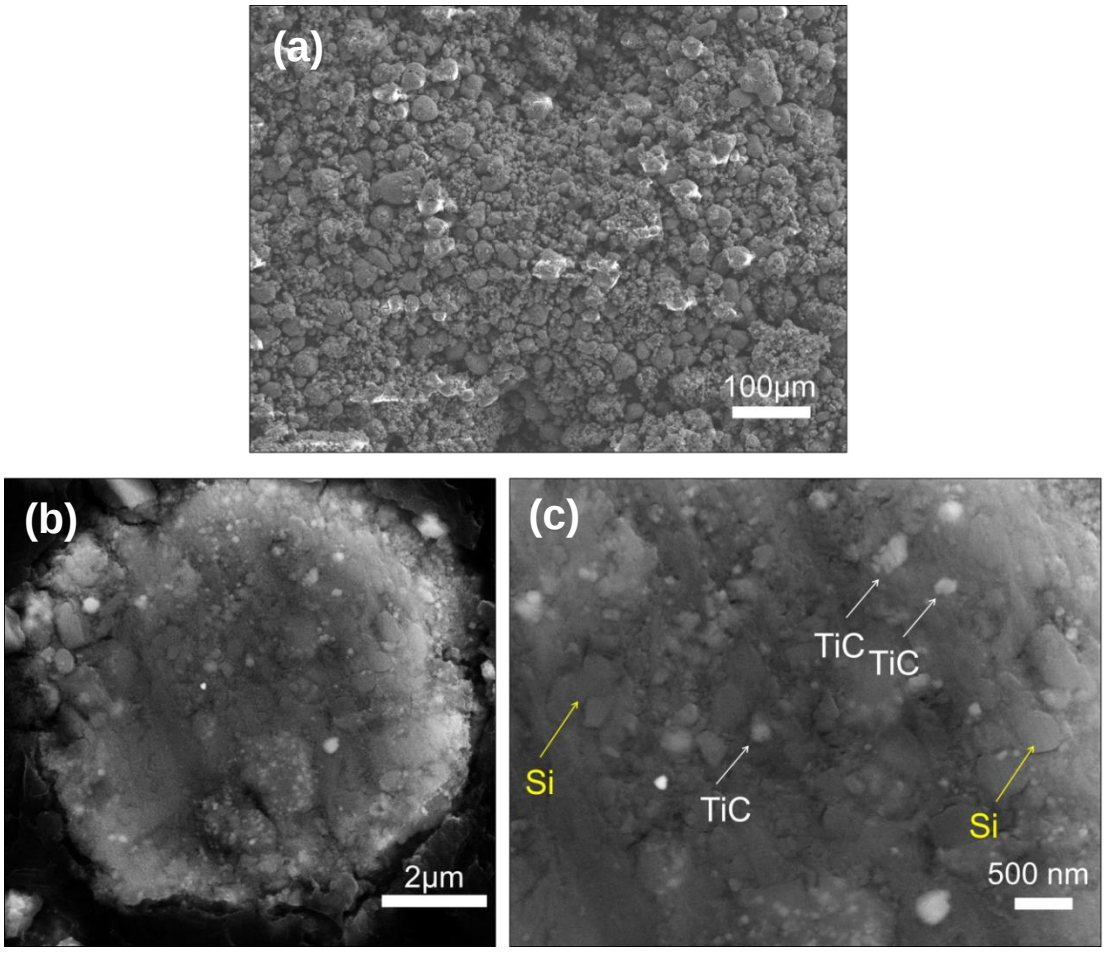

Figure 3-7: **a,** SEM image of AlSi12-TiC (x=0.25) powders **b,** Internal microstructure of AlSi12-TiC (x=0.25) powders **c,** Magnified image of **b**.

3.2.2.2 Laser Reflectivity

The reflectivities of AlSi12 powders without and with TiC nanoparticles were measured by a spectrophotometer and the results were illustrated in Fig. 3-8. The reflectivities of the AlSi12-TiC powder with x=0.05 and 0.25 are 38.35 ± 2.81% and 15.17 ± 1.88%, respectively, at a wavelength of 1070 nm. It should be noted that the reflectivity of AlSi12-TiC (x=0.05) sample is slightly lower than that of pure aluminum powders (43.43 ± 3.39%). The SEM study, as shown in Fig. 3-6d, show that the surface of AlSi12-TiC powder with x=0.05 is not fully covered by nanoparticles, which could explain the minor reduction of reflectivity. As the x increases to 0.25, the surface of the AlSi12-TiC powders are fully coated with TiC the nanoparticles, resulting in a significant reduction of the laser reflectivity at a wavelength of 1070 nm. A reflectivity of 15.17 ± 1.88% were measured from the AlSi12-TiC (x=0.25) powder, showing a comparable reflectivity (14.58 ± 0.46%) to AMNC (x=0.25) powder.

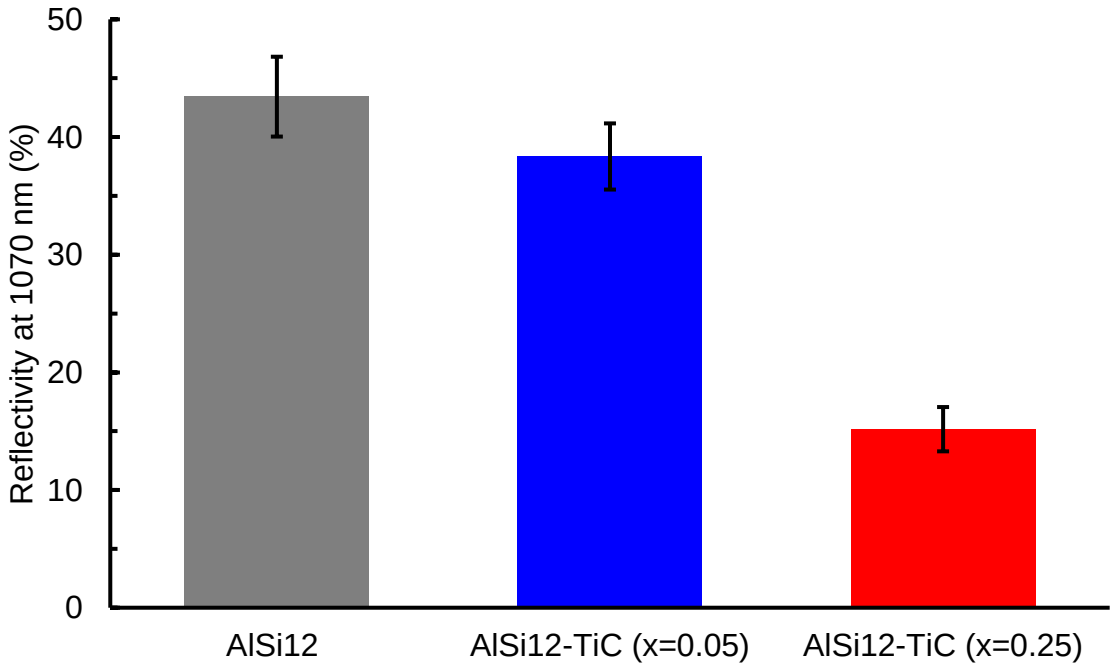

Figure 3-8: Reflectivity of AlSi12 powders with and without nanoparticles

3.2.3 AMNCs powders produced via mechanical mixing

3.2.3.1 Morphology, internal microstructure and size distribution

To demonstrate the scalability of AMNC powders using the mechanical mixing method, we designed two different volume fractions between the aluminum powder mixtures to the salt, i.e., 10 vol. % and 20 vol. %, respectively. The volume ratio, x, between the nanoparticles and the aluminum powder was maintained constant at 0.25 (See detailed information in the section of 3.1.2). The resulting AMNC powders produced with ten volume fraction of aluminum powders in the salt mixture, as illustrated in Fig. 3-9a, reveal the powder size distribution is approximately 36.5±5.9 μm. The SEM images (Fig. 3-9b and Fig. 3-9c) show that the spherical AMMNC powders are fully coated with TiC nanoparticles (gray spots) using the novel self-assembly fabrication method. Additionally, the image of internal microstructure (Fig. 3-9d) indicates the TiC nanoparticles (gray spots) were uniformly distributed inside the Al matrix powder, demonstrating the mechanical mixing AMMNC powders have similar results of the ultrasonic processing AMNC powders.

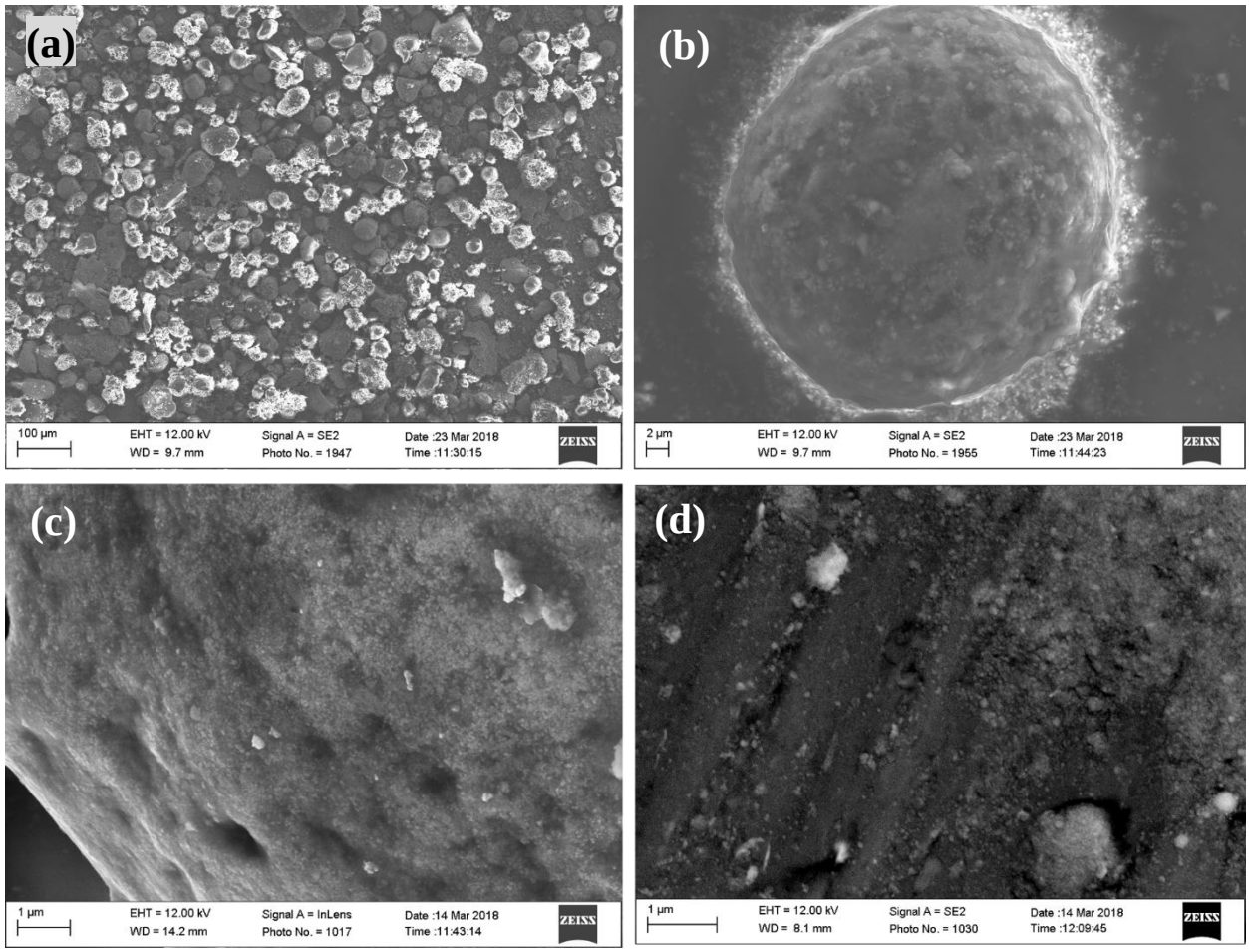

Figure 3-9: Morphology and microstructure of AMNC powders produced by mechanical mixing method. **The volume fraction between aluminum and salt is designed at 10 vol.%. a, b,** SEM images of AMNCS powder with x=0.25. **c,** surface and **d,** internal microstructure of a mechanical mixing AMNC powder with x=0.25.

In addition to the 10 vol. % of the matrix powders in the salt, AMNC powders designed with 20 vol.% of aluminum powders in the salt mixture were also fabricated by mechanical mixing method. Ideally, the mass of the resulting spherical AMNC powders (with uniform size distrubtion) could reach a greater amount than that of 10vol.% of matrix powder in the salt. However, the SEM images of the AMNC powders (Fig. 3-10a and Fig. 3-10b) reveal that the size distrubtion of the

powder is less uniform. The large powder with a size about 500 μm has been observed, as shown in the cross sectional image of Fig. 3-10d. It is believed that with the less amount of salt, the powder size mopholorgy would be more difficult to control. Fortunately, while the size distribution is less uniform, the TiC nanoparticles (gray color) were still self-assemled at the surface of the Al (Fig. 3-10b) and effectively pushed into the matrix (Fig. 3-10d and Fig. 3-10e), driven by minimaztion of the free energy in the immiscible liquid system. These results from mechanical mixing AMNC powders demostrate the feasibility of MMNC powder fabrication and provide a low cost route for the scalable production.

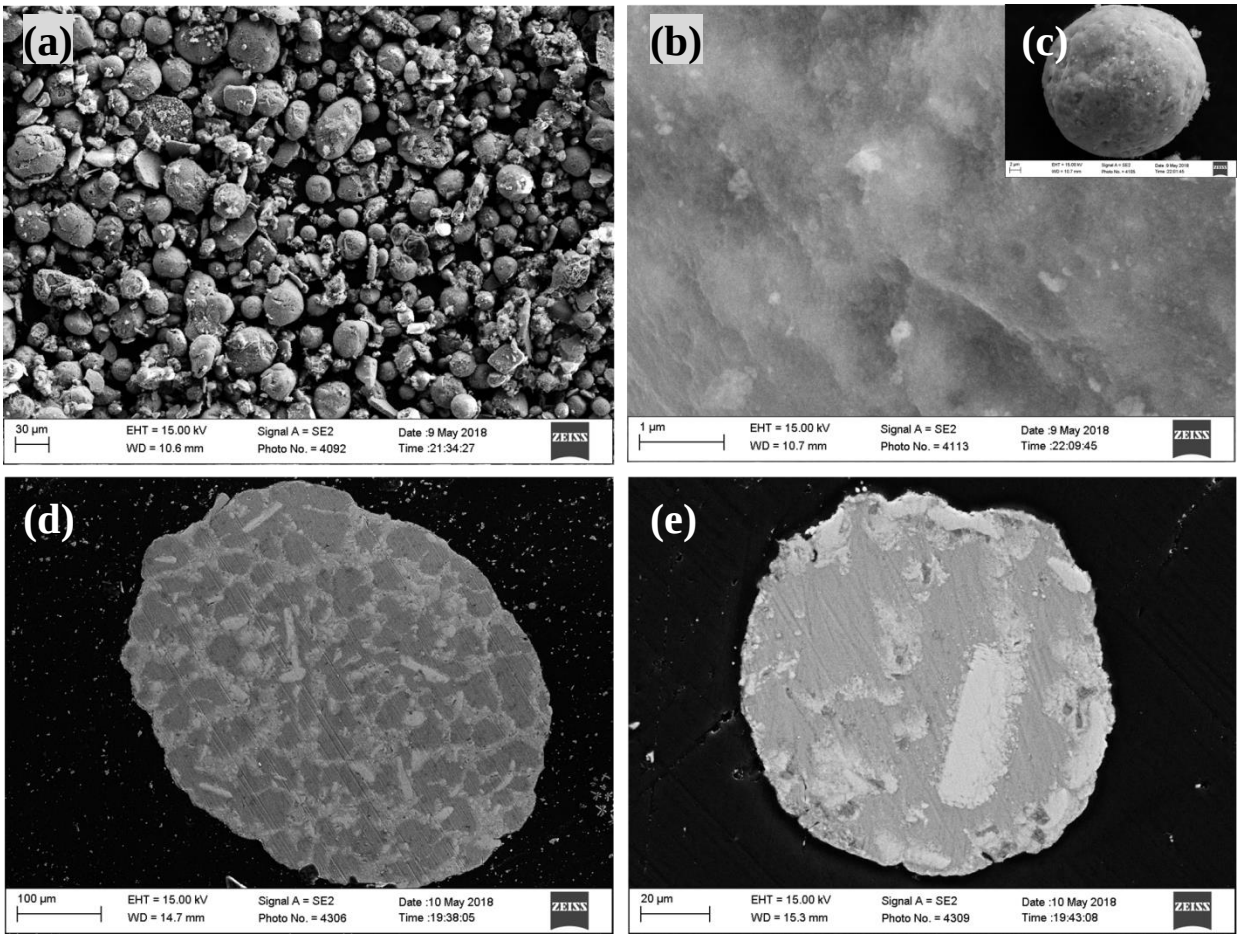

Figure 3-10: Morphology and microstructure of AMNC powders produced by mechanical mixing method. The volume fraction between aluminum and salt is designed at 20 vol.%.

3.2.3.2 Laser Reflectivity

It is expected that two types of AMNC powders have comparable laser reflectivity, because both obtain nanoparticles-coated surface morphology and uniform nanoparticle distribution inside the AMNC powders. The results from reflectivity measurement (Fig. 3-11) show that mechanical mixing AMNC(x=0.25) powders with a different volume fraction of Al powder in the salt (vol. 10% and vol. 20%) are 13.63 ± 2.16% and 14.02 ± 1.5%, respectively, at the laser wavelength of 1070 nm, which the results are comparable to that of AMNC powders produced by ultrasonic processing (14.58 ± 0.46%).

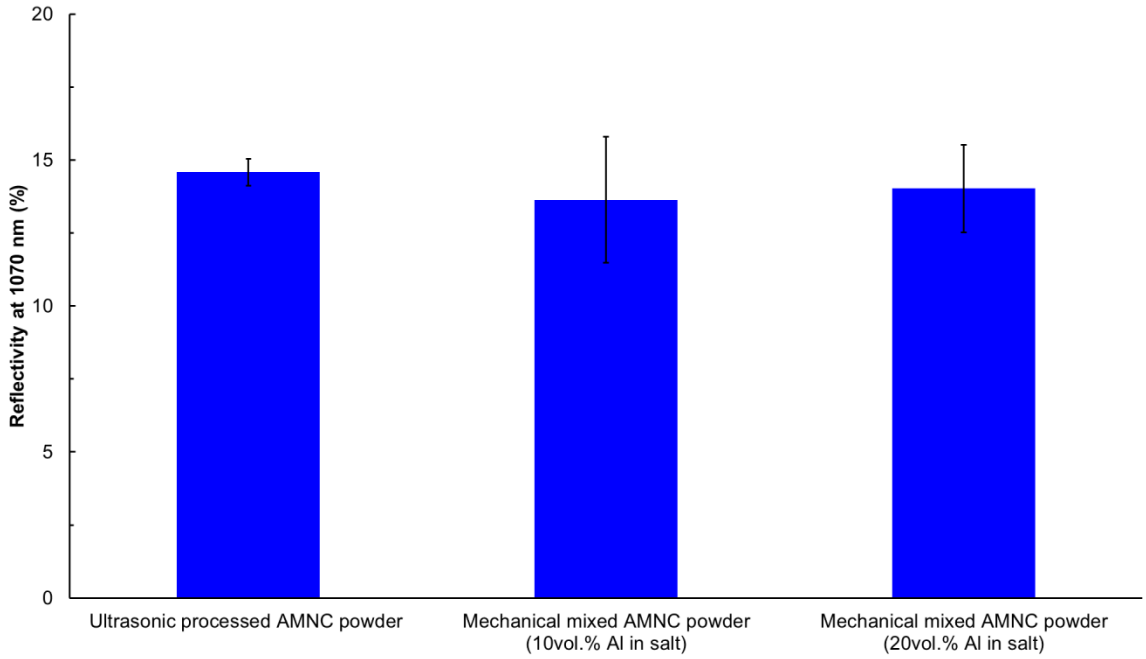

Figure 3-11: Comparison of the reflectivity at the wavelength of 1070 nm for two types of AMNC powders

3.2.4 Copper-matrix powder via mechanical mixing

3.2.4.1 Morphology, internal microstructure and size distribution

3.2.4.1.1 Copper matrix nanocomposite powders produced via wet mechanical mixing

Figure 3-12 shows the morphology of Cu-WC nanocomposite powders with x=0.1. As shown in Fig.3-12a, the powder size distribution is relatively less uniform compared to that of Cu-WC (x=0.25). To explain the non-uniform size distribution, It is believed that the less amount of nanoparticles in the melt (x=0.10) results in a longer time for Cu droplets to be fully decorated by WC nanoparticles. During the high speed stirring, small Cu droplets (with a partially coverage of nanoparticles) merged together before they were fully decorated by WC nanoparticles, forming Cu-WC nanocomposite powders with various sizes, as shown in Fig.3-12a. The brass sieves with different mesh sizes were applied used to obtain the powders with a size less than 44 μm (See section 3.1.3). A SEM image (Fig. 3-12b) shows a Cu matrix nanocomposite powder is assembled by WC nanoparticles. To reveal the internal microstructure, the cross sectional SEM images of the powder were obtained from the polished powder sample (See Cu powder system at section 3.1.2.2). Microstructure analysis reveals a different nanoparticle distribution inside the Cu matrix powders (Fig. 3-12c and Fig. 3-12d). Since the powder size distribution is non-uniform, it is expected that the nanoparticles distribution in every powders is also non-uniform. More detailed process optimization, such as mixing speed, processing temperature, and salt amount, are necessary to obtain the desired powder results.

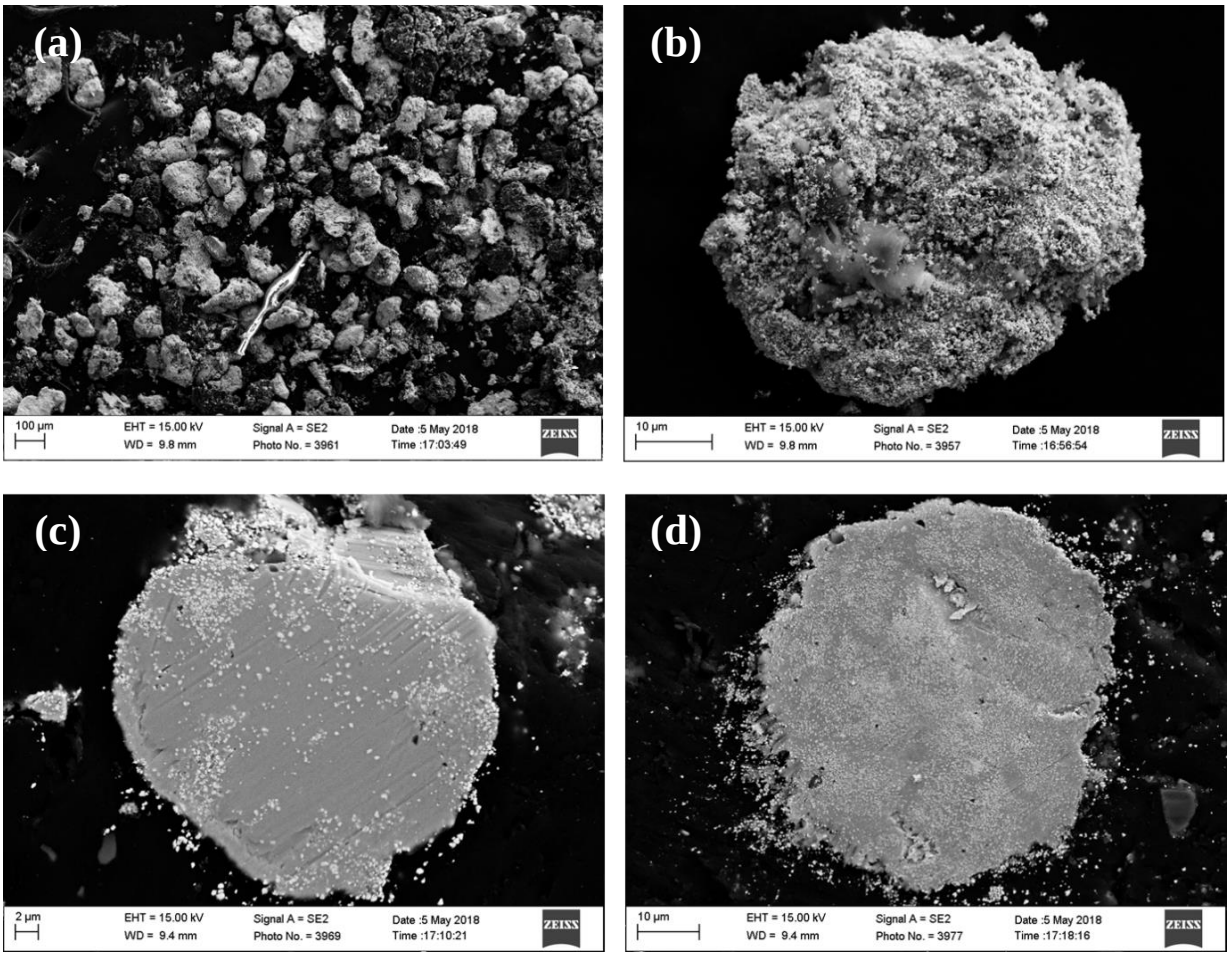

Figure 3-12: Morphology and microstructure of Cu-WC (x=0.1) nanocomposite powders. a, b SEM images of **Cu-WC** (x=0.1) powders**. b, c,** Internal microstructure **Cu-WC** (x=0.1) nanocomposite powders.

The previous results suggest that the powder size is less uniform with a small amount of nanoparticles in the melt. To obtain a uniform size distribution, a higher volume ratio between nanoparticles and Cu matrix powders, i.e., x=0.25, was designed. After fabrication, the powder size distribution was significantly improved and only a few powders with size about 500 µm were observed. The resulting powders were again separated by sieves to obtain the powders with the desired size (See Cu powder system at section 3.1.2.2), as shown in Fig.3-13a and Fig.3-13b. Clearly, powders with more uniform and spherical shapes were produced under a higher amount

of volume ratio, x, indicating the self-assemble hypothesis is correct. Similar to the case of Cu-WC (x=0.05), the nanoparticles were self-assembled at the surface of the Cu powder (Fig. 3-13d) and also distributed inside the matrix (Fig. 3-13b). More engineering optimizations are still needed to improve the nanoparticle distributions inside the matrix and the powder size distribution.

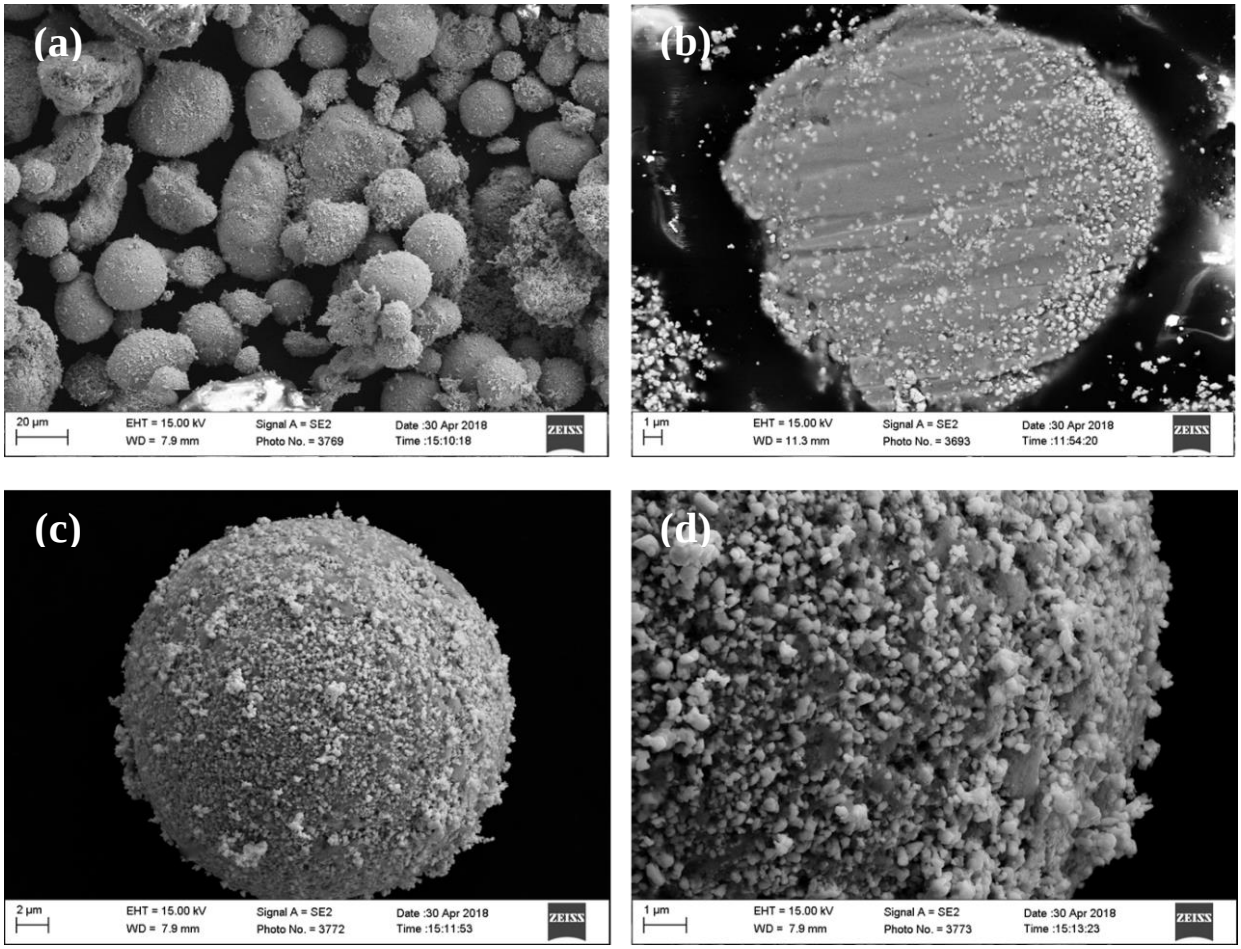

Figure 3-13: Morphology and microstructure of Cu-WC (x=0.25) nanocomposite powders. a, b SEM images of Cu-WC (x=0.25) powders. **b, c,** Internal microstructure of Cu-WC (x=0.25) nanocomposite powders.

3.2.4.1.2 Copper matrix nanocomposite powders produced via dry mechanical mixing

To obtain a uniform powder size distribution, a relative high volume ratio, i.e., x=0.66, was designed. A "dry" mechanical mixing method was proposed to eliminate any external mechanical shearing during the fabrication (See detailed difference at section of 3.1.2.2). The morphology of a spherical Cu-WC nanocomposite powder with x=0.66 is shown in Fig.3-14, indicating that the WC nanoparticles were self-assembled on the surface of a Cu micro particle (Fig. 3-14a, and Fig. 3-14b) because of the favorable energy state. Moreover, the resulting Cu-WC nanocomposite powders show a relatively uniform size distribution, even the nanoparticles distribution inside the Cu matrix (Fig. 3-14d). The average size of Cu-WC (x=0.66) is 41.9 ± 6.2μm. Since there was no external mechanical stirring, the nanoparticles in the dry mechanical mixing process self-assembled at the surface and distributed inside the matrix were mainly relied on the interfacial energy among salt, copper and nanoparticles. Therefore, the powders produced by drying mixing method have a relatively less nanoparticles coverage at the surface.

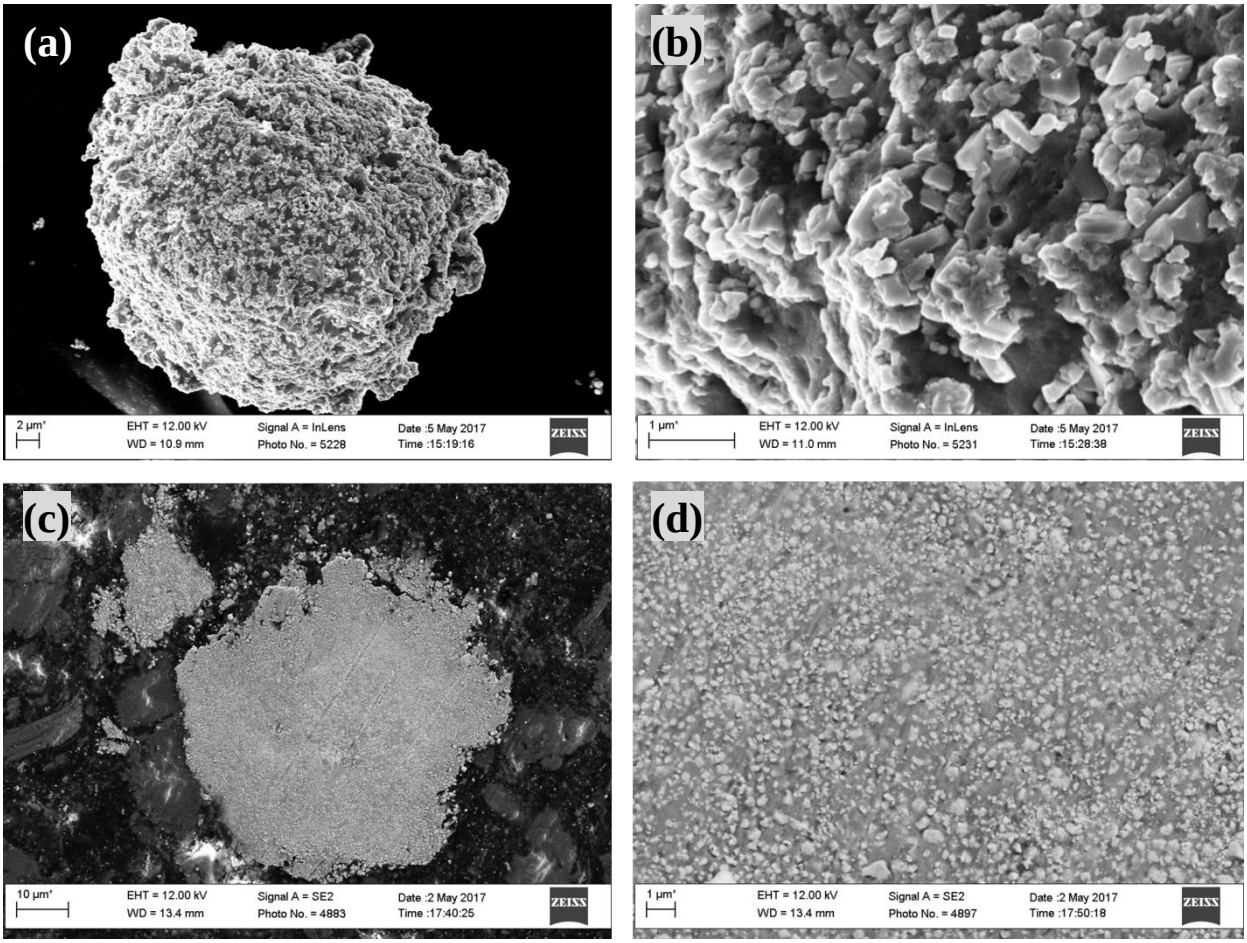

Figure 3-14: Morphology of Cu-WC (x=0.66) nanocomposite powders

3.2.4.2 Laser Reflectivity

The reflectivity of copper powders without and with WC nanoparticles was measured by a spectrophotometer and the results were summarized in Fig. 3-15. The reflectivity of the "wet" mechanical mixing powders (x=0.1 and x=0.25) are 13.83 ± 2.7% and 11.14 ± 2.6%, respectively. Other the other hand, the reflectivity of "dry" mechanical mixing powder (x=0.66) is approximately 33.97 ± 5.9%. The dry mechanical mixing nanocomposite powder has a higher laser reflectivity mainly due to the fact that a less nanoparticle coverage on the surface of Cu powders.

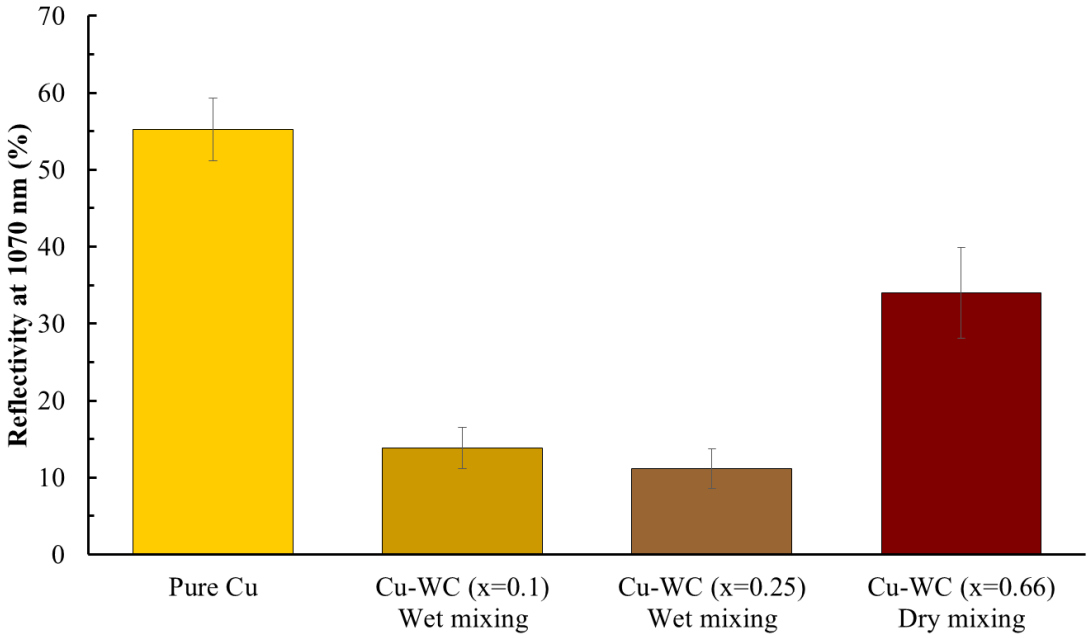

Figure 3-15: Comparison of the reflectivity at the wavelength of 1070 nm for copper powders with and without nanoparticles.

3.3 Summary

This chapter provides two processing routes, i.e., nanoparticle self-assembly with assistance of mechanical mixing or ultrasonic processing, for the fabrication of metal matrix nanocomposite (MMNC) powders. Two novel types of aluminum matrix nanocomposite powders (AMNC and AlSi12) that contain a high density of embedded TiC nanoparticles were successfully produced using self-assembly method with assistance of ultrasonic processing. The resulting MMNC powders show a significant reduction in laser reflectivity as the nanoparticle volume fraction increases. In addition, a scalable powder fabrication method, i.e., self-assembly with assistance of mechanical mixing, was proposed. The AMNC powders by mechanical mixing were successfully fabricated with similar size, morphology, and laser reflectivity to those by ultrasonic processing, providing a low cost and scalable route for MMNC powder fabrication. Cu matrix nanocomposite powers with different WC nanoparticle incorporation were also produced using

this method. More efforts are necessary to improve the resulting coper powder size distribution and its internal nanoparticle distribution.

CHAPTER 4 LASER ADDITVIE MANUFACTURING OF ALUMINUM MATRIX NANOCOMPOSITE

4.1 Experimental method

4.1.1 Laser additive manufacturing of pure aluminum and AMNCs

The schematic of a customized laser additive manufacturing system is illustrated in Figure 4-1. The experiment was conducted by a 1070 nm fiber laser (SP-200C-W-S6-A-B, SPI Lasers) tuned to a power output of 200 W, a scan speed of 0.2 m/s at continuous wave mode, a spot size of 50 μm, a hatching space of 30 μm, and a 90° scanning direction difference for each layer, as well as a customized stainless vacuum chamber (with a vacuum level at about 1×10^{-2} *torrs*). A temperature control system was installed for preheating of the powders. For each cycle of laser deposition, a AMNC powder layer (x=0.25 and x=1) with a thickness of about 50 μm was manually deposited on a pre-machined Al 1100 alloy substrate (≥99.0%, McMaster-Carr) with a dimension of 25.4 mm × 25.4 mm × 6.27 mm. The thickness of the powder layer was guided by a customized layer-thickness control device. A z-axis manual stage was placed in the chamber to manually adjust the laser focal point since the height of a new layer of powders will be different after laser melting of each layer. After the samples were mounted onto the temperature control system inside the vacuum chamber, it was firstly evacuated to a vacuum level of about 1×10^{-2} *torr,* followed by a constant argon flow about 30 minutes to reduce the oxygen content in the working environment. The argon purging process, i.e., vacuum pumping followed by argon purging, was repeated twice before of the preheating and laser selective melting. The laser scanning patterns of 3 mm × 3 mm, 3 mm × 18.5 mm, and 8 mm × 18.5 mm were processed the powder layers at temperatures of 25 °C (without preheating) or 300 °C (with preheating). The layer deposition process was repeated to obtain a designed layer thickness for fundamental study. In this study, the AMNC samples with a

thickness of 100 ± 16 µm (AMNC with 17 vol.% TiC) and of 309 ± 16 µm (AMNC with 35 vol.% TiC) were deposited for characterization. Laser processed pure Al samples with a thickness of about 192 ± 30 µm were also obtained for comparison. Moreover, to compare the material performance obtained from melting two categories of AMNCs powders, laser deposited AMNC (15 vol.% TiC) sample with a thickness of 513 ± 36 µm was produced by laser melting of mechanical mixing AMNCs powders.

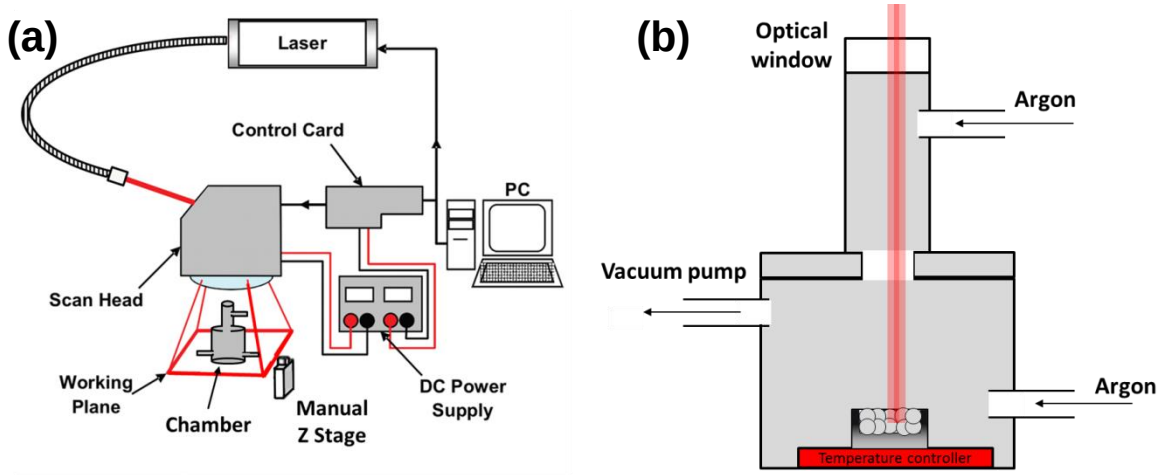

Figure 4-1: Schematic of lab-built laser additive manufacturing system. a, A 1070 nm fiber laser (SP-200C-W-S6-A-B, SPI Lasers) with a power of 200 W for laser deposition. A manual z-axis stage was used to accommodate the laser focal point. **b,** The vacuum chamber with a temperature control system for powder layers.

4.1.2 Characterization

4.1.2.1 Micro/nanostructure

Laser layer-deposited aluminum samples without and with nanoparticles (AMNCs) were characterized using scanning electron microscopy (SEM), Energy dispersive X-ray spectroscopy (EDS/EDX), focused ion beam (FIB), Electron backscatter diffraction (EBSD) and transmission electron microscopy (TEM). SEM and TEM were used to reveal the dispersion and distribution of

the TiC nanoparticles in the laser processed AMNC samples. The samples were first vertically mounted in epoxy holders with an outside diameter of 30 mm, and then filled with a mixture of a transparent curable epoxy and a hardener (Allied High Tech Products, Inc.) with a ratio of 10 to 3, followed by grinding and polishing. To clearly expose the TiC nanoparticles on the surface of the Al matrix, polished samples were 52° tilted and slightly etched by FIB with gallium ions, followed by obtaining SEM images with EDS analysis. High resolution TEM images were obtained by Scanning/Transmission Electron Microscopy (S/TEM, Titan, FEI). The TEM samples prepared by FIB were obtained from the micropillars after compression tests. Fourier-filtered high resolution TEM images were obtained to reveal the interface between the TiC nanoparticles and the Al matrix.

4.1.2.2 Mechanical characterization

The mechanical performances of laser deposited samples were characterized using microcompression tests (*in-situ and ex-situ*), nanoindentation, and Vickers hardness test.

Microcompression test: A MTS XP Nanoindenter was used to conduct microcompression tests to study the mechanical properties of the laser-processed samples with and without TiC nanoparticles. FIB-machined micropillars with a size of 4.0 ± 0.1 μm in diameter and a height of 10 ± 0.5 μm were compressed by a flat punch probe with a size of 10 μm at room temperature using the displacement control mode, and a strain rate of 2×10^{-3} s^{-1}. *In-situ* microcompression tests were conducted using a PI 95 PicoIndenter (Hysitron Inc.) with a flat punch diamond probe of 20 μm inside a FEI Quanta 3D SEM/FIB. FIB-machined micropillars (4 μm in diameter and 9 μm in height) from a AMNC (35 vol.% TiC, preheated at 300°C) sample were compressed using the load-control mode, and a strain rate of 2×10^{-3} s^{-1}. The real time load-displacement data and

in-situ deformation videos of micropillars were monitored, captured and recorded by TriboScan (Hysitron Inc.).

In-situ microcompression test at elevated temperatures: In-situ microcompression tests were conducted using a PI 95 PicoIndenter (Hysitron Inc.) with a flat punch diamond probe of 20 μm inside a FEI Quanta 3D SEM/FIB. FIB-machined micropillars (4 μm in diameter and 9 μm in height) from a AMNC (35 vol.% TiC, preheated at 300°C) sample were compressed using the load-control mode, and a strain rate of 2×10^{-3} s^{-1}. The real time load-displacement data and in-situ deformation videos of micropillars were monitored, captured and recorded by TriboScan (Hysitron Inc.). In-situ microcompression was conducted at temperatures of 200 ºC, 300 ºC, and 400 ºC by a resistive micro-electro-mechanical systems (MEMS) heater. A AMNC (35 vol.% TiC, preheated at 300 °C) sample was attached to the MEMS temperature-control sample heater using high temperature silver conductive epoxy (Ted Pella product #16014), followed by installing the sample heater on the PicoIndenter system. The resistance of the heating element was utilized to elevate the sample temperature to a desired value. Each temperature level was maintained 300 seconds before the compression tests. A resistive temperature detector (RTD) sensor was used to measure the real time temperature and provide feedback for the MEMS temperature controller.

Microcompression test of samples after exposure at elevated temperatures: To further determine the thermal stability, AMNC (35 vol.% TiC) samples, after a heating period of 1.0 hour at 400 °C were cooled down to room temperature and further microcompression tests were conducted again under room temperature. Micropillars with a diameter of 4 μm and a height of 9 μm were prepared by FIB. All testing parameters and experimental setups remained the same as in the section of *Microcompression test.*

Measurement of elastic modulus: Nanoindentation tests were performed by MTS Nanoindenter XP to evaluate the elastic modulus of the laser processed materials. The samples with nanoparticles (15 vol.% TiC, 17 vol.% TiC and 35 vol.% TiC) and without nanoparticles (pure aluminum) were compressed by a Berkovich tip with an indentation depth of 2 μm. For each sample, 20 randomly selected points were measured. Elastic moduli were calculated from the unloading curves.

Measurement of hardness: Vickers hardness with a load of 50g and the dwell time of 10s was used to characterize the microhardness of the deposits, i.e., pure Al, and AMNC (15 vol.% TiC, 17 vol.% TiC and 35 vol.% TiC). Five tests were conducted at different locations for each sample for the average value of microhardness.

4.2 Experimental results (AMNC powder via Ultriasonic processing)

4.2.1 Micro/nanostructure

A laser deposited AMNC sample (35 vol.% TiC) with a thickness of 309 ± 16 μm, as shown in Fig.4-2, was layer by layer deposited by laser melting of the Al powder (x=1) bed, which was preheated to 300 °C. A SEM image was captured from the top of the deposited sample (8 mm × 18.5 mm), showing the AMNC has a good uniformity and is well bonded to the previous layers.

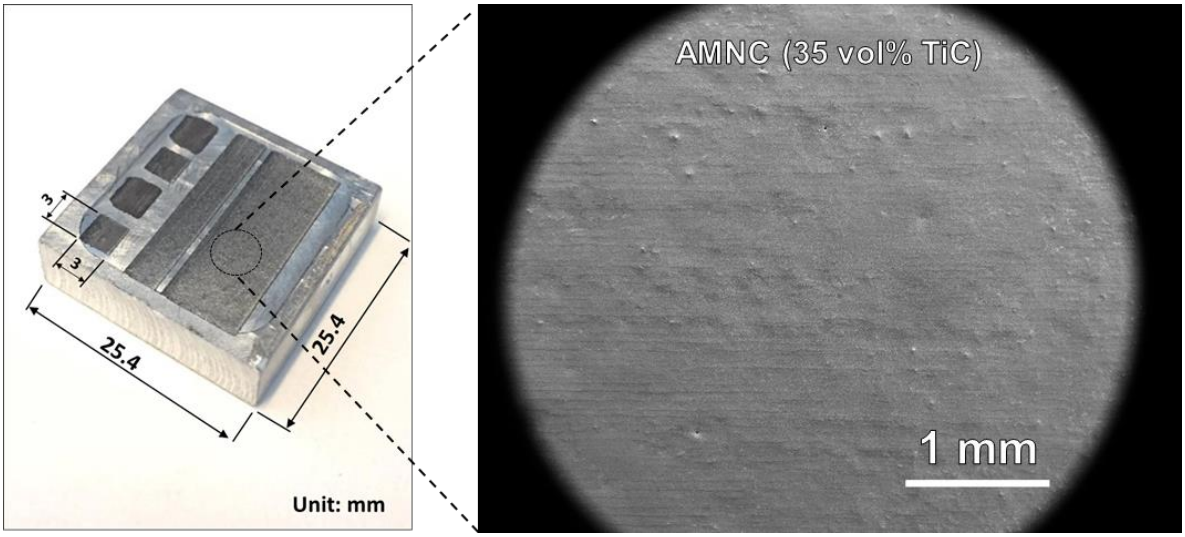

Figure 4-2: Surface of laser deposited aluminum matrix nanocomposites (AMNC). Top view of laser-deposited AMNC (35 vol.% TiC) samples with dimensions of 3 mm × 3 mm, 3 mm × 18.5 mm and 8 mm × 18.5mm. The insert SEM image shows an area of the laser deposited sample

To reveal the interior microstructure, the polished AMNC sample was tilted 52° to acquire cross-sectional images (See Microstructure characterization in Methods), as shown in Fig. 4-3a and Fig. 4-3b, indicating that a high volume fraction of TiC nanoparticles were dispersed and distributed homogeneously throughout the Al matrix. The uniform dispersion and distribution of TiC nanoparticles in Al matrix can be attributed to the unique nature of laser processing and the good wetting of TiC in molten Al. The laser induced rapid cooling rate can reach up to $10^{6\text{-}7}$ K/s [162], and therefore the movement of atoms and particles freezes within milliseconds. The initial AMNC powders were fully melted and then solidified rapidly. During the non-equilibrium laser-induced rapid melting and solidification, both the TiC nanoparticles at the surface and inside of AMNC powders did not agglomerate to form clusters.

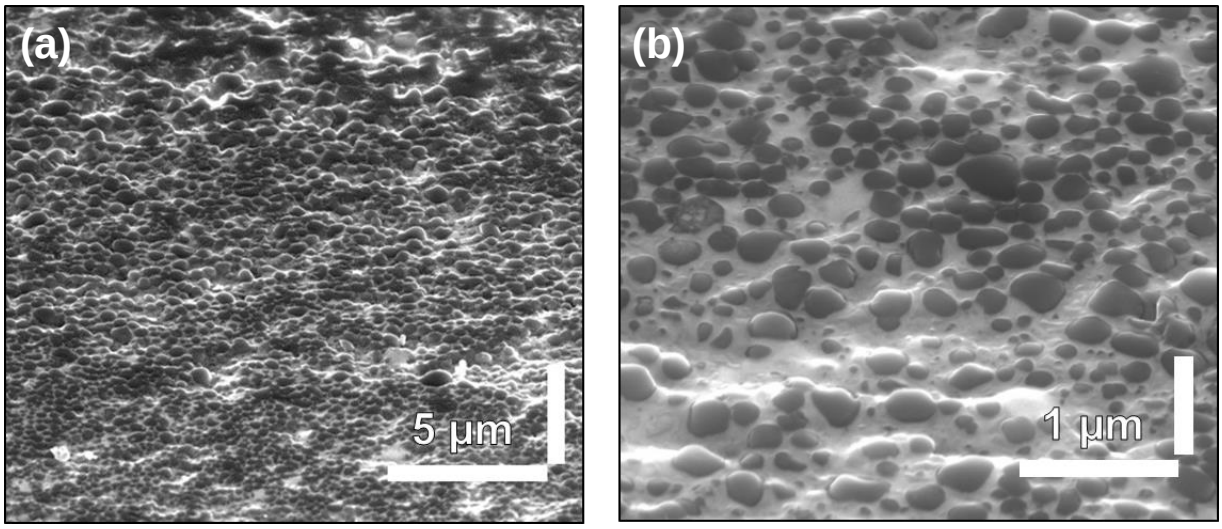

Figure 4-3: Micro of laser deposited aluminum matrix nanocomposites (AMNC). a, b, 52° tilted cross-sectional SEM images of laser processed AMNC (35 vol.% TiC) were captured under different magnifications, showing that TiC nanoparticles are uniformly dispersed and distributed in aluminum.

Despite the formation of some larger particles with an average size of 159 nm (as shown by TEM and the histogram in Fig. 4-4a and Fig. 4-4b) after solidification, TiC nanoparticles were still uniformly dispersed and distributed in AMNC samples. The TiC nanoparticles on the surface can absorb the laser beam more effectively to achieve a much higher temperature than the melting point of aluminum, enabling a rapid dispersion and diffusion of surface TiC nanoparticles into the core of the molten aluminum powders to expose liquid aluminum for bonding into dense layers with unprecedented properties. The rapid heating and cooling during the LAM process also limited the chemical reaction of TiC below 780 ˚C in aluminum melt.

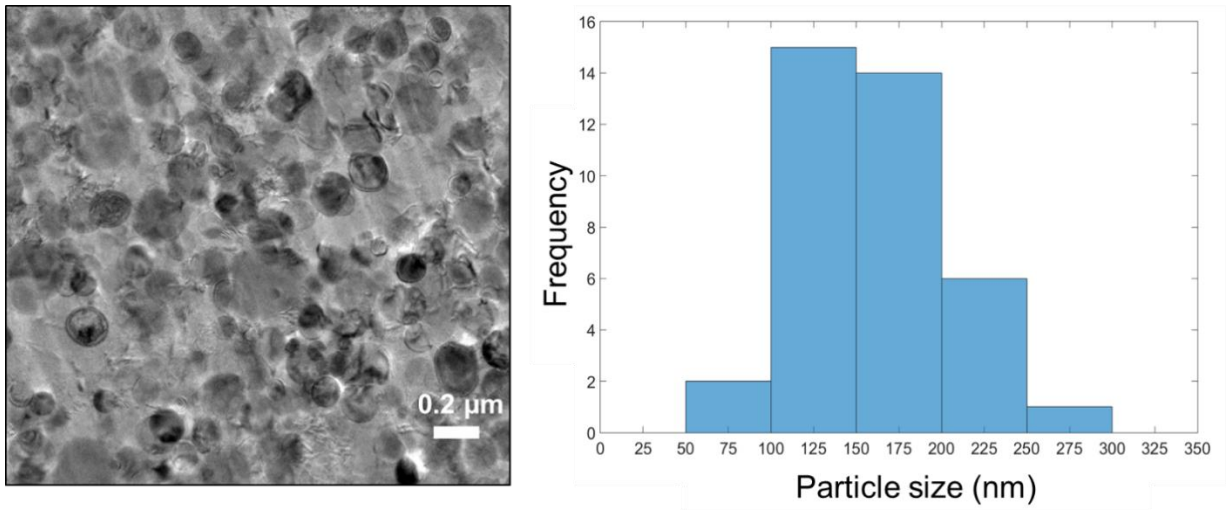

Figure 4-4: Nanostructure characterization of laser deposited aluminum matrix nanocomposites (AMNC). a, A bright-field TEM image indicates that TiC nanoparticles are well dispersed in Al matrix. **b,** A histogram of TiC nanoparticle size distribution analyzed from image a.

To study the interface between Aluminum matrix and the TiC nanoparticles, the AMNC (35 vol.% TiC) samples were characterized at the atomic scale by high-resolution TEM, as shown in Fig.4-4a. A magnified image, as shown in Fig. 4-5b, was captured for further Fast Fourier Transform (FFT) processing. As shown in Fig. 4-5b, TiC nanoparticles bond with Al matrix extremely well as confirmed in the FFT filtered high resolution TEM image.

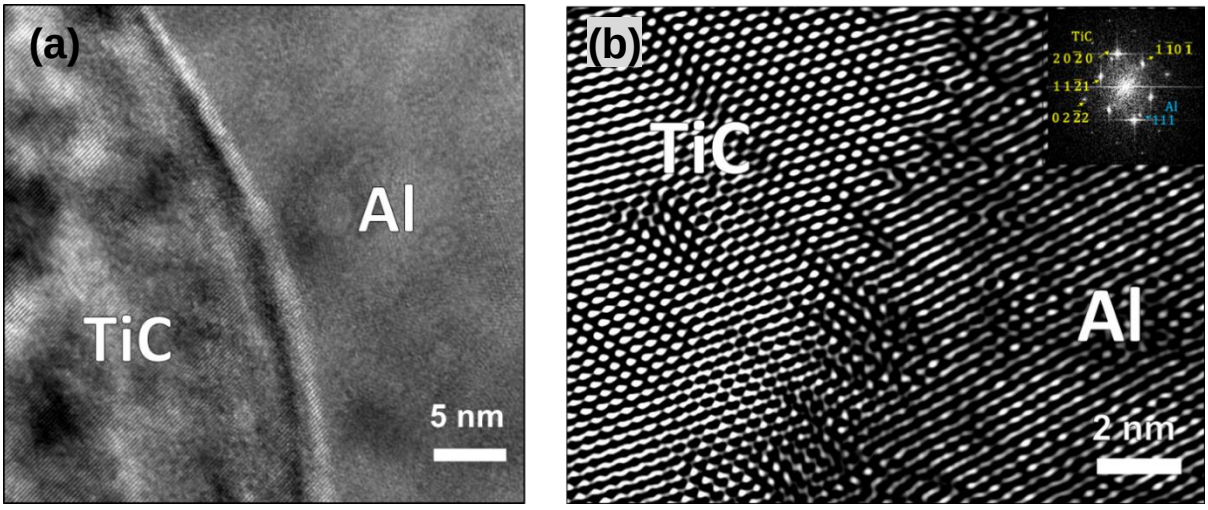

Figure 4-5: Nanostructure characterization of laser deposited aluminum matrix nanocomposites (AMNC). a, A magnified bright-field TEM image from Fig.4-5a. **b,** A FFT filtered high resolution TEM image from Fig. 4-5a shows good bonding between TiC nanoparticle and aluminum. Inserts are the fast Fourier transforms corresponding to the planes of (1 1 1) aluminum matrix and of (2 0 0) TiC nanoparticles.

It is argued that the high density of uniformly distributed TiC nanoparticles play a critical role of refining the Al grains because the nanoparticles can act as nucleation sites and also restrict the growth of the Al grains during solidification. The EBSD mapping results revealed the grain size and crystallographic texture difference from the laser-deposited samples of pure Al and AMNC (35 vol.% TiC), as shown in Fig. 4-6b. Clearly, TiC particles, i.e., the black spots shown in Fig.4-6b, were uniformly distributed on the Al matrix grain, indicating that TiC nanoparticles were well dispersed and distributed throughout the Al matrix. For the high (i.e., 35 vol.%) volume fraction of reinforcing TiC nanoparticles and the good dispersion of these nanoparticles, it is necessary to remove the TiC phase from Fig. 4-6b to better reveal the grain size of the refined Al matrix. Whereas the average grain size for the pure aluminum is approximately 2.7 ± 1.4 μm, the average grain size for the AMNC (35 vol.% TiC) was refined to 331 ± 95 nm, as shown in the

histogram in Fig. 4-6d and Fig. 4-6e. Recent studies also observed that the grain size of the laser additive Al sample can be reduced after the incorporation of ceramic nanoparticles[34,89].

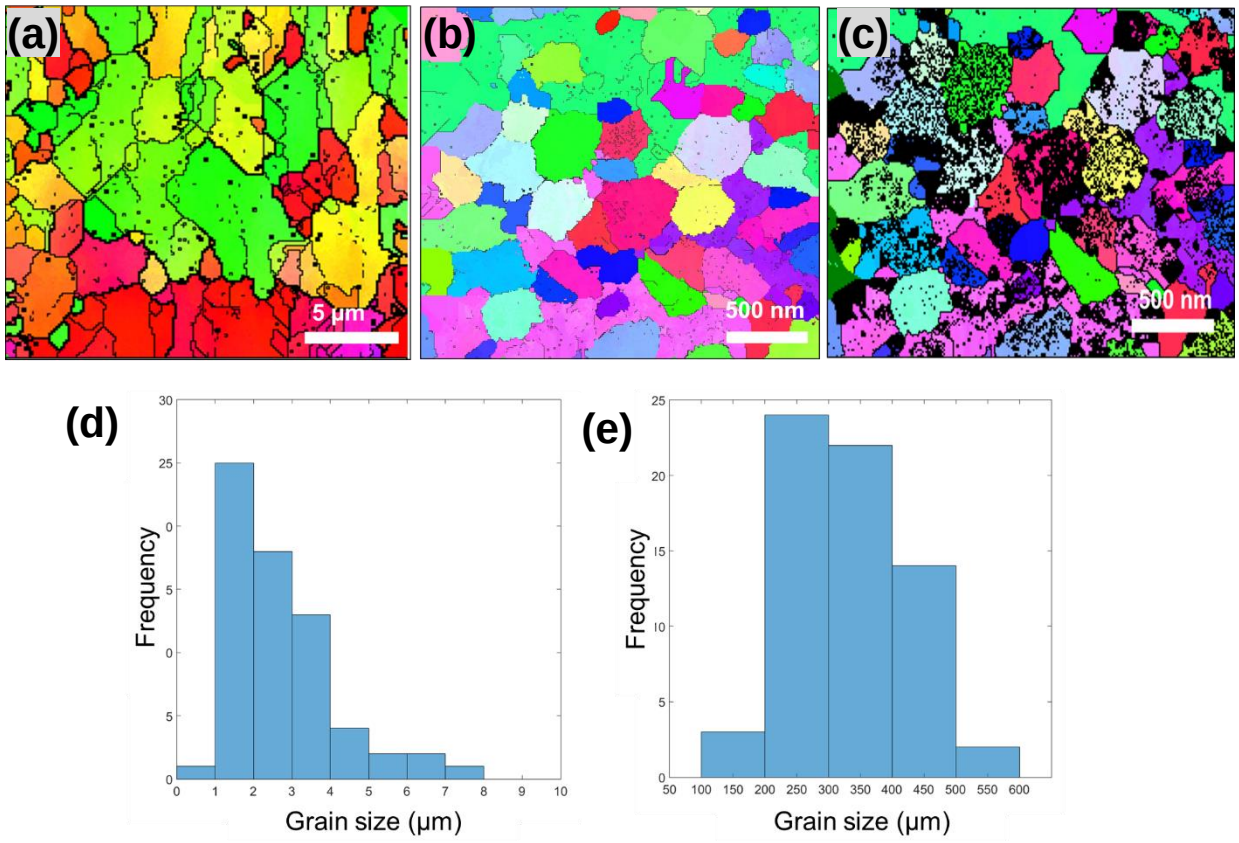

Figure 4-6: a, Grain maps of laser-deposited a, pure aluminum and b, AMNC (35 vol.% TiC) without TiC signal. **c,** AMNC (35 vol.% TiC) with TiC signal. The distribution in grain size for the **d**, pure aluminum and **e**, AMNC (35 vol.% TiC, preheated at 300 °C).

4.2.2 Material performance

4.2.2.1 Mechanical behavior at room temperature

To evaluate the enhancement of mechanical properties due to such high density of TiC nanoparticles, microcompression tests were first conducted at room temperature. Micropillars with a diameter of 4.0 ± 0.1 μm and a height of 10.0 ± 0.5 μm were carefully machined by FIB from

the laser-deposited samples with and without nanoparticle reinforcements, as shown in Fig.4-7. It should be noted that the locations of the micropillars were chosen randomly.

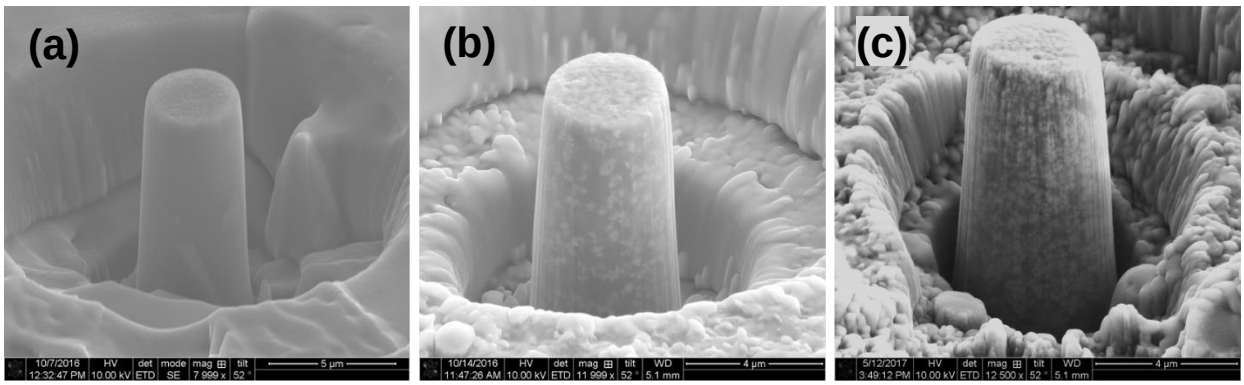

Figure 4-7: Micropillars of laser processed aluminum samples without and with nanoparticles. a, pure aluminum. **b,** AMNCs (17 vol.% TiC) **and c**, AMNCs (35 vol.% TiC).

After microcompression test, a yield-strength curve was obtained as shown in Fig. 4-8a, the pure aluminum sample has a yield strength of only about 92 ± 16 MPa (Fig. 4-8a, the curve in black), while the AMNC samples (with 17 vol.% TiC, processed at 25°C, i.e., no preheating) offer a yield strength of up to 300 ± 52 MPa (Fig. 4-8a, the curve in blue). With a higher TiC loading (35 vol.%), the yield strength of the as-deposited AMNC reaches 868 ± 104MPa with a plasticity greater than 10%, as shown in the curve in purple in Fig. 4-8a. Data for each curve was obtained by at least three sets of experiments. To improve the layer uniformity during laser melting, pre-heating of the powder layers at 300 °C was applied. The result shows that yield strength of AMNC (35 vol.% TiC, pre-heated) is about 906 ± 105 MPa (Fig. 4-8a the curve in red) with a plasticity greater than 10%. The characterization of micropillar deformation after the compression was shown in Fig. 4-8b. Multiple slip bands appeared in the laser deposited pure aluminum samples, which are common for microcompression tests of face-centered cubic micropillars[163]. In contrast, the AMNC samples have significantly fewer slip bands as compared to those in the pure Al

samples. It is highly likely that TiC nanoparticles in the Al samples can sustain higher compression loads, resulting in significant higher yield strength**.**

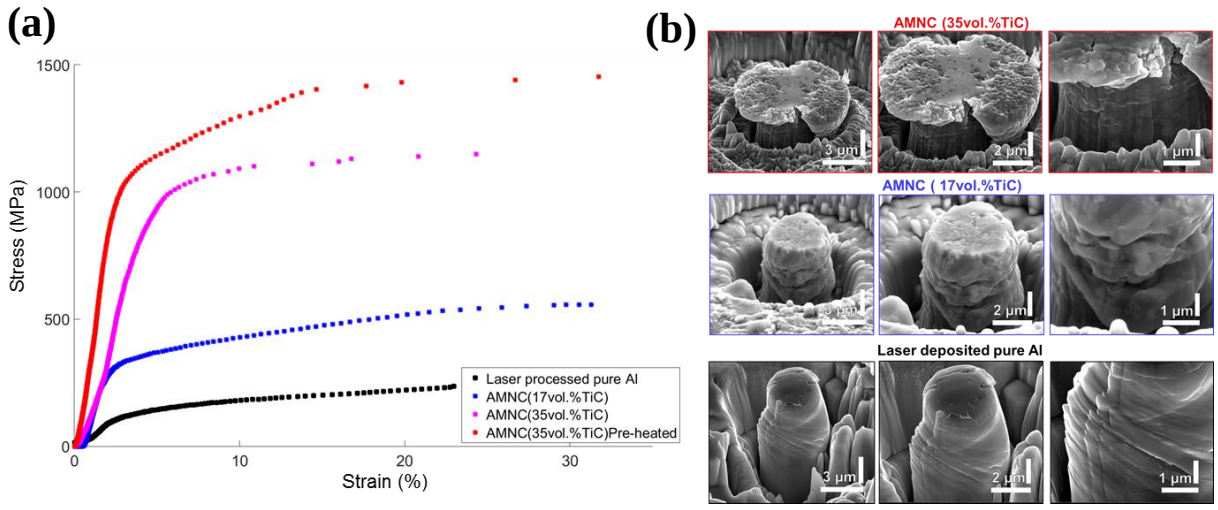

Figure 4-8: Room-temperature mechanical behavior of laser deposited aluminum with and without nanoparticles. a, Typical engineering stress-strain curves of laser deposited Al samples with and without nanoparticles. **b,** SEM images of micropillars after microcompression tests.

4.2.2.2 Young's modulus

It is postulated that the good interfacial bonding between the nanoparticles and Al matrix results in the superior elastic modulus in the AMNC samples. Fig. 4-9 shows that the Young's modulus of the laser-deposited AMNC samples is significantly enhanced compare to that of pure aluminum. While the pure aluminum sample has a Young's modulus of 68 ± 4 GPa, the AMNC (17 vol.% TiC) and AMNC (35 vol.% TiC) samples offer a Young's modulus of 108 ± 10 GPa and 197 ± 27 GPa, respectively.

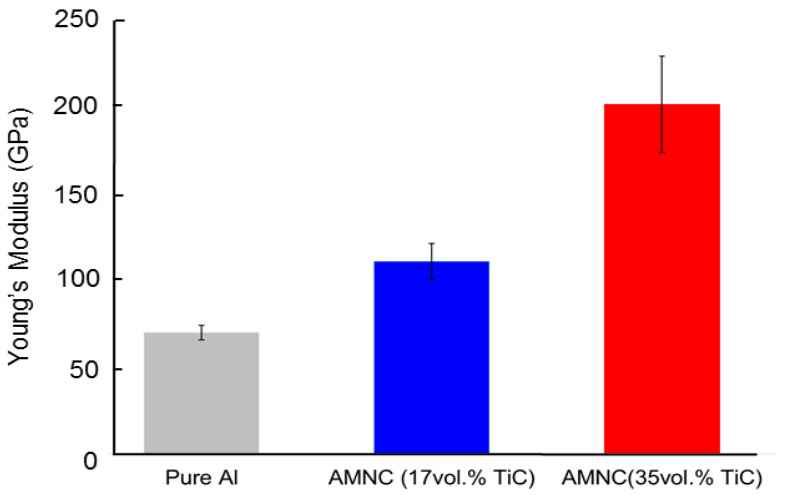

Figure 4-9: Young's modulus of laser-deposited Al and AMNC samples. Error bars represent s.d. for at least twenty data sets.

4.2.2.3 Microhardness

The average Vickers hardness ($HV_{0.05}$) of pure aluminum was 34.1±1.0 HV and that of AMNC nanocomposite, i.e., (17 vol.% TiC) and (35 vol.% TiC), were 100.6±6.7 HV and 330.3±30.6 HV, respectively. It should be noted that the slight variation of the laser deposited samples may due to the thickness of the deposited layer.

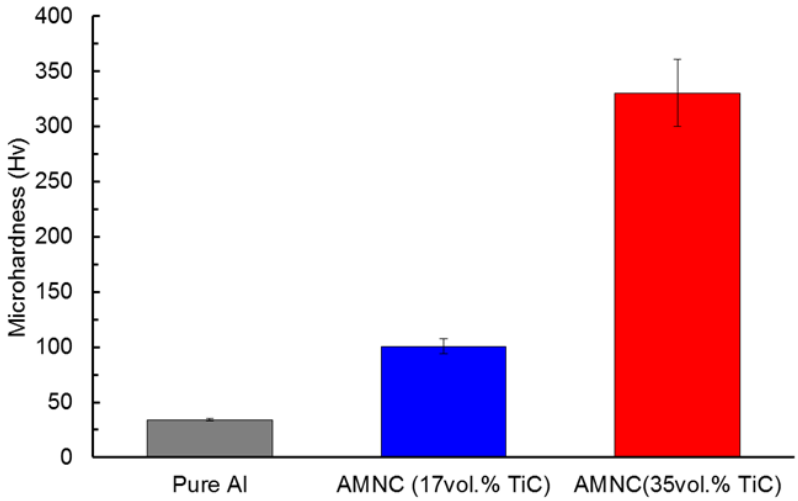

Figure 4-10: Microhardness of laser-deposited Al and AMNC samples.

4.2.2.4 Mechanical behavior at elevated temperature

It is well known that most aluminum alloys lose their strength at elevated temperatures due to the rapid coarsening of grain size and loss of strengthening precipitates[164]28. To evaluate the high temperature stability of the laser-deposited AMNC (35 vol.% TiC) samples, microcompression tests were conducted at 200 °C, 300 °C and 400 °C, as shown in Fig. 4-12. The results from the in-situ microcompression after testing reveal that the AMNC samples can still reach a yield strength of 200 ± 43 MPa with a plasticity greater than 15% at 400 °C, as shown in Fig. 4-10a. The slip bands observed in Fig. 4-10b and 4-10c show the similar results from that of room temperature test (Fig. 4-8b, AMNC 35vol.% TiC), indicating that the TiC nanoparticles in the Al matrix sustain higher compression load, resulting in a significant higher yield strength. Moreover, to further determine the thermal stability after a heating period of 1.0 hour at 400°C, the AMNC samples were cooled down to room temperature and again tested using microcompression testing at 25 °C (See High-temperature stability measurement in 4.1.2.2). The results show that the AMNC (35 vol.% TiC) samples still exhibit a yield strength greater than 800 MPa with a plasticity greater than 10%.

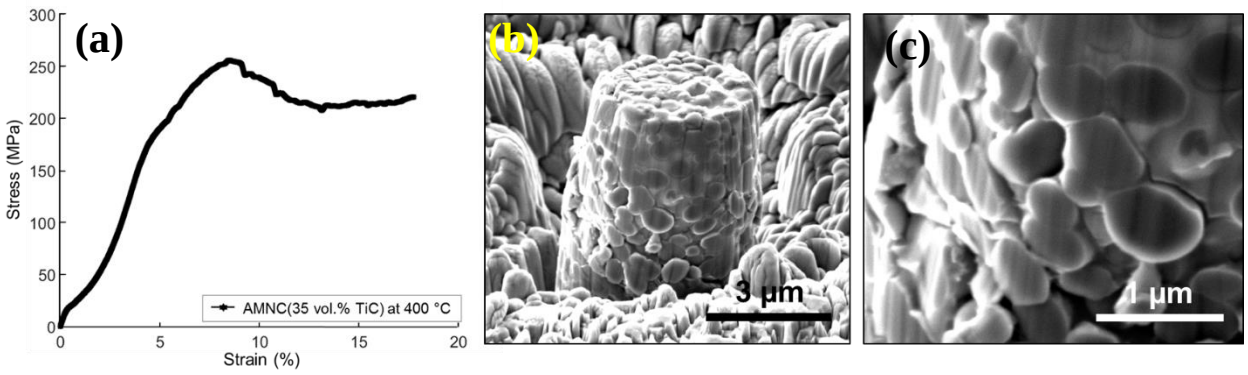

Figure 4-10: Mechanical behavior of laser deposited Super Aluminum at elevated temperature. a, Typical engineering stress-strain curves for microcompression of laser-deposited AMNC (35 vol.% TiC) at 400 °C. **b,** SEM image of micropillar after microcompression tests at 400 °C. **c,** magnified image of **b.**

4.2.3 Strengthening effects

To understand the unprecedented strength obtained in as-deposited AMNCs, the strengthening mechanisms for the AMNC (35 vol.% TiC) can be possibly attributed to Orowan strengthening[154], Hall-Petch effect[158], and load-bearing transfer, which are estimated to be approximately 294 MPa, 104 MPa, and 525 MPa, respectively. These potential strengthening contributions in the laser-deposited AMNC (35 vol.% TiC) samples are discussed as below,

The contribution from Orowan strengthening can be estimated by[154]:

$$\Delta\sigma_{Orowan} = \frac{0.13 G_m b}{\lambda} \ln\frac{r}{b} \tag{1}$$

$$\lambda \approx d_p \left[\left(\frac{1}{2V_p}\right)^{\frac{1}{3}} - 1 \right] \tag{2}$$

,where r is the particle radius, and λ is the inter-particle spacing , d_p is the particle diameter, b is the Burger's vector, V_p is the volume fraction of nanoparticles, and G_m is the matrix shear modulus.

The values for the AMNC samples with 35 vol.% TiC are: b=0.286 nm, G_m=25.5 GPa, V_p=0.35, r=0.5 and d_p=79.5 nm. The particle size is determined by the TEM results in Extended Data Fig.3. The $\Delta\sigma_{Orowan}$ is thus determined to be approximately 294 MPa.

It is well known that the grain size has a significant influence on metal yield strength since grain boundaries act as obstacles for dislocation movement. The TiC nanoparticles can serve as nucleation sites and also the pinning points to inhibit the Al grain growth during solidification. From EBSD mapping results(Fig. 4-6c), the average grain size of the laser-deposited AMNC (35 vol.% TiC) sample is approximately 331 ± 95 nm, as shown in Fig. 4-6a and Fig.4-6d). The yield strength gained from the Hall-Petch strengthening can be calculated by:

$$\Delta\sigma_{H\_P} = kd^{-\frac{1}{2}} \tag{3}$$

where k =0.06 MPa m$^{1/2}$ [165] as the strengthening coefficient for aluminum, d as the average grain size in the AMNC sample. The calculated $\Delta\sigma_{H\_P}$ is 104 MPa.

It is believed that the load-bearing effect significantly contributes to the strengthening of the AMNC sample since the interfacial bonding between the nanoparticles and aluminum is excellent, as shown in as shown in Fig. 4-5b. A strong interfacial bonding and a dense homogeneous dispersion of TiC nanoparticles, as shown in Fig. 4-4a, can result in unprecedented strengthening for the AMNC samples, which can be estimated by[157]:

$$\Delta\sigma_{load} = 1.5V_p\sigma_i \tag{4}$$

where V_p is the volume fraction of particles and σ_i is the interfacial bonding between Al matrix and TiC nanoparticles. The strong interfacial bonding as shown in Fig. 4-5b suggests that the

theoretical value of σ_i would be approximately 1000 MPa (with a hypothetical $\Delta\sigma_{load}$ at 525 MPa). It should be noted that this is purely hypothesis as there is no interfacial bonding strength data available.

4.2.4 Comparison of material performance with other engineering materials

4.2.4.1 Comparison of specific yield strength and specific modulus at room temperature with other engineering materials

Fig. 4-11 shows the specific Young's modulus and specific yield strength of the AMNC samples and other engineering alloys, indicating that the AMNC (35 vol.% TiC) exhibits the highest specific Young's modulus and one of the best specific yield strengths among all structural metals. To compare the AMNC (35 vol.% TiC) samples with other representative engineering alloys, all testing data were collected from micropillar compression tests without size effect. The diameters of testing samples were in the range of 3.5 μm to 7 μm. It should be noted that the properties reviewed were obtained by using different strain rates and the data points shown in the graph were the extreme values data presented in that reference, i.e., the highest values for the yield strength. Also, since the authors10,39 did not provide exact Young's modulus data, the data were estimated using a superposition method, which would theoretically be higher than the experimental data. The references for each material are listed as follows: Al7075 T73[166], Ultrafine-grained Al[167], Mg2Zn (14 vol.% SiC)[19], Mg10Al (1 diamondoids)[168], 316L stainless steel and 316L stainless steel (15vol.% TiB2)10[125], Duplex stainless steel[169], Ti6AI4V[170], and W7Cr9Ce[171] and Inconel MA6000[172].

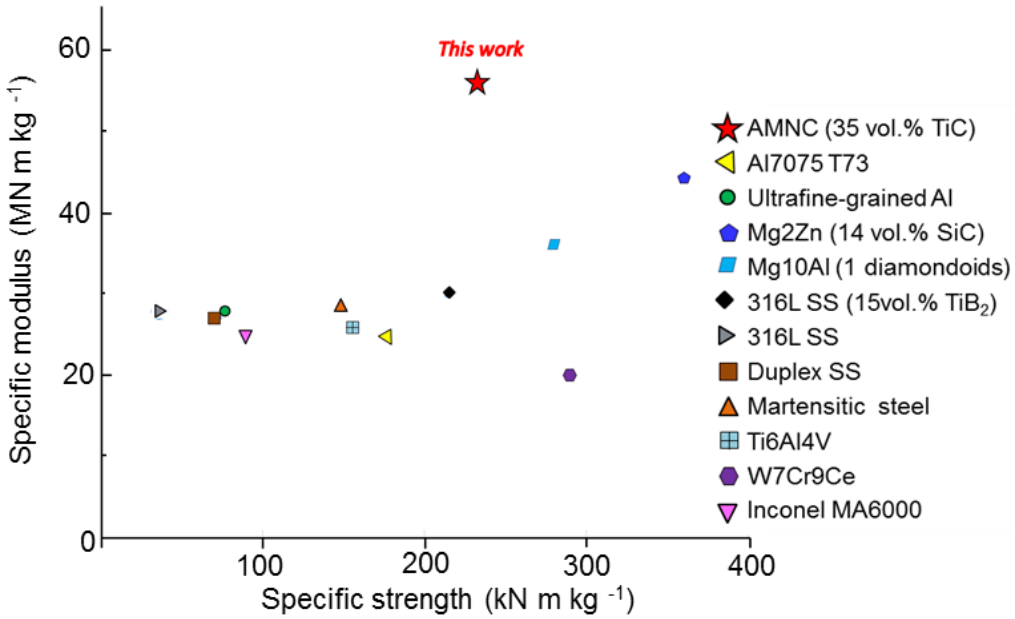

Figure 4-11: Specific Young's modulus and specific yield strength of AMNC and other materials (all data from microcompression tests without size effect)

4.2.4.2 Comparison of specific yield strength and specific modulus at room temperature with Al matrix composite materials

An extensive review of conventional aluminum matrix composites (AMCs), i.e. especially aluminum reinforced with TiC micro particles, is included in Table 4-1. All AMC-TiC composites offer much lower mechanical properties and Young's modulus than that of laser printed AMNCs. Table 4-1 summarizes the material properties of aluminum reinforced by TiC micro particles (Al-TiC composites) reported in literatures. Problems such as porosity, chemical reaction, poor wettability, poor incorporation, nonhomogeneous particle dispersion and distribution in the matrix were often observed, especially with reinforcements of smaller sizes[161,173,174]. It should be noted that even with 56 vol.% TiC micro powders incorporated into Al matrix using a pressureless infiltration technique, the elastic modulus of the Al-TiC composite is still only 170 GPa without any yield strength data[175]. It clearly shows that all Al-TiC composites offer much lower properties

and Young's modulus than that of AMNCs (with up to 35 Vol.% TiC nanoparticles), which delivered a yield strength of up to 1000 MPa, plasticity over 10%, and Young's modulus of approximately 200 GPa.

Table 4-1 | Material properties of Al-TiC composites produced by different methods

Authors	Fabrication method	Material system	Yield strength (MPa)	Elastic modulus (GPa)	Volume (%)	Weight (%)
Kennedy[176]	Casting	Al/TiC	63	89	10	-
Selcuk[177]	Casting	Al/TiC (T6)	301	84	7	10
Bauri[178]	Casting	Al/TiC	88,103,123	-	-	5
Kumar[104]	Casting	AlCu/TiC	87	-	-	10
Mazaheri[173]	Casting	Al/TiC	66	-	10	-
Shyu[179]	Casting	Al/TiC	296	94	-	-
Rai[180]	Casting	Al/TiC	80, 90, 100 (Hot rolled)	-	-	10
Wang[130]	Combustion synthesis	2009Al/TiC	120, 191, 248, 198	-	10, 15, 20, 30	-
Contreras[175]	Presureless Infiltration	Al/TiC	-	170	56	-
Mohapatra[181]	Hot Consolidation	Al/TiC	107, 180, 205	89 (20 vol.%)	5,10, 20	-

The comparison of the specific modulus and yield strength between the new AMNCs and any other aluminum-based materials (aluminum alloys and composites) is shown in Fig. 4-12. It is obvious that AMNC clearly offers the highest specific modulus and yield strength among all aluminum materials. While the microcompression tests with micropillars without size effect will offer scientifically-meaningful yield strength, Young's modulus, and uniform plasticity to characterize the laser printed AMNCs, tensile testing would pose a more serious challenge for ductility in the laser-printed samples, which heavily depends on engineering optimization. But it should be noted that uniform plasticity of about 10% in the laser-printed AMNCs is a good indication that the material can withstand some plastic deformation. For high temperature applications, the ductility may not be an issue though.

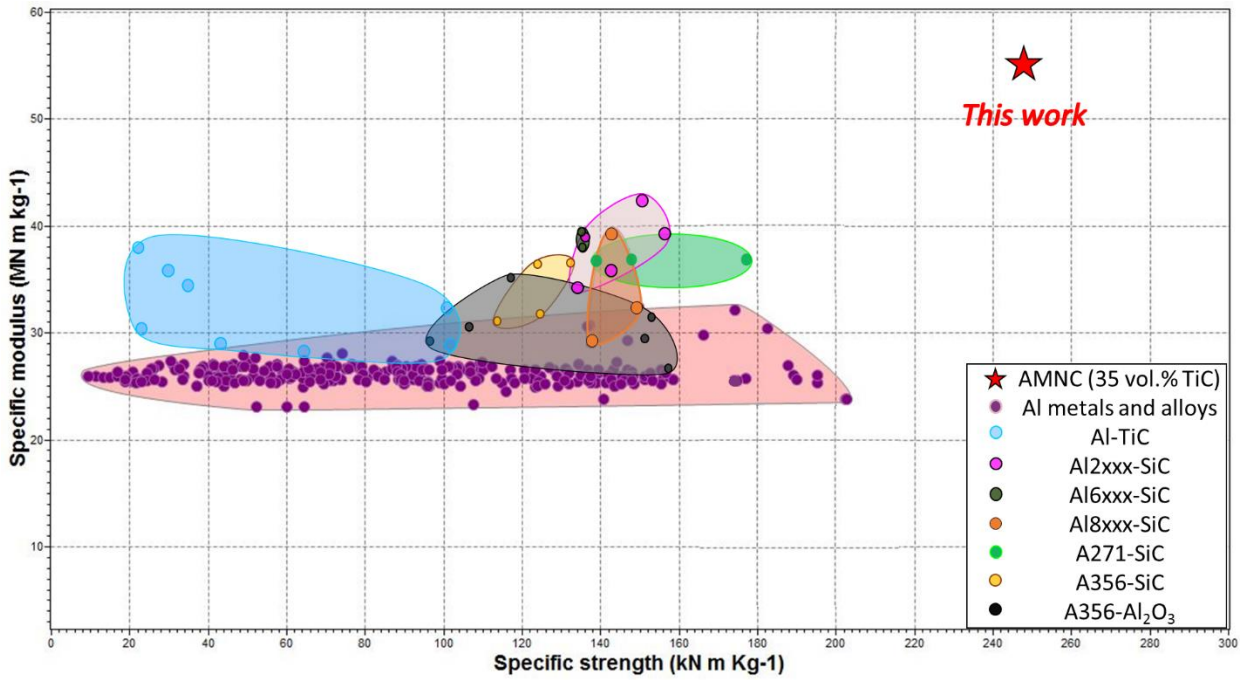

Figure 4-12: Comparison in specific Young's modulus and specific yield strength of AMNC (this work), Al alloys, and Al composites (plotted via CES Selector software, Granta Design, Cambridge, UK).

4.2.4.3 Comparison of yield stress at elevated temperature with other engineering materials.

Fig. 4-13 shows the AMNC (35 vol.% TiC) samples offer exceptional strength when compared with other engineering materials at different elevated temperatures. At 400 °C, the AMNC samples offer a higher strength than any other aluminum materials and even greater than stainless steel SS304. These results clearly suggest that super aluminum with dispersed nanoparticles deposited via laser additive manufacturing, not only exhibits yield strength and plasticity that are superior to those of previously reported Al-based materials but also provides exceptional high-temperature stability.

The yield stress at elevated temperatures is sensitive to different strain rates. It should be noted that a high strain rate typically leads to a strengthening effect. Therefore, to scientifically

compare AMNC (35 vol.% TiC) samples with other representative engineering alloys, this study also listed the strain rate data: a strain rate of 1 x 10^{-2} for aluminum alloys; of 2 x 10^{-3} for current strongest magnesium nanocomposite, and of 1 x 10^{-4} for SS304. The test of SS304 was conducted according to the ASTM Standard E21-92. For each material, the references are listed as follows: 7017 Aluminum[182], SS304[183], Mg_2Zn (14 vol.% SiC)[19], 7075 Aluminum[184], and 6061 Aluminum[185].

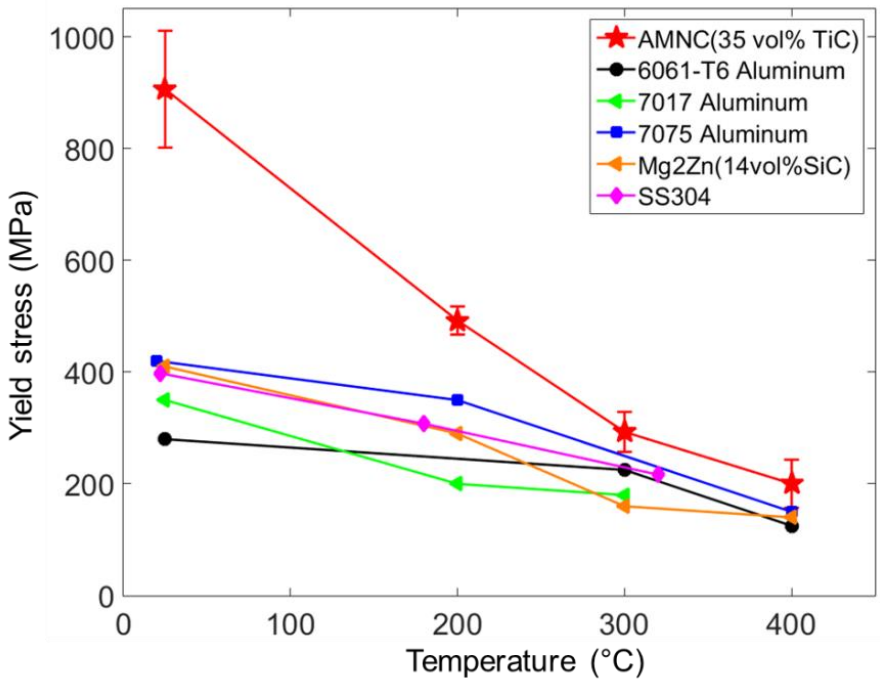

Figure 4-13: Yield strength of AMNC (35 vol.% TiC) at test temperatures of 25 °C, 200 °C, and 400 °C in comparison with other materials.

4.3 Experimental results (AMNC powders via Mechanical Mixing)

4.3.1 Microstructure

To study the microstructure of AMNC samples produced by laser melting of mechanical mixing AMNC powders, this study first conducted experiment of LAM on the powders and then

characterized the samples with SEM and FIB. Figure 4-14a shows an AMNCs sample (15 vol.% TiC) with a thickness of 513 ± 36 μm was layer-by-layer deposited by laser melting of the mechanical mixing AMNC (x=0.25) powder bed. The SEM images (Fig. 4-14a and Fig. 4-14b) were obtained from the top of the deposited sample (3 mm × 3 mm), showing the sample with a good uniformity and well bonded to the previous layers.

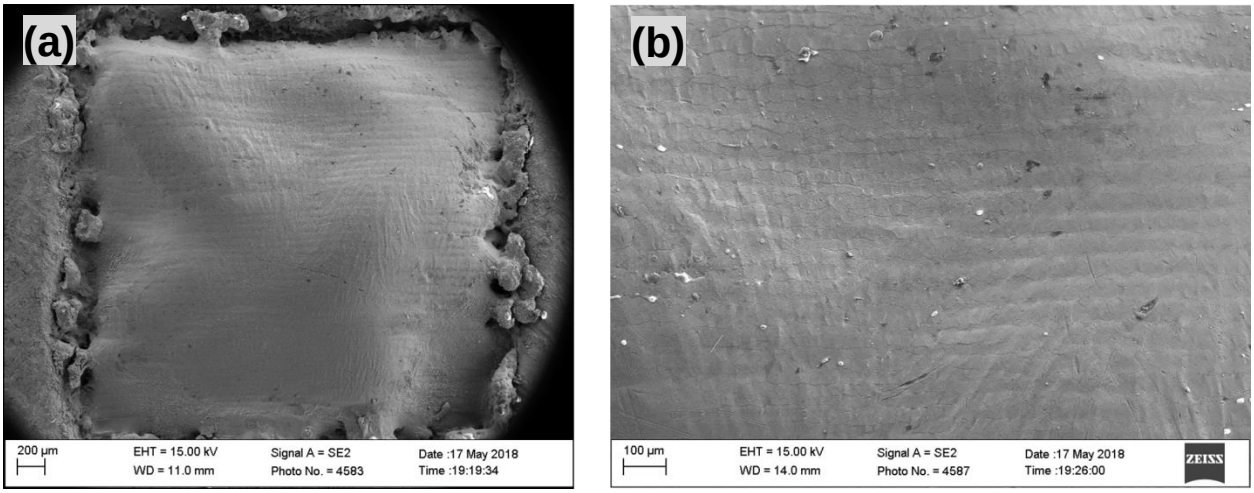

Figure 4-14: An aluminum matrix nanocomposites (AMNC) by laser melting of mechanical mixing AMNCs powder (x=0.25). a, Top view of laser-deposited AMNC (15 vol.% TiC) samples with dimensions of 3 mm × 3 mm. **b,** magnified image of **a**.

To clearly reveal the nanoparticle dispersion and distribution, the internal microstructure of AMNC sample were investigated by SEM. The SEM image in Fig. 4-15a and Fig. 4-15b without FIB etching were first acquired at a 52° tilt to reveal the overall cross-sectional image of the sample, showing that the TiC nanoparticles were distributed and dispersed uniformly in the Al matrix. Focused Ion Beam (FIB) was then used to selectively ion-mill the sample to expose the internal structure. The purpose of this step is to eliminate the concern of sample contamination potentially occurred at the step of manual polishing. Figure 4-15c and Fig. 4-15d show the SEM images of the internal microstructure after FIB milling. Clearly, it can be seen that the TiC nanoparticles is

uniformly distributed and dispersed in the Al matrix, showing similar results as the SEM images obtained without FIB cleaning.

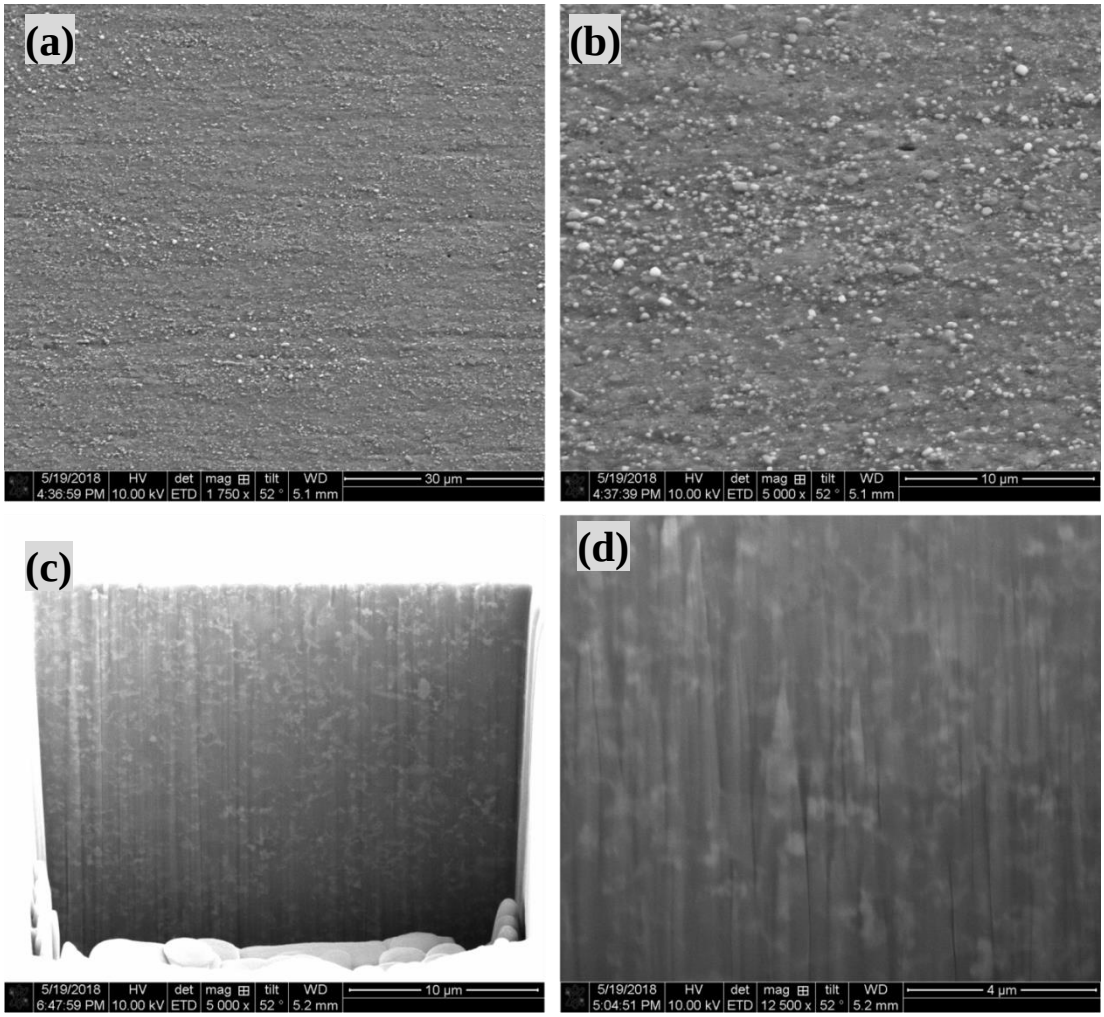

Figure 4-15: Internal microstructure of laser deposited AMNC (15 vol.% TiC). 52° tilted cross sectional SEM image of the sample **a, b,** without FIB milling and **c, d** with FIB milling.

4.3.2 Material performance

4.3.2.1 Microhardness

Figure 4-16 shows the microhardness of the AMNC sample by laser melting of two categories of AMNC powders. The average hardness of both samples are 111.8 ± 9.5 HV and 100.6 ± 6.7 HV, respectively. The AMNC (15 vol.% TiC) with lower fraction of nanoparticles has

a slightly higher microhardness than that of AMNC (17 vol. % TiC, ultrasonic processing) because the different size of dispersed nanoparticles in the samples. As observed from the microstructure analysis, the size of nanoparticles in the AMNC (17 vol.% TiC) is about 200 nm but size of nanoparticles in the AMNC (15 vol.% TiC) is less than 100 nm.

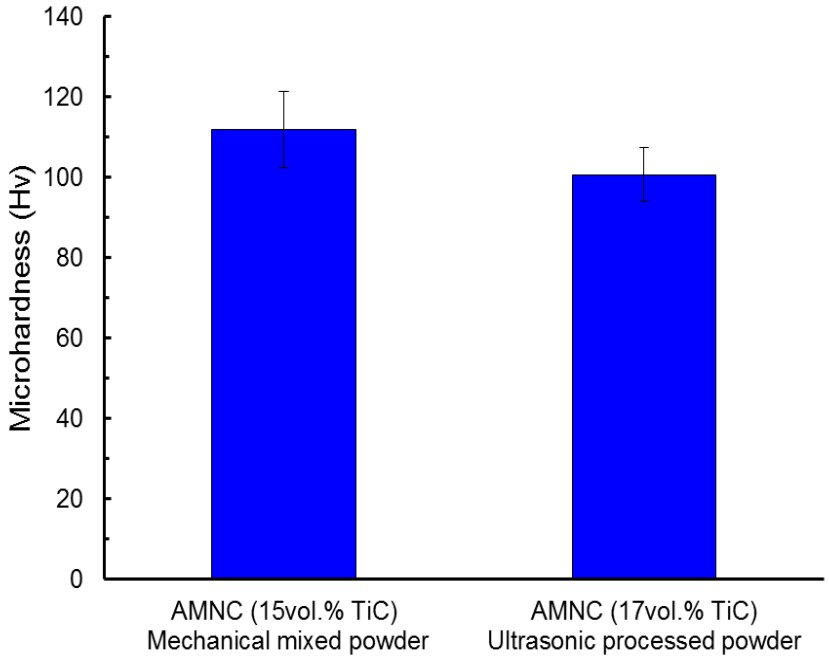

Figure 4-16: Comparison of microhardness between AMNCs produced by laser melting of two types of AMNC powders.

4.3.2.2 Young's modulus

Figure 4-17 illustrates the comparison of young's modulus of laser deposited AMMNC samples. The Young's modulus for the AMNC (15vol.% TiC) sample is about 97.2 ± 6.5 GPa whereas the young's modules the Young's modulus for the AMNC (17vol.% TiC) is approximately 108.1 ± 10.2 GPa, respectively. It is believed that the enhancement of Young's modus is attributed to the high Young's modulus of TiC (439.4 GPa), and thus the sample with the higher volume loading of nanoparticles has the higher Young's modulus.

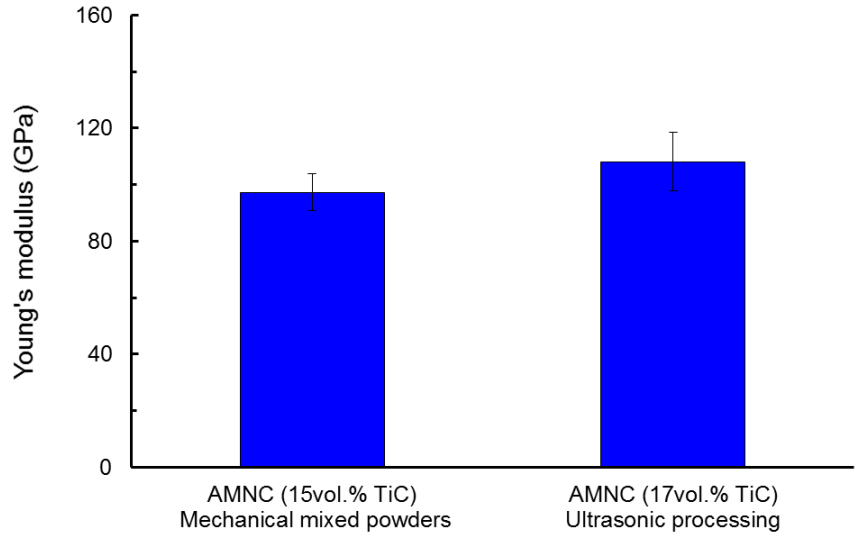

Figure 4-17: Comparison of Young's modulus between AMNCs produced by laser melting of two categories of AMNC powders.

4.4 Summary

In summary, two types of AMNC powders, i.e., ultrasonic processing and mechanical mixing, were applied for laser additive manufacturing (LAM) experiment. The laser deposited AMNC with dense dispersed nanoparticles was layer-deposited via LAM of novel ultrasonic processing AMNC powders, delivering the highest specific Young's modulus and one of the best specific yield strengths among all structural metals, as well as an unprecedented thermal stability at 400 ºC amongst all aluminum based materials.

Additionally, a layer-by-layer laser deposited AMNC sample was successfully produced by laser melting of AMNC powders produced by mechanical mixing, demonstrating mechanical properties are comparable to that of AMNC sample produced by laser melting of powders by ultrasonic processing. The new pathway for laser 3D Printing of nanoparticles reinforced aluminum can be readily extended to other materials for widespread applications.

CHAPTER 5 LASER ADDITIVE MANUFACTURING OF ALUMINUM ALLOY MATRIX NANOCOMPOSITES

5.1 Experimental method

The motivation of this study is to laser additively manufactured aluminum alloys. To benefit from strengthening effects of the secondary phase in alloy, aluminum silicon alloy was selected because of its high melt fluidity, low shrinkage upon solidification, and small solidification range[6]. It is expected that the mechanical properties of laser printed nanocomposite alloy are still maintained with less incorporated nanoparticles.

5.1.1 Laser additive manufacturing

The schematic of a customized laser additive manufacturing system is illustrated in Figure 5-1. The system was modified from the previous experimental setup, as shown in Figure 4-1. The preheating system, layer-thickness control device, and laser equipment, i.e., wavelength and power, remain the same. Instead of using the stainless vacuum chamber, a commercial standard vacuum glove bag (Aldrich AtomsBag, Aldric) was used as a transparent flexible chamber to examine the operating process. The built-in gloves enable users to work in an isolated argon protective environment. The experiment was conducted under a laser power output of 200 W, a scan speed of 0.2 m/s at continuous wave mode, a spot size of 50 μm, a hatching space of 30 μm, and a 90° scanning direction difference for each layer. A preheating of the powders was set as a temperature of 300 °C. For each cycle of laser deposition, a AlSi12-TiC powder layer (x=0.05 and 0.25) with a thickness of about 50 μm were manually deposited on the pre-machined Al 1100 alloy substrate (≥99.0%, McMaster-Carr) with a dimension of 50.8 mm × 50.8 mm × 9.5 mm. The thickness of the powder layer was manually adjusted by a customized layer-thickness control device and the z-axis manual stage. The laser focal point was set as 50 μm for each layer processing. A constant

argon flow was applied into chamber for over 60 minutes to reduce the oxygen content in the working environment. The laser scanning patterns of 3 mm × 3 mm and 8 mm × 18.5 mm were conducted at the powder layers at temperatures of 300 °C (with preheating). The layer-by-layer deposition process was repeated to obtain a designed layer thickness for fundamental study. In this study, the nanocomposite samples with thickness of approximately 200 ± 20 µm (AlSi12-TiC with x=0.05 and 0.25) were deposited for characterization. Laser processed pure AlSi12 samples with a thickness of about 120±20 µm were also obtained for comparison.

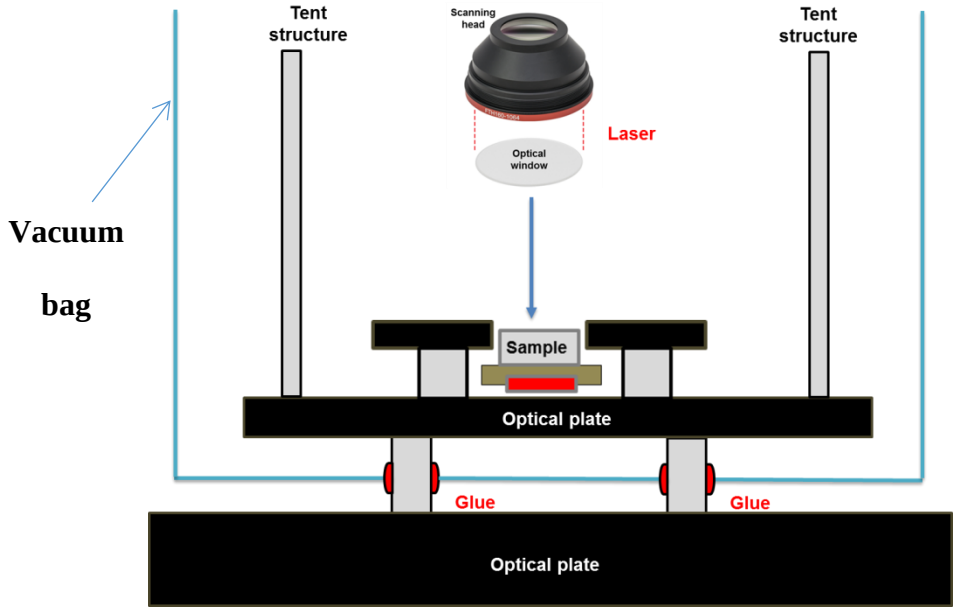

Figure 5-1: Schematic of laser additive manufacturing for $AlSi_{12}$ alloy system under argon protection (The powder layers can be manually deposited without exposure to the atmosphere)

5.1.2 Characterization

5.1.2.1 Phase identification: Phase identification of commercial AlSi12 powder and laser processed specimens were performed by X-ray diffractometer (XRD) (X'pert panalytical, U.K.)

with x ray radiation (λ = 0.1504 nm) at 40 kV and 40 mA, using a continuous scan mode at 1.0°/min. A commercial AlSi12 powder sample was tested for the comparison purpose.

5.1.2.2 Micro/nanostructure: To determine the dispersion and distribution of nanoparticles and alloy elements in the laser deposited samples, scanning electron microscopy (SEM), energy dispersive X-ray spectroscopy (EDS/EDX), focused ion beam (FIB), and transmission electron microscopy (TEM) were used. To clean the surface and reveal the grain size, the mechanical grinded and polished sample without nanoparticles was polished by low-angle ion milling (Model PIPS 691, Gatan), followed by etching with a solution consisted of sodium hydroxide (1 g), potassium permanganate (4 g), and distilled water (100 mL) for 15 s. For the laser deposited sample with nanoparticles, the sizes of the grain structure were investigated by image analysis software (Image J) from SEM and TEM micro/nanostructure analysis. The TEM samples were prepared using FIB and analyzed by Transmission Electron Microscopy (T12 Qucik CryEM and Cryo, FEI). Detailed elemental distribution of the laser deposited nanocomposite sample was characterized using Scanning/Transmission Electron Microscopy (S/TEM, Titan, FEI).

5.1.2.3 Mechanical characterization

Measurement of elastic modulus: Nanoindentation tests were performed by MTS Nanoindenter XP to evaluate the elastic modulus of the laser deposited materials. The laser processed samples with different composition of nanoparticles (x=0.05 and x=0.25) and without nanoparticles (pure AlSi12) were compressed by a Berkovich tip with an indentation depth of 2 μm. For each sample, 10 randomly selected points were measured. Elastic moduli were calculated from the unloading curves.

Measurement of hardness: Vickers hardness with a load of 50g and the dwell time of 10s was used to characterize the microhardness of the samples (AlSi12-TiC x=0.05 and x=0.25) with

and without nanoparticles (AlSi12). A total of five points were measured at different locations for each sample for the average value of microhardness.

5.2 Experimental results

5.2.1 Phase analysis (XRD) -Alloying elements-nanoparticle Interaction

The XRD patterns of laser processed sample were depicted in Fig. 5-2. The strong diffraction peaks corresponding to aluminum and silicon were identified in the commercial AlSi12 powder sample, whereas the diffraction peaks of titanium aluminum (Al_3Ti), silicon carbide (SiC) were shown in the nanocomposite sample, revealing that chemical reaction occurred in the nanocomposite sample after laser processing. The Si diffraction peaks in nanocomposite became weaker in the intensity, implying that the chemical formation of SiC phase during laser processing. Strong peaks of Al_3Ti were also observed in the nanocomposite sample. It is very likely the total chemical reaction is shown as follows,

$$3Al + Si + TiC = Al_3Ti + SiC\ \Delta H \ll 0$$

, where $\Delta H$is reaction enthalpy.

The reaction rates of each system can be estimated by Arrhenius equation as follows,

$$k = Ae^{\frac{-Ea}{k_B T}}$$

, where k is the rate constant, T is the absolute temperature, A is the constant for each reaction, E_a is the activation energy, and K_B is the Boltzmann constant. From the Arrhenius equation a higher reaction enthalpy of the phase results in the greater formation tendency. As shown in Table 5-1, the reaction enthalpy of potential system (1), (2), and (3) are -66.94 KJ/mol, -184 KJ/mol, and -300 to -310 KJ/mol, respectively. Therefore, the formation rate estimated by Arrhenius

relationship reveals that Al_3Ti can have a greater formation tendency than SiC due to higher enthalphy.

$$TiC = Ti + C\ \Delta H = +184\ KJ/mol \text{ (1)}$$

$$Si + C = SiC\ \Delta H = -66.94\ KJ/mol \text{ (2)}$$

$$3Al + Ti = Al_3Ti\ \Delta H \cong -300\ KJ/mol \text{ (3)}$$

It is possible that Si phase react with TiC nanoparticles during laser processing, followed by the formation of SiC and Al_3Ti phase. As shown in Table 5-1, The TiC phase and resultant SiC phase have relatively higher bond disassociation energies, i.e., 435 KJ/mol and 430 KJ/mol, than Al_3Ti (250-260 KJ/mol), suggesting that the greater amount of energy that is required to break the phase. Detailed micro and nanostructure characterization about these phases will be discussed in the following section.

Table 5-1 Energies of potential reaction system from temperature of 1500 to 2000°C

Reaction System (~1500-2000°C)	Reaction Enthalpy (KJ/mol)	Bond Disassociation Energy between Elements (KJ/mol)
$Si + C = SiC$	-66.94[186]	435[187]
$Ti + C = TiC$	-184[188]	430[189]
$3Al + Ti = Al_3Ti$	-300~310[190]	250-260[191]

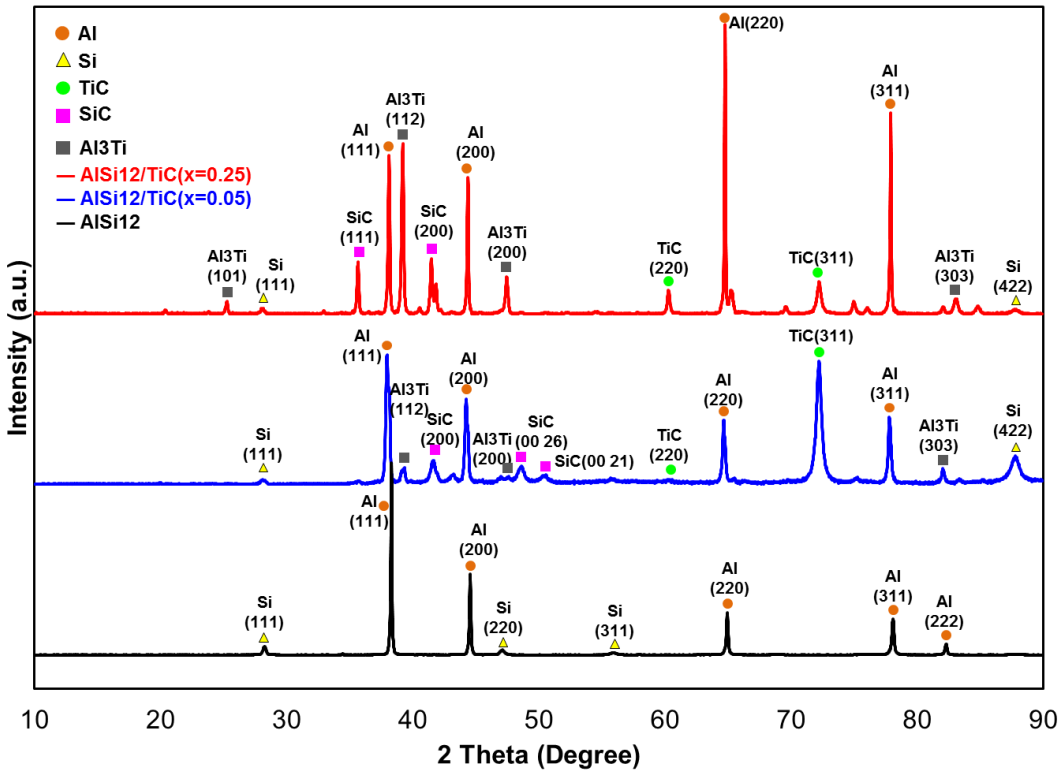

Figure 5-2: XRD spectra of laser deposited AlSi12 sample with and without TiC nanoparticles

5.2.2 Micro/Nanostructure

5.2.2.1 Laser processed AlSi12

A laser deposited AlSi12 sample without nanoparticles was obtained for comparison purpose. To reveal the microstructure, the sample was chemically etched for 15 second (See experimental method at section 5.1.2.2). The large thermal gradient and undercooling induced by laser processing, the preferred solidification microstructure is the eutectic Al/Si structure[192]. As shown in Fig. 5-3, the Si phases (gray spots) were observed throughout the microstructure after

the sample was chemically etched. The average grain size is approximately 4.0 ± 0.9 μm. Due to the limited sample size, this study mainly focuses on studying the overall grain structure evolution without particularly investigating coarsened grain areas such as molten pool boundaries. It would be more interesting to investigate the grain structure evolution among different regions, e.g., molten zone, heated affected zone, overlapping zone, if the bulk samples can be obtained in the future.

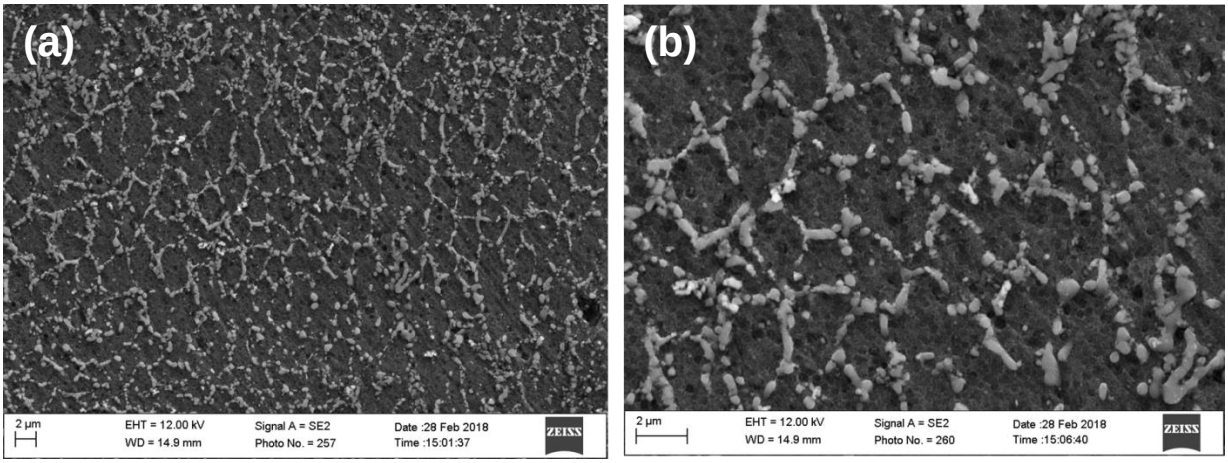

Figure 5-3: Microstructure of laser processed AlSi12 with different magnification.

5.2.2.2 Laser processed AlSi12-TiC with x=0.05

It is well accepted that the microstructure of matrix can be refined after the incorporation of nanoparticle. We designed 5 vol.% of TiC nanoparticles incorporated in AlSi12 powders and further conducted experiment on LAM by melting these nanoparticle reinforced powders, i.e., AlSi12-TiC with x=0.05. The microstructure of the laser deposited AlSi12 sample with TiC nanoparticles, i.e., $AlSi_{12}$-TiC (x=0.05), was characterized with scanning electron microscopy (SEM) and focused ion beam (FIB). The bright phases shown in Fig. 5-4a and Fig. 5-4b are the TiC nanoparticles, which are uniformly distributed in the dark AlSi12 matrix. From the magnified image (Fig. 5-4b), the bright TiC nanoparticles tend to distributed at grain boundary to form fine ring structures. To eliminate the concern of potential contaminants on the microstructure, Focused

Ion Beam (FIB) was applied to selectively cut through the sample. The images were then acquired at a 52° tilt to expose the nanoparticle distribution in the AlSi12 matrix. As shown in Fig. 5-4c, similar to the results of Fig. 5-4b, the TiC phases were mainly formed at grain boundary and Si elements were clearly observed in the Al matrix. The grain size is approximately of 2.1 ± 0.7 μm, showing a slight grain refinement of the microstructure. It is possible that the small fractions of nanoparticles are not sufficient enough to significantly refine the microstructure.

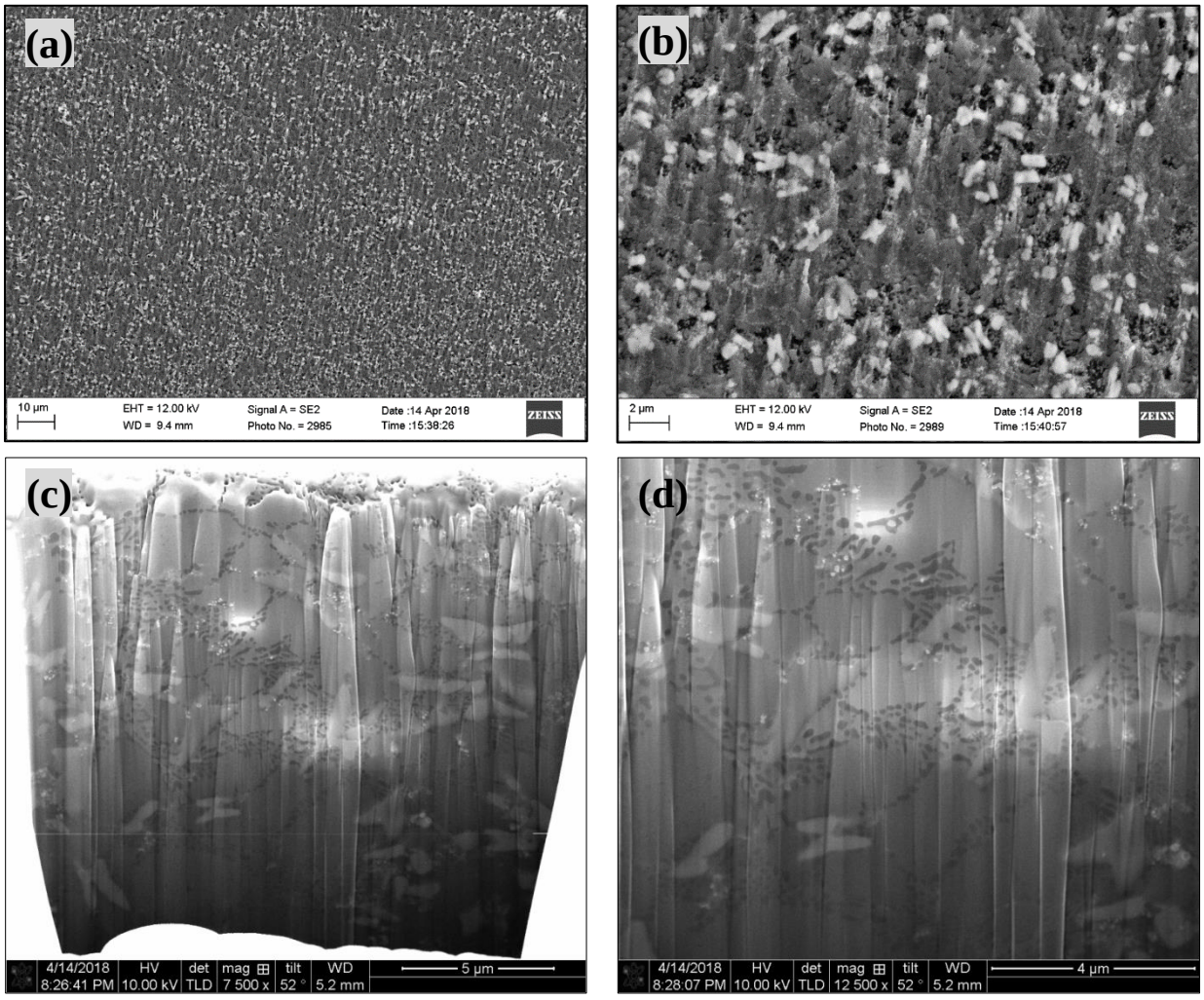

Figure 5-4: Laser deposited AlSi12-TiC (x-0.05) nanocomposite sample. a, cross-sectional SEM image. **b,** Magnified image of a. **c,** 52° tilted cross-sectional SEM images. **d,** Magnified image of **c**.

5.2.2.3 Laser processed AlSi12-TiC with x=0.25

A higher amount of nanoparticles into the matrix was designed to study the effects of nanoparticles on AlSi12 microstructure. SEM and FIB were again applied for sample characterization after sample was chemically etched. The cross sectional images of the sample were shown in Fig. 5-5a and Fig. 5-5b. The bright spots were first determined as Ti phase from

EDS analysis, and then further confirmed as TiC nanoparticles by atomic scale elemental mapping under TEM characterization (See image of Fig. 5-7c at the following section). While the TiC nanoparticles are well distributed throughout the sample, little amount of dendrites were observed, implying the chemical reaction occurred during the layer-by-layer laser processing. From the image of Fig.5-5b, it is surprised that a significant amount of intermetallic phases, i.e., gray color below TiC, were distributed uniformly in the sample. To confirm the phase, two TEM samples were prepared using FIB for the nanostructure characterization.

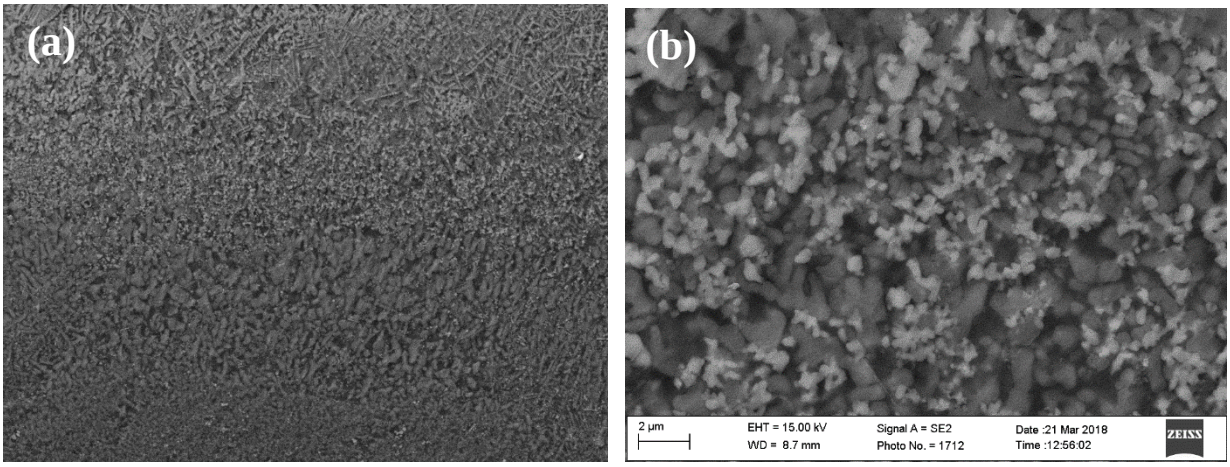

Figure 5-5: Laser deposited AlSi12-TiC (x=0.25) nanocomposite. a, cross-sectional SEM image. **b,** Magnified image of **a.**

Micro and nanostructure analysis identified four different phases, i.e., Al, Al_3Ti, TiC, and SiC, which agreed with the results of XRD analysis. Most of the SiC nanoparticles (Fig. 5-6b and Fig. 5-6d) with a size less than 100 nm were distributed around the Al_3Ti phase, indicating the original Si phase in AlSi12 powder first chemically reacted with TiC nanoparticles during the laser processing, followed by the formation of Al_3Ti phases and SiC nanoparticles. It should be noted that not all of the TiC nanoparticles were fully reacted away and thus some of TiC phase were still observed, as shown in Fig. 5-6b.

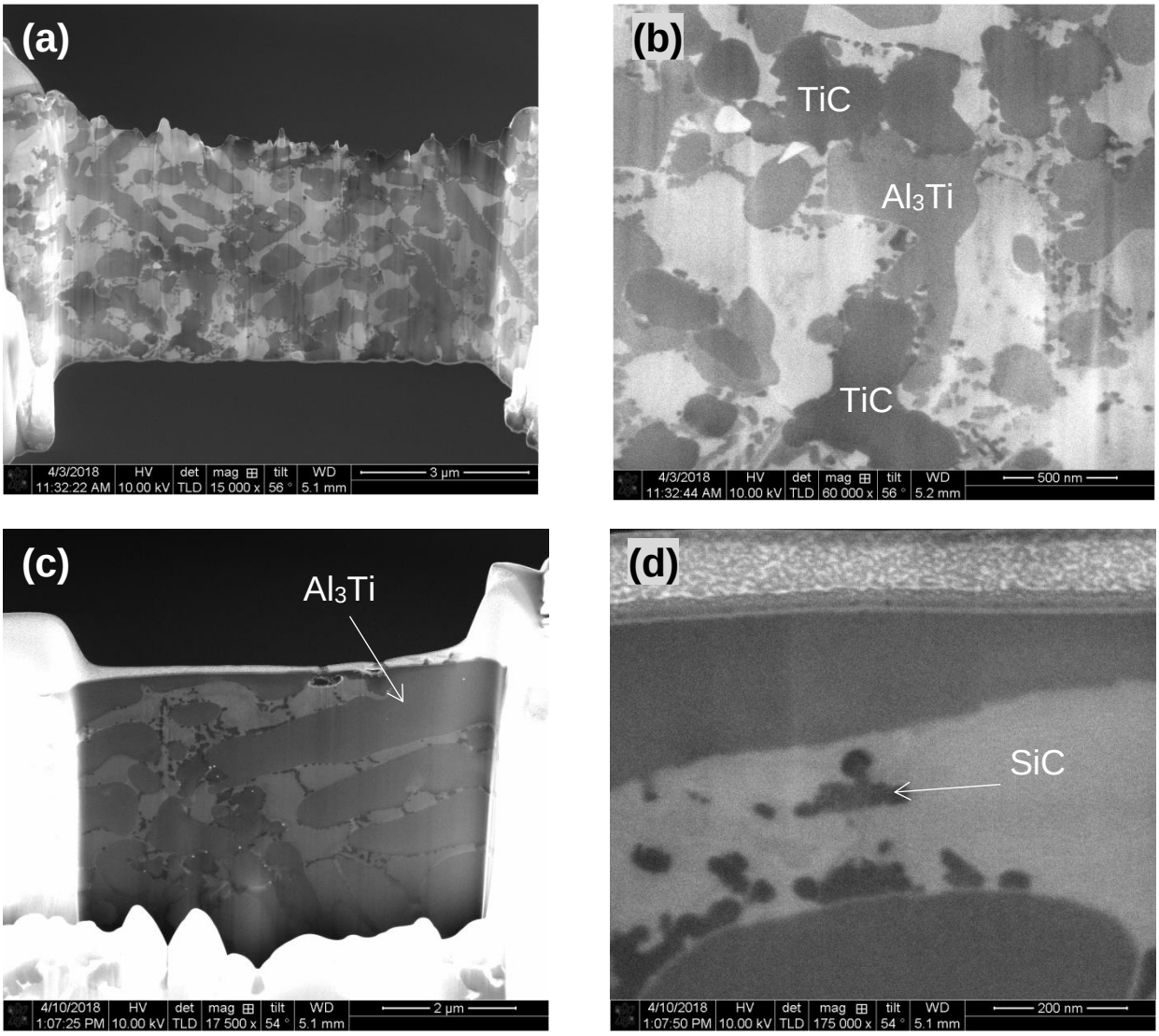

Figure 5-6: Microstructure characterization of laser processed AlSi12-TiC (x=0.25). a, c, Thin sliced $AlSi_{12}$-TiC (x=0.25) samples prepared by FIB. The samples of **a** and **c** with a thickness less than 100nm were cut from random locations at Fig. 5-5a. **b, d,** Magnified images of **a** and **c**.

To study the phase distrubtion, in depth nanostructre characterzation was performed using TEM (Titan, FEI). Figure 5-7 reveals the elemental distrubtion and the correpsonding EDS mapping image. The nanostrucutre TEM image shows the SiC nanoparticles were distributed around the Al_3Ti phase closely and a TiC nanopartcile was observed in the image. It should be

noted that the image of Fig. 5-7c was taken from the opposite direction under TEM characterization due to the sample mounting.

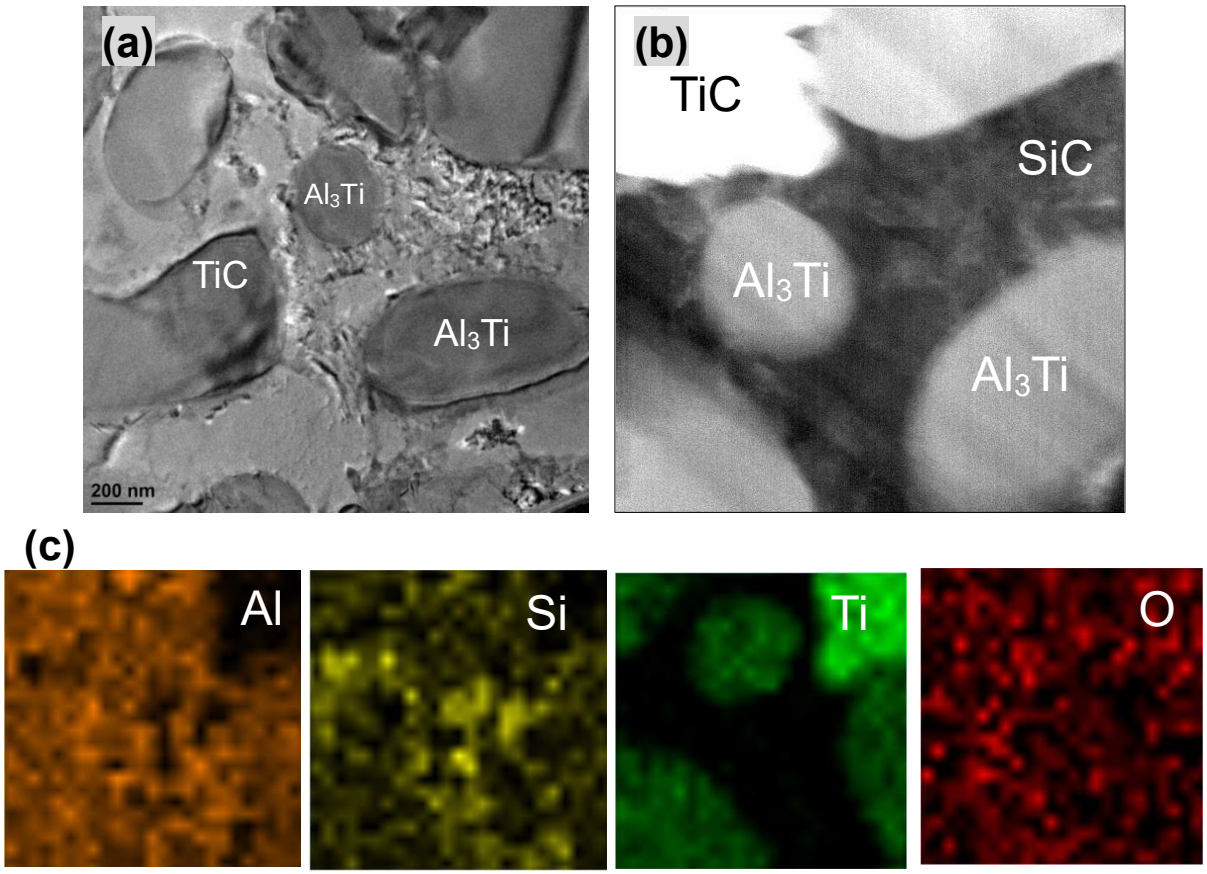

Figure 5-7: Nanostructure characterization of laser processed AlSi12-TiC (x=0.25). a, A bright-field TEM image shows the sample consists of four major phases, i.e., Al, Al_3Ti, TiC and SiC. **b,** Magnified image of **a**. Al_3Ti phases were surrounded by SiC nanoparticles. **c,** Elemental maps of **c.**

5.2.2.4 Summary of grain sizes for laser deposited sample

The grain sizes of the laser deposited sample with and without nanoparticles are illustrated in Fig. 5-8. The average grain size of laser deposited AlSi12 sample is estimated to be 4.0 ± 0.9 μm, whereas the average grain size for the AlSi12-TiC with x=0.05 and x=0.25 are about 2.1 ± 0.6 μm and 450 ± 200 nm, respectively. The grain size measurements show that the grain sizes of

AlSi12 nanocomposite decreases as the fraction of incorporated nanoparticles increases. Nanostructure analysis reveals a variation of grain size (about 200 nm) from the AlSi12-TiC (x=0.25) sample. The variation could be explained by the chemical reaction during the laser processing. It is possible that the reaction products also influenced the grain structure during the rapid solidification.

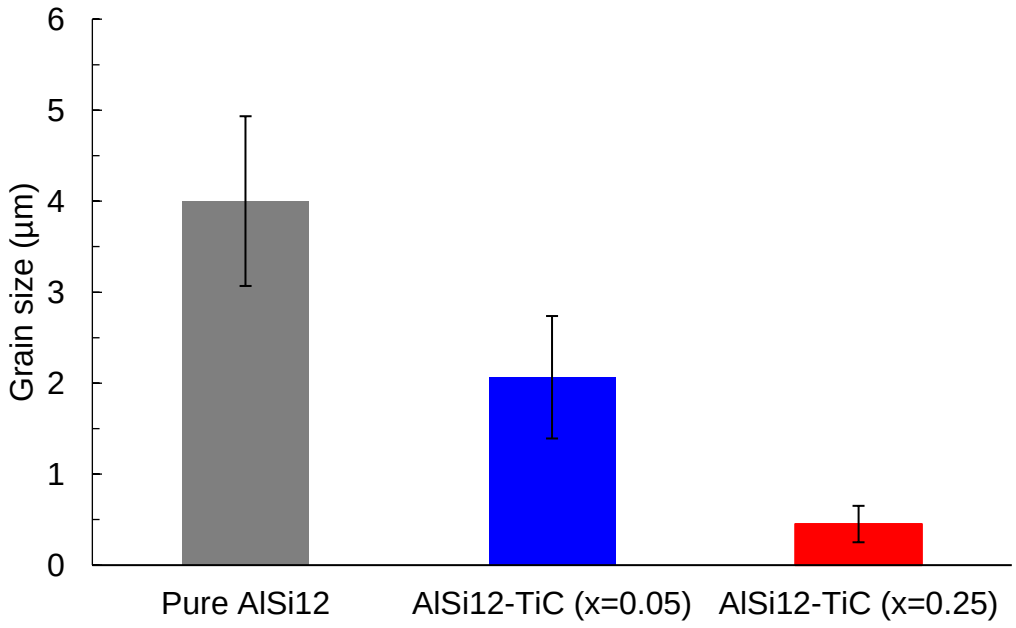

Figure 5-8: Comparison of grain size between samples with and without nanoparticles.

5.2.3 Mechanical properties

5.2.3.1 Microhardness

Figure 5-9 shows the microhardness of the AlSi12 sample with and without nanoparticles. The hardness of AMNCs was added into the figure for comparison. The average hardness of the laser deposited AlSi12 and AlSi12-TiC (x=0.05 and x=0.25) are 53.6 ± 1.41 HV, 150.0 ± 9.4 HV, and 578 ± 42.5 HV, respectively. Surprisingly, the laser deposited AlSi12-TiC (x=0.25) offers a significant higher hardness, i.e., over one order of magnitude, compared to that of pure AlSi12

sample and even the sample incorporated with 35 volume percent of TiC nanoparticles, i.e., AMNC (35 vol.% TiC). Based on the phase analysis (XRD) and micro/nanostructure examinations, it is very likely that the SiC nanoparticles and rich amount of Al_3Ti intermetallic phases contribute to the hardness of the sample.

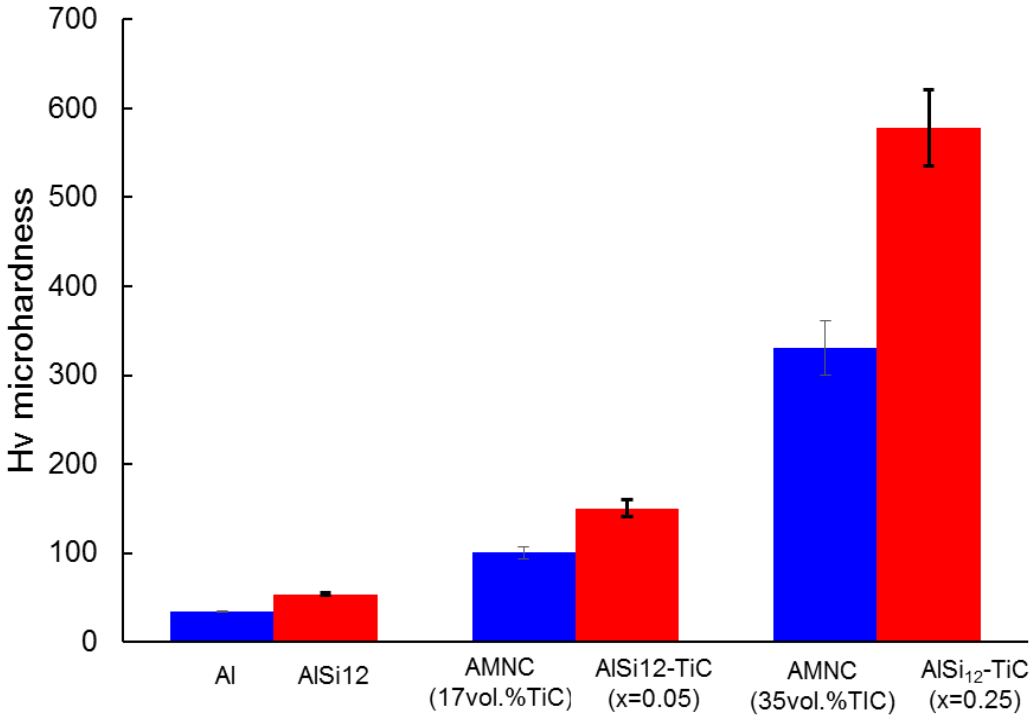

Figure 5-9: Comparison of microhardness between samples of AMNCs and AlSi12-TiC.

5.2.3.2 Young's modulus

The Young's modulus of the laser-deposited AlSi12-TiC samples is significantly increased compared to that of pure $AlSi_{12}$ aluminum, as illustrated in Fig. 5-11. Again, Young's modulus of AMNC samples and pure aluminum sample were added into the figure for comparison purpose. Whereas the pure AlSi12 sample has a Young's modulus of 70 ± 2.5 GPa, the AlSi12-TiC (x=0.05 and x=0.25) samples offer a Young's modulus of 93.9 ± 5 GPa and 187.73 ± 28 GPa, respectively. The AlSi12-TiC sample with x=0.25 exhibits a comparable Young's modulus to the AMNCs (35

vol.% TiC) possibly because of the contribution of resultant SiC nanoparticles and the intermetallic phase.

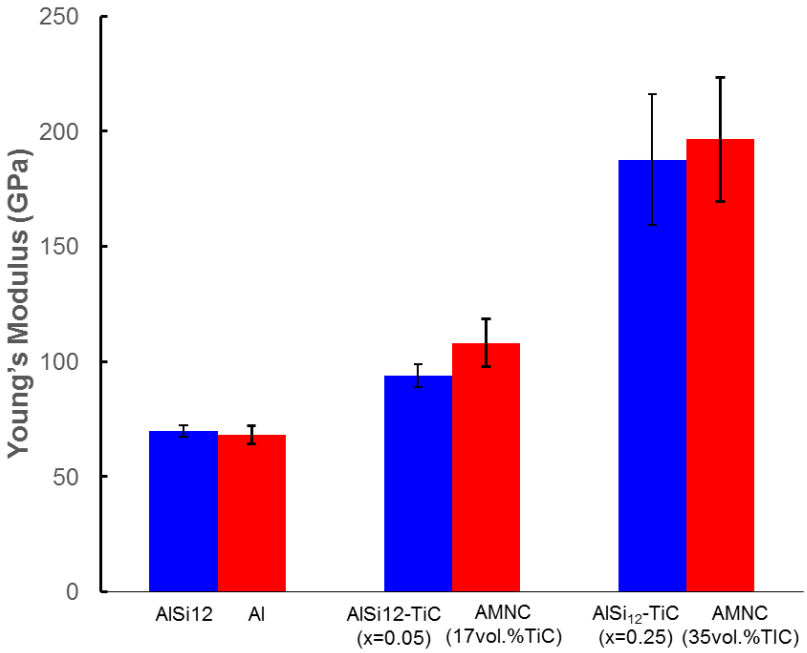

Figure 5-10: Comparison of Young's modulus between samples of AMNCs and AlSi12-TiC.

5.3 Summary

This study was motived by benefiting from strengthening effects of the secondary phase in aluminum-silicon alloy to achieve comparable mechanical properties of AMNCs with less nanoparticles. The laser deposited AlSi12 alloys with and without nanoparticles were successfully deposited. The nanoparticle effects on alloy phase were investigated by XRD, SEM and TEM. The mechanical properties of the samples were compared with those of AMNC samples. Samples with different fractions of nanoparticles, i.e., x=0.05 and 0.25, were successfully laser deposited to achieve comparable mechanical properties to those of AMNC samples. Micro/nanostructure analysis reveals that the grain size of AlSi12 nanocomposites decreases as the fraction of incorporated nanoparticles increases. However, some reaction products, i.e., SiC and Al_3Ti, have been observed from the laser deposited AlSi12 nanocomposite samples, suggesting a chemical

reaction occurred during the laser processing. More fundamental studies and careful processing parameters are needed to optimize the LAM of aluminum alloy system.

CHAPTER 6 LASER ADDITIVE MANUFACTURING OF COPPER MATRIX NANOCOMPOSITE

6.1 Experimental method

Laser additive manufacturing offers a great possibility to build metals with complex shape and high material performance. However, a great challenge to directly deposit dense copper with high mechanical properties still exists due to the high laser reflectivity and thermal conductivity of copper. This study is to study laser additively manufacturing of high performance copper matrix materials. The laser absorption and mechanical properties of deposited samples are expected to improve by incorporation of nanoparticles into the Cu matrix.

6.1.1 Laser additive manufacturing experiments

The laser additive manufacturing experiments for copper matrix nanocomposite were conducted by the LAM system as shown earlier in Figure 5-1. The experiment was conducted under a laser power output of 200 W, a scan speed of 0.1 m/s at continuous wave mode, a spot size of 50 μm, a hatching space of 30 μm, and a 90° scanning direction difference for each layer. A preheating of the powders was set as a temperature of 250 ℃. For each cycle of laser deposition, a Cu-WC powder layer (x=0.1, 0.25 and 0.66) with a thickness of about 50 μm were manually deposited on the pre-machined substrates of pure copper, Cu-11vol%WC, or nickel with a dimension of 25.0 mm × 30.0 mm × 2.0 mm. The thickness of the powder layer was manually adjusted by a customized layer-thickness control device and the z-axis manual stage. The laser focal point was set as 50 μm for each layer processing. A constant argon flow was applied into chamber for over 60 minutes to reduce the oxygen content in the working environment. The laser scanning patterns of 3 mm × 3 mm was conducted at the powder layers at temperatures of 250 °C (with preheating). The layer-by-layer deposition process was repeated to obtain a designed layer

thickness for fundamental study. In this study, the Cu-12vol%WC nanocomposite samples deposited on a pure copper substrate or a copper matrix nanocomposite substrate have an average thickness of approximately 423.0 ± 86 μm and 150.6 ± 27 μm, whereas the samples deposited on the pure nickel substrate have the thickness of about 103.4 ± 3.3 μm, 269.8 ± 6.2 μm and 188.2 ± 22.2 μm (Cu-WC, x=0.1, 0.25 and 0.66), respectively.

Preparation of as-cast Cu-11vol%WC nanocomposite: An as-cast Cu-11vol.%WC nanocomposite sample was produced using a direct molten salt assisted self-incorporation method. The WC nanoparticles (US Research Nanomaterials, 150-200 nm) were mixed with $KAlF_4$ powders with a volume ratio of 1 to 9 by a mechanical shaker (SK-O330-Pro) for 20 minutes. During the casting process, pure copper was first melted at a temperature of 1200 °C by an induction heater, followed by adding the mixture of WC nanoparticles and $KAlF_4$ powders into the melt. The whole casting process was then conducted at 1200°C under an argon protection for 30 minutes before the melt was cooled down to room temperature in the furnace. A thin MMNC substrate with a thickness of 2.0mm was obtained from the as-cast Cu-11vol.%WC via wire electro discharge machining (wire-EDM)

6.1.2 Characterization

6.1.2.1 Thermal conductivity of the substrate

The thermal conductivity of the substrate was measured by laser flash method[193]. The rectangular shape of samples with a diameter of 2mm and a length of 20mm were prepared and irradiated by a laser pulse from the front side. The transient temperature on the back side is captured recorded by a data acquisition device (USB-6003, National Instruments). The time to reach to the half of the maximum temperature change can be obtained from the temperature history and used to estimate the thermal conductivity.

6.1.2.2 Micro/nanostructure

Scanning electron microscopy (SEM), energy dispersive X-ray spectroscopy (EDS/EDX), and focused ion beam (FIB) were used to determine the WC nanoparticles dispersion and distribution in the laser processed samples. To reveal the grain size, a detector of Channel Detection Electron Multiplier (CDEM) equipped in the SEM/FIB system (Nova 600, FEI) was used to characterize the polished samples. The sizes of the grain structure were investigated by image analysis software (Image J) from CDEM images.

6.1.2.3 Mechanical characterization

Measurement of elastic modulus: Nanoindentation tests were performed by MTS Nanoindenter XP to evaluate the elastic modulus of the laser processed materials. The laser processed nanocomposite samples with different volume loadings of nanoparticles (x=0.1, 0.25, and 0.66) were compressed by a Berkovich tip with an indentation depth of 2 μm. For each sample, 10 randomly selected points were measured. Elastic moduli were calculated from the unloading curves.

Measurement of hardness: Vickers hardness with a load of 1.9N and a dwelling time of 10s was used to characterize the microhardness of the nanocomposite samples (Cu-WC x=0.1, 0.25 and 0.66). A total of five points were measured at different locations for each sample for the average value of microhardness.

6.2 Experimental results

6.2.1 Microstructure characterization

6.2.1.1 Laser deposited Cu matrix nanocomposite on pure copper substrate

From literature it is well known that it is extremely difficult to directly deposit dense copper parts by laser additive manufacturing (LAM) due to the high laser reflectivity and thermal

conductivity of copper (about 386.3 ± 23.5 W/(m·K)). Adding nanoparticles into copper matrix powders is expected to improve the laser beam absorption during LAM. The reflectivity results at the typical wavelength of LAM, i.e., 1070 nm, have been measured in Chapter 3. Experiments of LAM on Cu matrix nanocomposite were carried out using customized LAM system by selectively melting of Cu-WC nanocomposite powders on different substrates, followed by microstructure characterizations and mechanical properties of the resulting samples. Figure 6-1a shows a SEM image was captured from the top of the laser deposited Cu-WC nanocomposite sample, i.e., Cu-12 vol.%WC. A close examination of microstructure, as shown in Fig. 6-1b, reveals that the surface of the sample consisted of a number of porosities (about 200 μm) with a ball-liked morphology, which was regarded as a typical defect observed from LAM of copper[48,61]. As a consequence, irregular shapes with porosities have been observed from the cross section of the sample, as shown in Fig. 6-2a. Further improvement is possible by increasing the concentration of nanoparticles or optimizing the processing parameters such as laser energy density, preheating temperature, scanning patterns and so on.

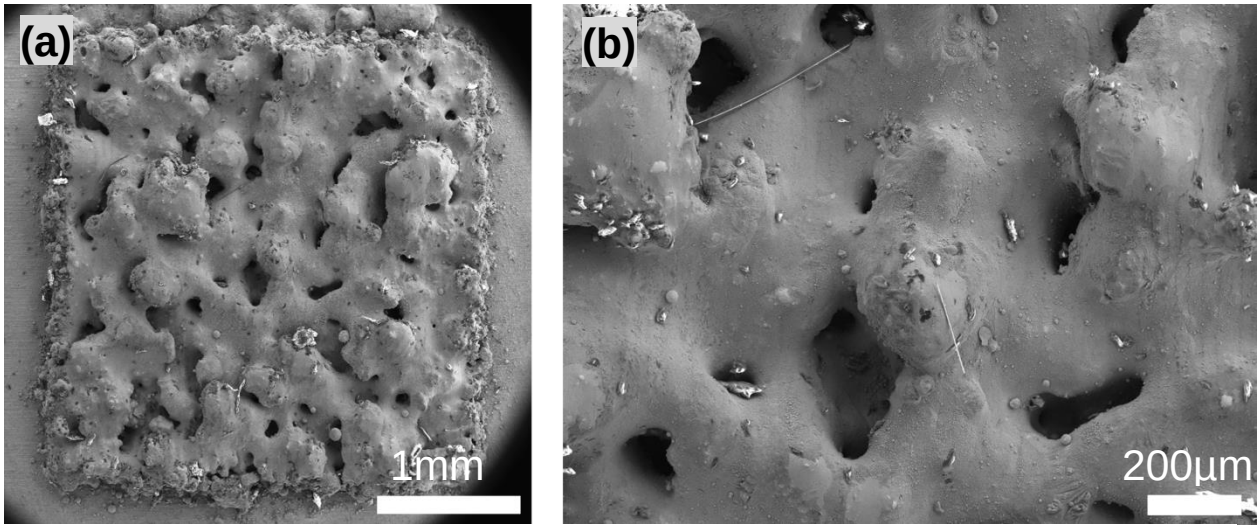

Figure 6-1: Laser deposited Cu-12vol.%WC nanocomposite sample on a pure copper substrate.

The characteristic internal microstructure of the laser deposited Cu-12vol.%WC is shown in Fig. 6-2, revealing a well distribution of WC nanoparticles throughout the Cu matrix. The white spots in the image are WC nanoparticles, which are confirmed by EDS analysis. A magnified image (Fig. 6-2b) was obtained from Fig. 6-2a, showing a well dispersion of WC nanoparticles. We also observed clusters in the sample, which can be attributed to the laser processing parameters (energy density, scan speed, beam size) or the powders morphology (size distribution, reflectivity, nanoparticle dispersion and distribution). Since the nanocomposite powders have less uniform nanoparticles distribution and dispersion (Fig. 3-12), the clusters are very likely occurred after the laser melting.

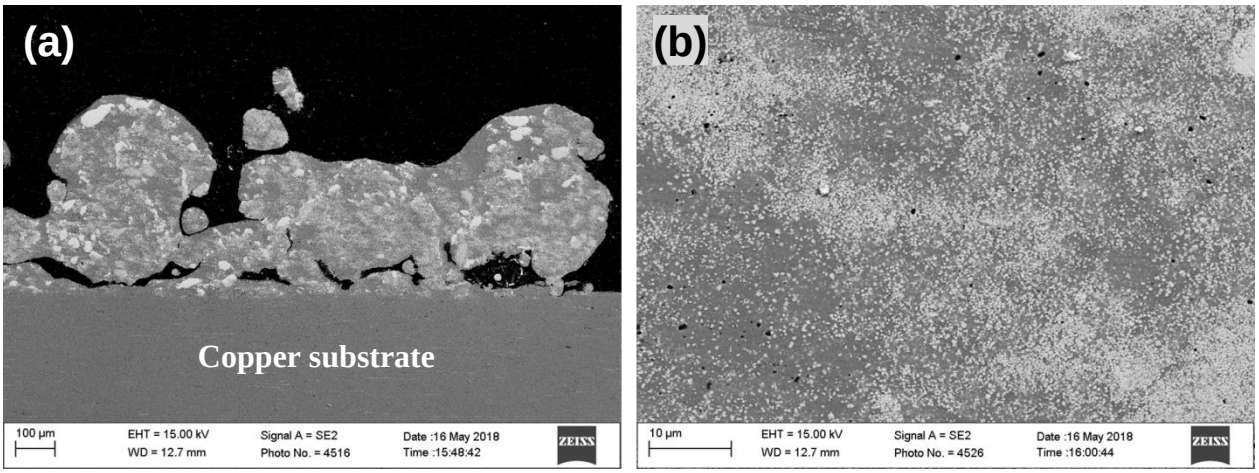

Figure 6-2: Internal microstructure of Cu-12vol.%WC.

6.2.1.2 Laser deposited Cu matrix nanocomposite on copper matrix nanocomposite substrate

To improve the layer uniformity, an as-cast Cu-12vol.%WC MMNC sample was selected as a substrate for the LAM. It is believed the lower thermal conductivity of MMNC (about 304.1 ± 2.3 W/(m·K)) can further decrease the thermal gradient between the powder bed and the surface of the substrate during the laser processing. As shown in Fig. 6-3a and Fig. 6-3b, the SEM images captured from the top of the Cu-12vol.%WC reveal a better layer uniformity than that of the sample deposited on the pure copper substrate (Fig. 6-1a). Further characterization of internal microstructure shows similar characteristics of nanoparticles dispersion and distribution. Again the nanoparticles were uniformly distributed and dispersed, as shown in Fig. 6-3d, but some agglomeration of nanoparticles were also observed.

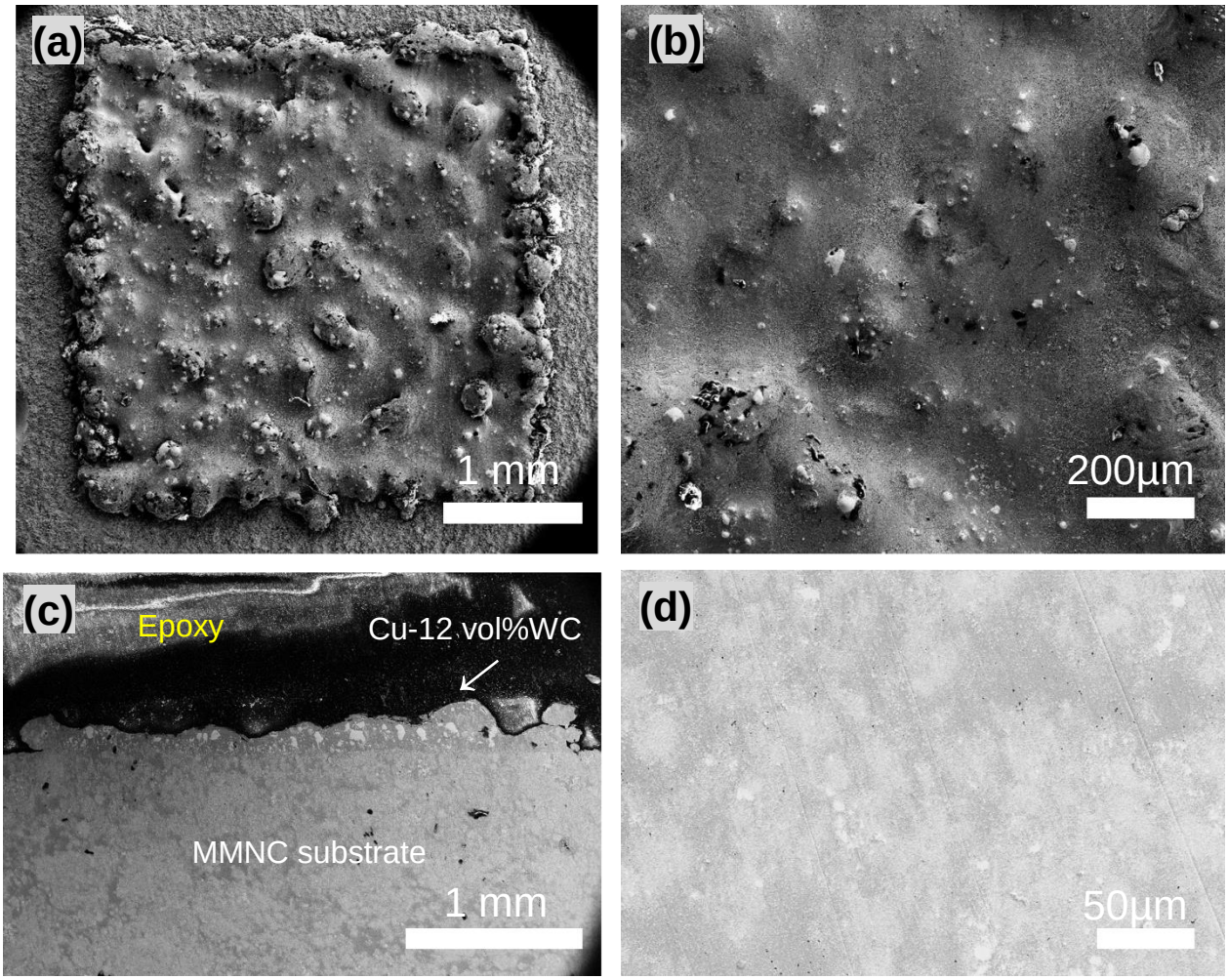

Figure 6-3: Laser deposited Cu-12vol.%WC nanocomposite sample on a copper MMNC

6.2.1.3 Laser deposited Cu matrix nanocomposite on pure nickel substrate

The results presented in previous section suggest that using a pure copper as a substrate may be too difficult to obtain uniform laser deposited layers. The pre-placed powders cannot be sufficiently melted by laser, resulting in an extensive amount of porosities and balling phenomenon. It is very likely that the MMNC substrate with a lower thermal conductivity helps the layer uniformity. Therefore, a pure nickel was selected as the substrate to improve the layer uniformity because of its well wettability with copper but a lower thermal conductivity (91.7 ± 2.8 W/m·K[21]. Figure 6-3a shows a cross sectional image of the laser deposited Cu-WC (x=0.1) nanocomposite

deposited on the pure nickel substrate. The nanoparticles were distributed throughout the sample but some clusters were also observed, which could be explained by the nanocomposite powders with relatively non-uniform nanoparticle dispersion and distribution. In addition, that the larger size of WC nanoparticles with about 200 nm (Fig.6-4c) are mainly located at the nickel substrate whereas the smaller size (Fig.6-4d) was observed at the regions where from far the nickel substrate. It is mainly due to the re-melting processes during the layer-by-layer process. While the surface morphology has been improved, i.e., no significant porosities at the surface, the porosities with about 2 µm to 5 µm have been observed from the internal microstructure characterization.

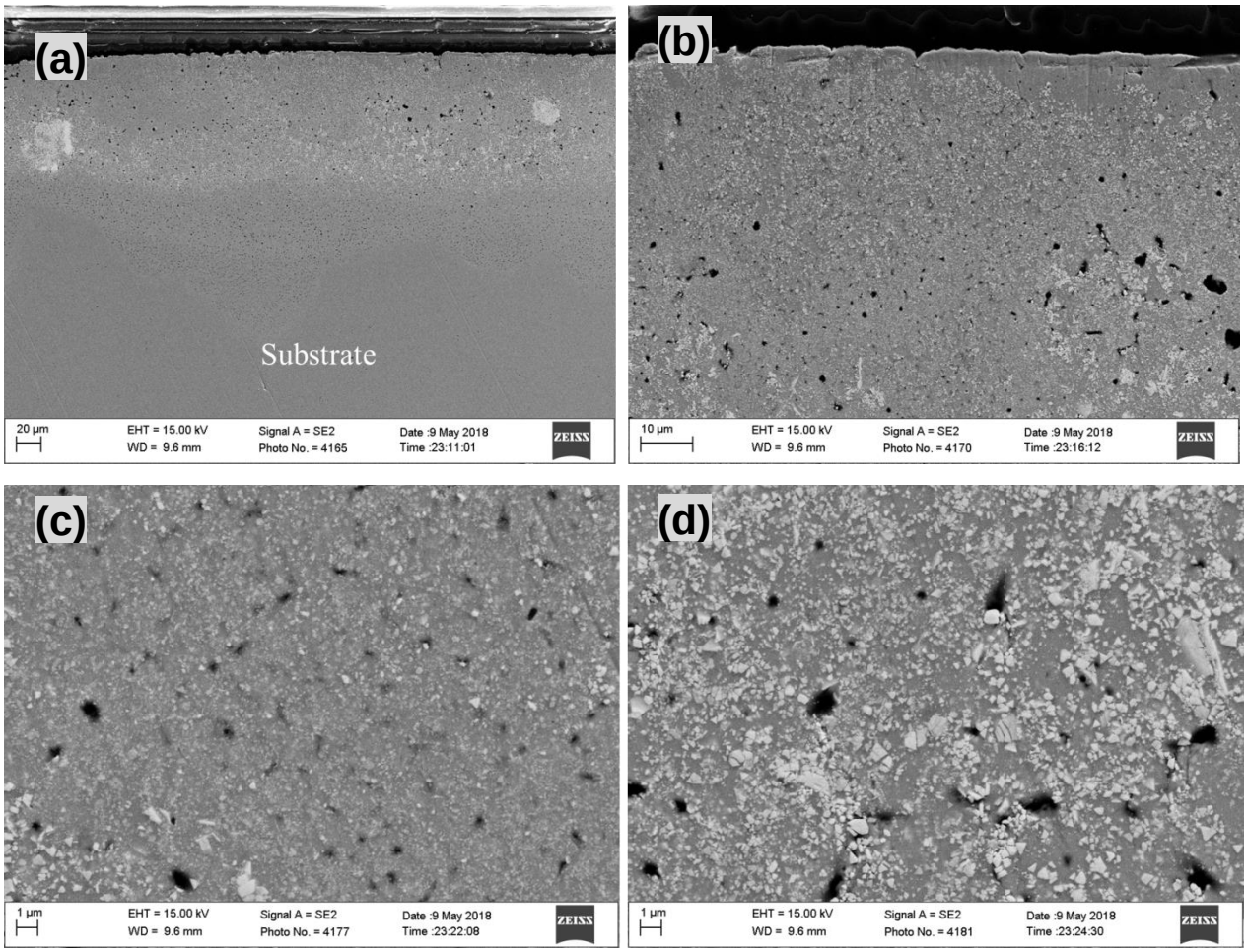

Figure 6-4: Laser deposited Cu-WC (x=0.1) nanocomposite sample on a pure nickel substrate.

It is expected that a higher fraction of nanoparticles can decrease the laser beam reflectivity during LAM and thus further improve the uniformity and densification of the laser deposited copper sample. Therefore, we incorporated a higher loading of nanoparticles into pure copper (about 20vol.%) to laser additively manufacture Cu-WC (x=0.25) nanocomposite sample (See method at section 6.1.1). Figure 6-5a reveals the Cu-WC (x=0.25) nanocomposite sample (3mm × 3mm) with a thickness approximately of 269.8 ± 6.2 μm was layer-by-layer deposited on a pure nickel substrate by laser melting of the nanocomposite powders. A magnified SEM image (Fig. 6-5b) was captured to show the good layer uniformity of the nanocomposite. To reveal the internal structure, a cross sectional images of the sample were obtained, as shown in the Fig. 6-5c and Fig. 6-5d. Similar to the case of the laser deposited Cu-WC (x=0.1), nanoparticles were distributed throughout the Cu-WC (x=0.25). Clusters are still observed possibly due to the same reasons, i.e., powder uniformity and nanoparticle distribution in the Cu matrix. In addition, microstructure analysis reveals a substantial difference of densification between laser deposited Cu-WC components additively manufactured from the nanocomposite powders with x=0.1 and x=0.25.

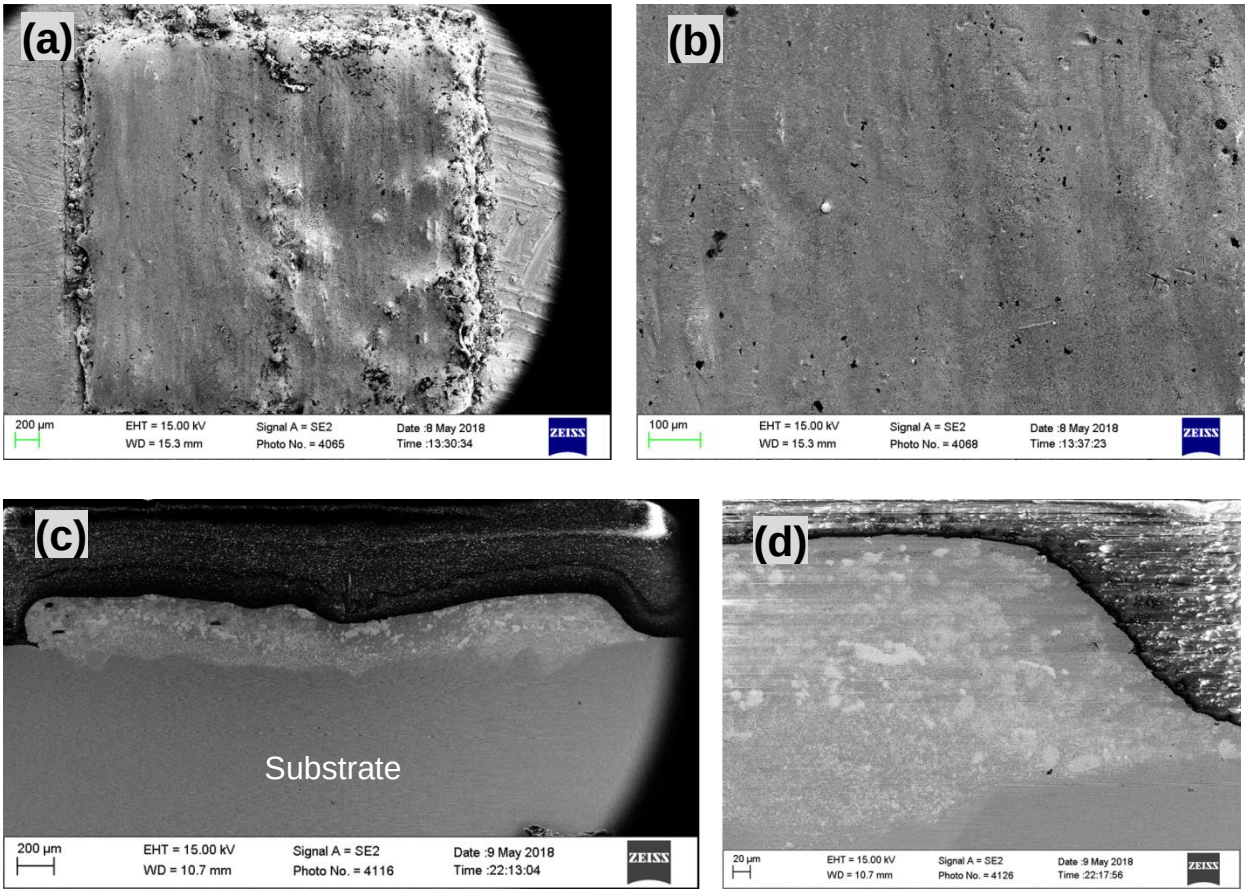

Figure 6-5: Laser deposited Cu-WC (x=0.25) nanocomposite sample on a pure nickel substrate.

The porosities observed from the internal structure, as shown in Fig. 6-6c and Fig. 6-6d, are significantly improved when compared to those of laser deposited Cu-WC with x=0.1, indicating that the higher fraction of nanoparticles indeed enhanced the laser beam absorption and further improve the densification of the sample.

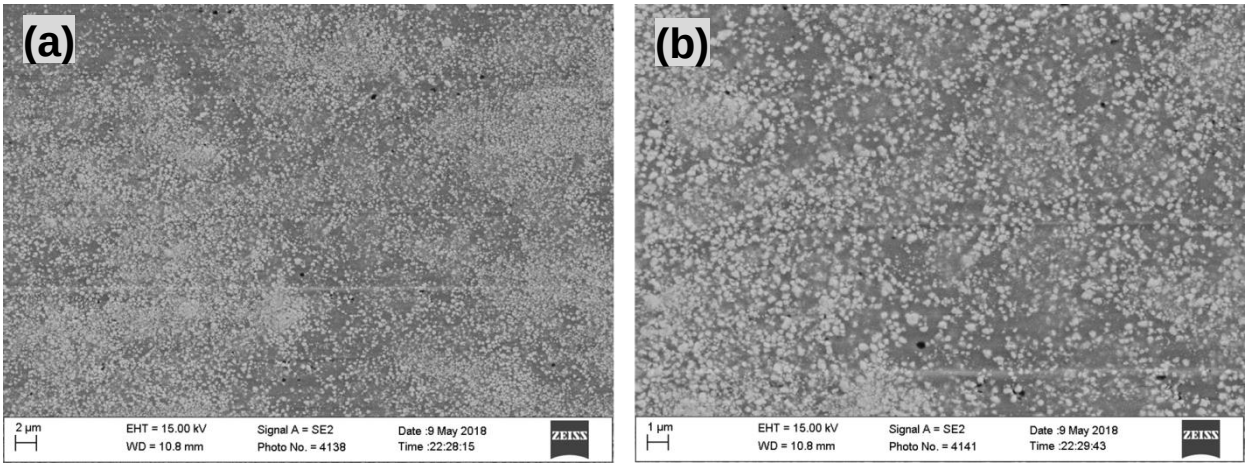

Figure 6-6: Internal microstructure of laser deposited Cu-WC (x=0.25) nanocomposite

To study the effects of high nanoparticle volume fraction, i.e., about 40 vol.%, on LAM, the dry mechanical mixing nanocomposite powders with a higher loading of reinforced nanoparticles, i.e., Cu-WC (x=0.66), were used for LAM experiment. The cross-sectional SEM micrographs of the laser deposited Cu-WC (x=0.66) are shown in Figure 6-7. Different from the results of components additively manufactured using wet mechanical mixing powders, the samples laser deposited using dry mechanical mixing powders have even more clusters (yellow arrow) located at the regions far from the nickel substrate, as shown in Fig. 6-7a. The absence of the clusters might attribute to the lower laser reflectivity of the wet mechanical mixing powder. As such, the laser energy was mainly absorbed by WC nanoparticles inside the Cu matrix powder, causing agglomerations of WC nanoparticle.

In contrast, the region closed to the nickel substrate reveals a uniform dispersion and distribution of nanoparticles. The gray spots observed in Fig. 6-7b show WC nanoparticles (in white) were uniformly dispersed and distributed in the dark dense copper layer. It is believed the pure nickel substrate with a good wettability and a low thermal conductivity also received the laser energy and contributed the heat to the powder melting. However, as the component was additively deposited further, the less heat contribution received from the nickel substrate. Thereby only WC

nanoparticles in the nanocomposite powders received the laser energy, which further caused the formation of clusters.

To reveal the nanoparticle effects on grain structure, we utilized FIB to selectively ion milled a pocket at the area with dense dispersed nanoparticles, as shown in Figure 6-7c. The grain size of the fully dense supper copper is approximately less than 5 μm (Fig. 6-7d), which indicates the uniform dispersed nanoparticles (black spots in this case) restrict the grain growth.

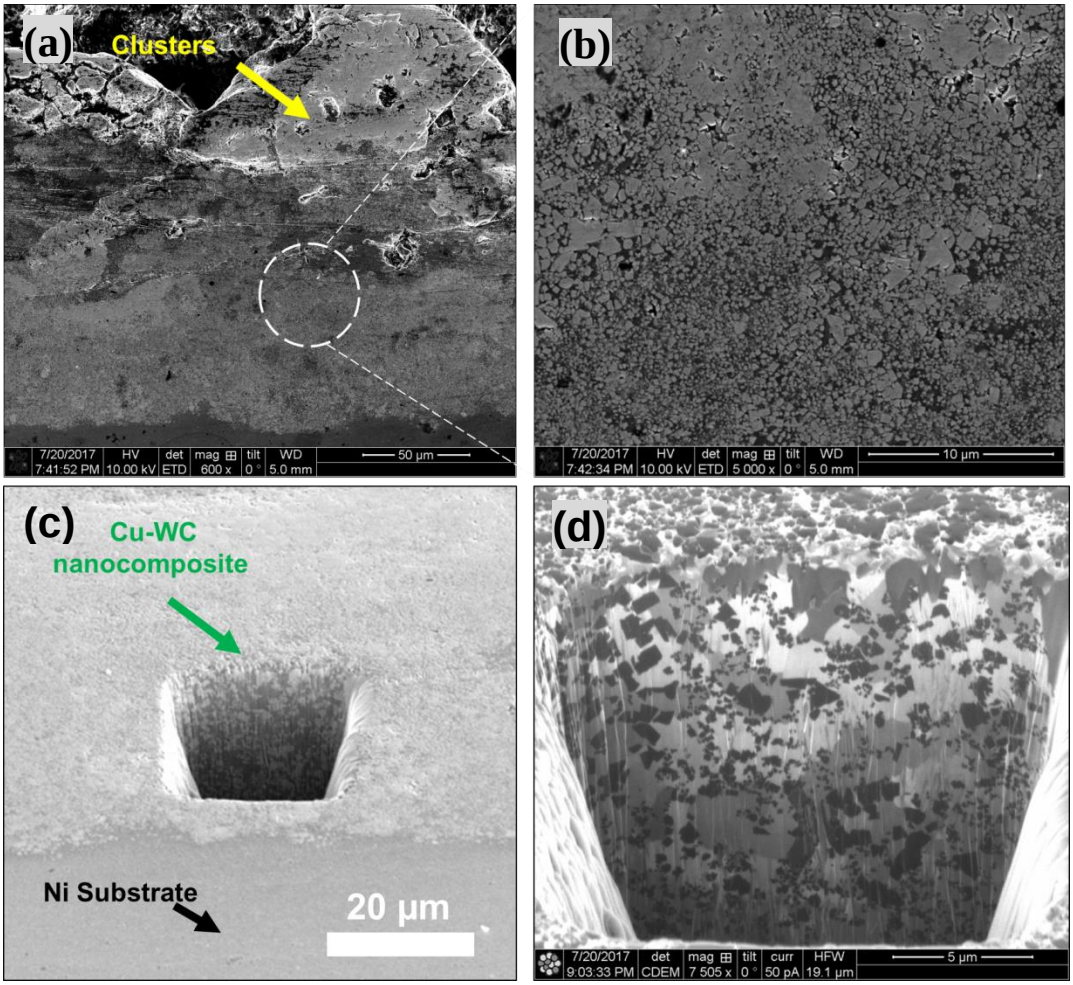

Figure 6-7: Microstructure of laser deposited Cu-WC (x=0.66). The cross sectional SEM image of the nanocomposite **a,b** without and **c**, with tilted angle of 52° under SEM; **d,** The grain structure of the laser deposited sample

6.2.1.4 Grain sizes of laser deposited sample

FIB imaging was utilized to reveal the grain structure of the as-cast MMNC substrate and laser deposited sample. The channeling contrast from different orientated grains and the dispersion of WC nanoparticles were characterized using CDEM mode of ion beam (See section of 6.1.2). FIB micrograph of laser additively manufactured Cu-12vol.%WC. The darkest phase in Figure 6-8a is WC nanoparticles whereas the other white or grayish phases are copper grains with different orientations. A closed examination (Fig. 6-8b) reveals a refined grain structure by dispersed WC nanoparticles (black spots). Whereas the average grain size for the MMNC substrate (Cu-11vol.%WC) is approximately 310 ± 101 nm, the average grain size for the laser additively manufactured Cu-12vol.%WC is refined to 199 ± 75 nm. This slight reduction of grain size could be explained by the rapid cooling rate induced by laser. The results were summarized in Fig. 6-8c. It is of both scientific and technical interest to use EBSD to study the nanoparticle effects on grain structures.

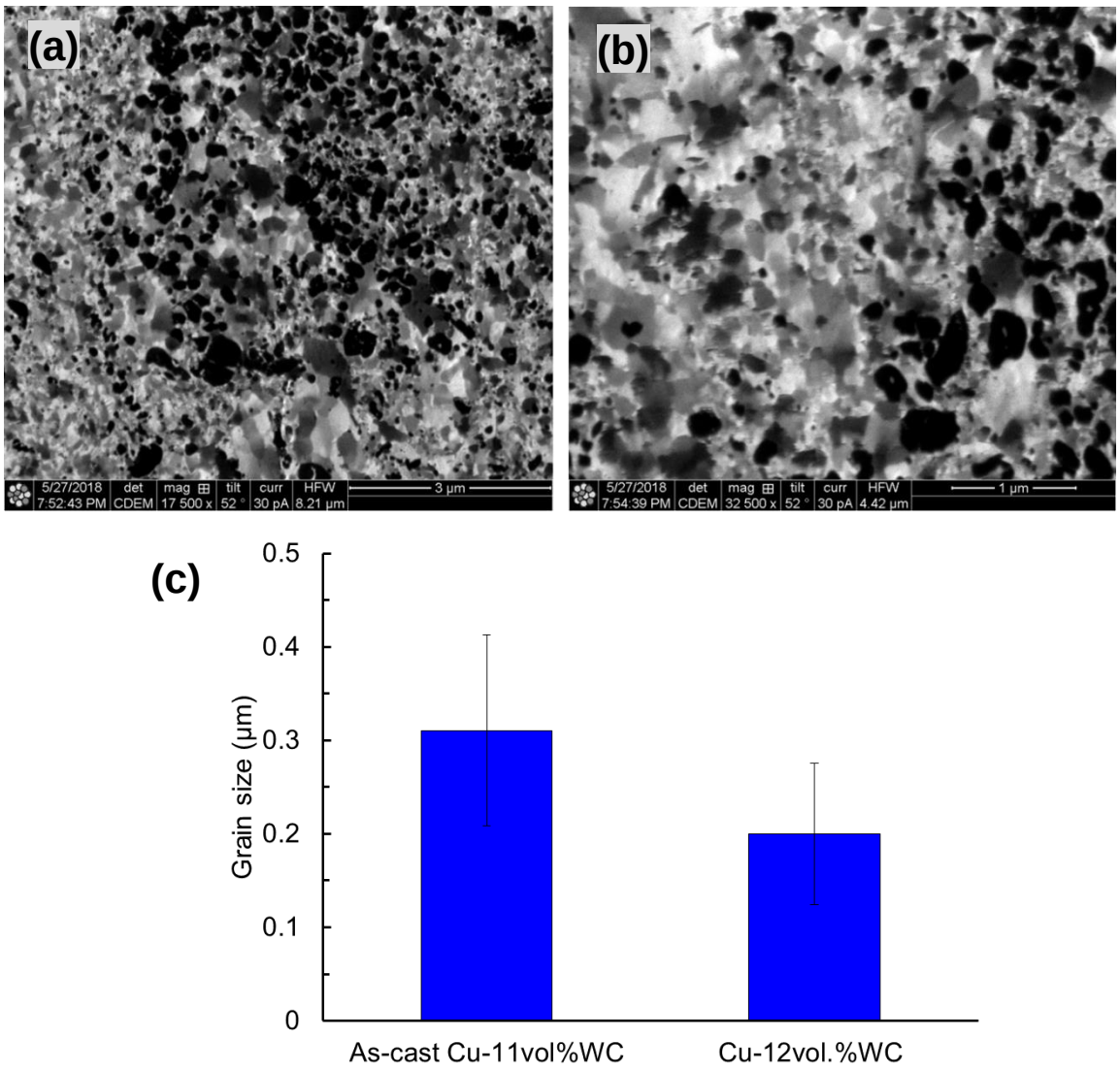

Figure 6-8: **a, b,** Grain structure of laser deposited Cu-12vol.%WC nanocomposite**. c,** comparison of grain sizes between samples of as cast MMNC substrate and laser deposited Cu-12vol.%WC.

6.2.2 Mechanical properties

6.2.2.1 Microhardness

The hardness of the laser deposited Cu-12vol.%WC and as-cast MMNC were summarized in Fig. 6-9. The average hardness of the laser deposited Cu-12vol.%WC on MMNC substrate is about 121.8 ± 11.4 HV whereas the sample deposited on the pure copper substrate has an average hardness of 120.8 ± 17.1 HV. Both have similar results because of the same volume fraction of incorporated nanoparticles. The as-cast MMNC used in this study has an average hardness of 147.7 ± 19.1 HV, which is higher than that of the laser deposited sample because of the better nanoparticle dispersion and distribution.

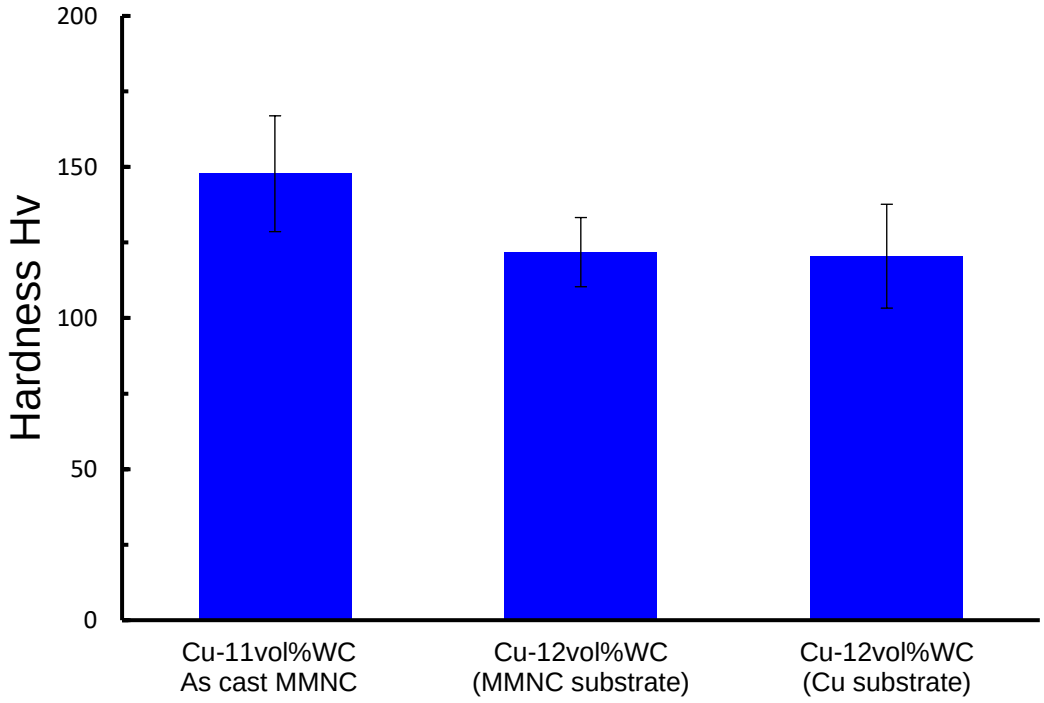

Figure 6-9: Comparison of microhardenss between samples of as cast MMNC substrate and laser deposited Cu-12vol.%WC.

6.2.2.2 Young's modulus

The results from Young's modulus measurement, as shown in Fig. 6-10, illustrate that the laser deposited Cu-12vol.%WC on MMNC substrate and Cu substrate have a young's modulus of 132.7 ± 15.1 GPa and 131.9 ± 12.3 GPa, respectively. A young's modulus of 149.1 ± 16.7 GPa obtained from the as-cast MMNC sample shows a higher result than that of laser deposited sample. It is very likely that the porosities and clusters in the laser deposited sample lead to a slightly lower young's modulus. The properties can be improved by optimizing the process parameters such as laser energy density and powder sample morphology.

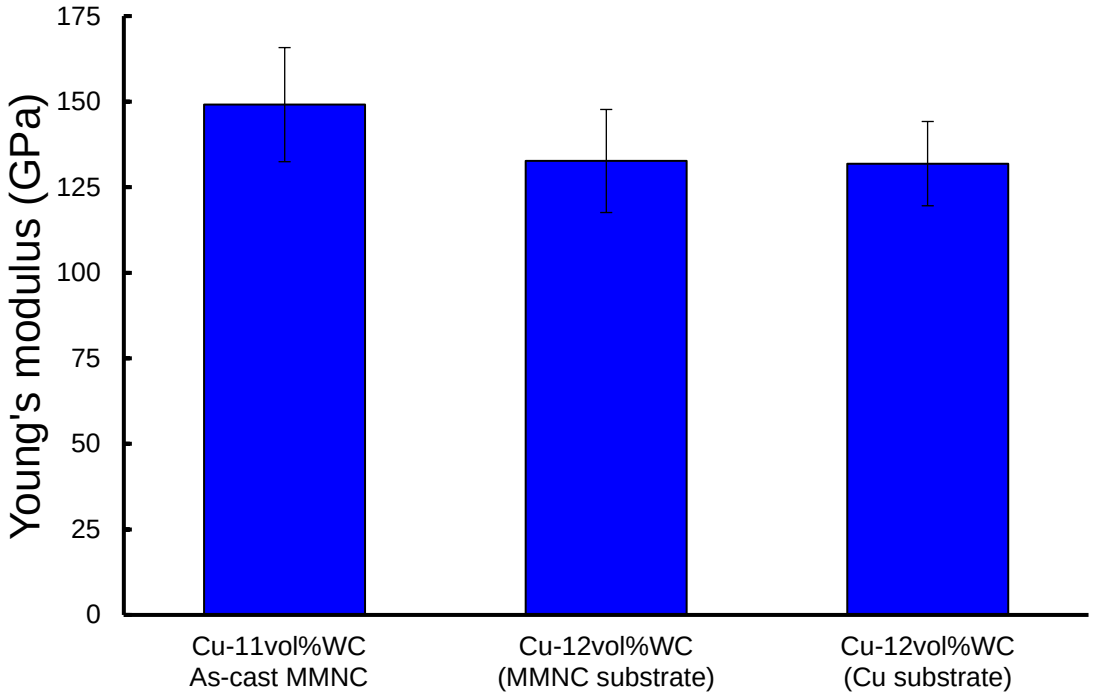

Figure 6-10: Comparison of Young's modulus between samples of as cast MMNC substrate and laser deposited Cu-12vol.%WC.

In addition to the Young's modulus measurement of laser deposited Cu-12vol.%WC, the Young's modulus of laser deposited sample on a nickel substrate were also measured, as shown in Fig. 6-11, for fundamental study. The Young's modulus increased as the nanoparticle volume

fraction increased. While the current purpose of using pure nickel as a substrate is to improve the layer uniformity, it is of interest for a future study on various application of copper-nickel nanocomposite.

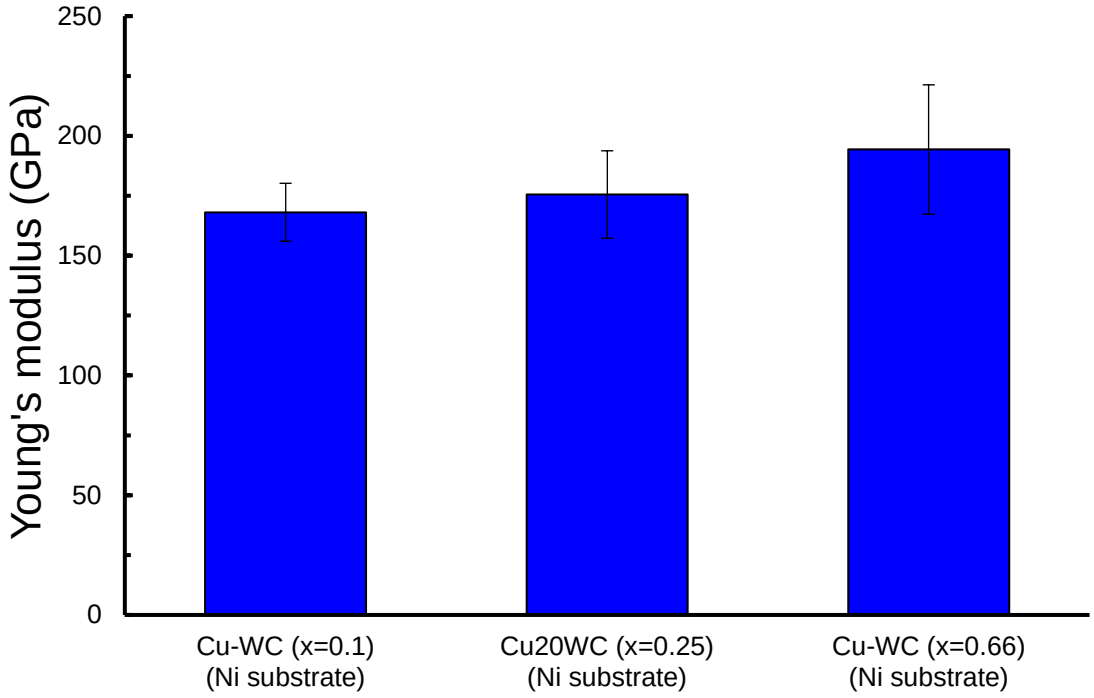

Figure 6-11: Comparison of Young's modulus between samples of laser deposited Cu-WC sample on nickel substrate

6.3 Summary

This chapter explores the feasibility of producing copper metal matrix nanocomposites by laser additive manufacturing. Incorporation of WC nanoparticles into Cu powders enables a higher laser absorption and thus improves the surface morphology, layer uniformity, and densification of the components. Pure copper was initially used as a substrate for LAM experiment but the resultant component consists of number porosities (about 200μm) with a ball-liked morphologies. Substrates of pure nickel and as-cast MMNC were further used to improve the layer uniformity. Accordingly, microstructure analysis reveals that the samples have a better surface morphology,

densification and layer uniformity than the sample deposited on pure copper. Good nanoparticle distribution in the matrix has been observed but clusters still existes, which could be attributed to the morphology and laser reflectivity of the nanocomposite powders. In addition, the microstructure study shows that the nanoparticles inhibited the grain growth and refined the Cu matrix. Laser induced rapid cooling results in a smaller grain size in the laser deposited sample than that of the as-cast sample. The as-cast sample exhibits slightly higher Young's modulus and hardness than the laser deposited sample, mainly due to the better sample densification. The results suggest a processing route to directly laser additively manufactured dense Cu matrix nanocomposites is feasible.

CHAPTER 7 CONCLUSIONS

This study is to understand nanoparticle effects on laser additive manufacturing of high-performance metal matrix nanocomposites (MMNCs). The specific objective of this research is to experimentally investigate the nanoparticle effects on laser reflectivity of powders, micro/nanostructure and mechanical properties of laser additively manufactured components.

Two processing routes, i.e., nanoparticle self-assembly with assistance of mechanical mixing or ultrasonic processing, were used to prepare metal matrix nanocomposite (MMNC) powders in this study. MMNC powders with different volume ratios (x) between nanoparticle (TiC or WC) and matrix powders (Al, AlSi12, or Cu) were prepared, including AMNC (x=0.25; x=1), AlSi12-TiC (x=0.05 and x=0.25), and Cu-WC (x=0.1, x=0.25 and x=0.66). The resulting MMNC powders by ultrasonic processing show a significant reduction in laser reflectivity at the wavelength of 1070 nm as the nanoparticle fractions increase. Moreover, AMNC powders with spherical shapes and uniform size distribution were obtained using the ultrasonic processing method. Nanoparticles were self-assembled at the surface of the matrix due to the favorable energy state. Uniform distribution and good dispersion of nanoparticles throughout the matrix powder have been observed using FIB and SEM. Additionally, to demonstrate the scalability, MMNC powder were produced by two methods, i.e., wet mechanical mixing or dry mechanical mixing method. The wet mechanical mixing powders show the reflectivity of the powders decreases as the nanoparticle fractions increases, whereas the reflectivity of dry mechanical mixing powder shows little reduction due to the less nanoparticle coverage at the matrix of copper. The powder morphology and size distribution of the powders (Al system) by wet mechanical mixing show comparable results to those of the powders by ultrasonic processing, demonstrating the potential scalability of the technique. For the copper matrix system, more efforts are still needed to improve

the powder morphology, size distribution, and nanoparticle dispersion and distribution inside the matrix. This study offers a low cost and scalable method for mass production of MMNC powders with various loadings of nanoparticle for LAM.

Laser additive manufacturing of two types of AMNC powders were conducted by self-customized laser additive manufacturing system. Laser deposited AMNCs with different volume fractions of nanoparticles were successfully produced. The AMNCs offer higher Young's modulus, yield strength, and hardness as the nanoparticle fractions become higher. The AMNC with 35 vol.% TiC delivers a yield strength of up to 1.0 GPa, plasticity over 10 %, and Young's modulus of approximately 200 GPa. The AMNC (35 vol.% TiC) offers unprecedented performance in terms of specific yield strength, specific Young's modulus, and elevated temperature stability at 400 ºC amongst all aluminum alloys, which are attributed to high density of well-dispersed nanoparticles, strong interfacial bonding, and ultrafine grain sizes (about 331 nm). In addition, to compare the material performance obtained from laser melting two types of AMNCs powders, laser deposited AMNC (15 vol.%TiC) sample with a thickness of 513 ± 36 μm was laser additively produced via melting of AMNCs powders by mechanical mixing, delivering mechanical properties comparable to those of laser deposited AMNC (17 vol.% TiC) via powders by ultrasonic processing. The study provides a new pathway for laser 3D Printing of nanoparticles reinforced aluminum for widespread applications.

To achieve comparable mechanical properties of AMNCs with less nanoparticles, AlSi12 alloy was selected as a matrix material for LAM. Samples with and without TiC nanoparticles were successfully laser deposited to study the fundamental nanoparticle interaction with alloy phase and also to compare the mechanical properties of AMNCs. Micro/nanostructure analysis reveals that the grain size of AlSi12-TiC nanocomposites decreases as the fraction of incorporated

nanoparticles increases. Additionally, some reaction products, i.e., SiC and Al_3Ti, have been identified from the laser deposited AlSi12 nanocomposite samples, suggesting a chemical reaction occurred during the laser processing. The microhardness of laser deposited AlSi12-TiC with x=0.25 shows a significant increase (578 ± 42.5 HV) when compared to that of sample without nanoparticles, which could be attributed to the dispersed TiC nanoparticles and contribution of reaction products, i.e., SiC nanoparticles and rich amount of Al_3Ti intermetallic phase. Moreover, the laser deposited AlSi12 samples with TiC nanoparticles offer a comparable Young's modulus to that of AMNC samples. While the mechanical properties of AlSi12-TiC sample are comparable to that of AMNCs, more fundamental studies and careful processing parameters are needed to optimize the LAM of aluminum alloy system. This study offers a novel design route to additively manufactured high-performance aluminum alloys by benefiting from the strengthening effects of the minor phase(s) in an alloy to use a less amount of incorporated nanoparticles.

The feasibility of LAM of Cu matrix nanocomposite was explored by laser melting of Cu-WC nanocomposite powders. The microstructure shows that a large number of porosities with ball-liked morphologies were obtained after laser melting of the powders on a pure copper substrate. However, the layer uniformities and densification behaviors of the laser deposited parts have been significantly improved using substrates of pure nickel or as-cast MMNC, mainly due to a lower thermal conductivity and good wettability. The internal microstructure analysis reveals a good nanoparticle distribution in the matrix but some agglomeration of nanoparticles still existed, which can be attributed to the morphology and laser reflectivity of the nanocomposite powders. The grain structure of laser deposited Cu-12vol.%WC has been refined by the nanoparticles and laser induced rapid solidification. The study provides a feasible processing route to directly laser deposit dense Cu samples by addition of nanoparticles.

In summary, the work presented in this dissertation has experimentally demonstrated a wide varieties of laser deposited MMNCs to provide insights of powder fabrication (nanoparticle selection, volume fractions, reflectivity, size and morphology, and scalability) and processing/microstructure/properties relationships. This study advances the knowledge base for a rational design of high-performance metal matrix nanocomposites with desirable properties by LAM for numerous applications.

CHAPTER 8 RECOMMENDATION FOR FUTURE WORK

8.1 Fabrication of metal matrix nanocomposite (MMNC) powders

The MMNC powders presented in this study were fabricated via a self-assembly method assisted by ultrasonic processing or mechanical mixing. However, the mass of powders produced in this study is still only about 50g to 70g. It would be of significance if the amount of produced powders can be increased. More engineering optimizations are necessary to extend the techniques to industrial manufacturing. For example, powder size, dispersion and distribution of nanoparticles, stirring speed, volume ratio between matrix powder and salt, and volume ratio between nanoparticle and matrix powder are needed to be considered. To realize the scalable possibility, this study suggests the processing routes can be focused on increasing the size of crucible, optimizing stirring speed and enhancing the amount of volume ratio between matrix powder and salt. If successful, it would allow these techniques incorporate any amount of nanoparticles into any matrix powder to produce MMNCs with any nanoparticle volume fractions.

8.2 Laser additive manufacturing of MMNCs

The MMNCs laser additively manufactured in this study were carried out using customized LAM system. It would be necessary to further clarify all the results using commercial LAM machines to demonstrate the material performance. For example, it will be a significant breakthrough if tensile tests based on ASTM standards can be obtained from the laser additive manufactured MMNC parts. The ductility and strength of the parts can be tested for various engineering applications.

8.3 Further fundamental study on LAM of MMNCs

This study experimentally demonstrated a variety of laser deposited MMNCs. It is also important to fundamentally investigate the effects of nanoparticles on LAM. For example, powder

flowability, laser reflectivity, and thermophysical properties such as thermal conductivity, surface tension and viscosity. The knowledge will be extremely important for precise control of the nanoparticles effects on the LAM process. Experimentations with various nanoparticles in different matrixes can be carried out using a standard LAM machine, followed by in depth microstructure and standard characterizations. The knowledge obtained from the experimental results can be compared with fundamental studies to validate and improve the fundamental models. The relationships among processing parameters, microstructure evolution, and material performance can be scientifically established.

REFERENCE

1 Kruth, J. P., Leu, M. C. & Nakagawa, T. Progress in Additive Manufacturing and Rapid Prototyping. *CIRP Annals* **47**, 525-540 (1998).

2 Gibson, I., Rosen, D. W. & Stucker, B. *Additive Manufacturing Technologies*. (Springer, 2010).

3 Steen, W. M. & Mazumder, J. *Laser material processing*. (Springer Science & Business Media, 2010).

4 Gu, D. D., Meiners, W., Wissenbach, K. & Poprawe, R. Laser additive manufacturing of metallic components: materials, processes and mechanisms. *International Materials Reviews* **57**, 133-164 (2012).

5 Aboulkhair, N. T., Everitt, N. M., Maskery, I., Ashcroft, I. & Tuck, C. Selective laser melting of aluminum alloys. *MRS Bulletin* **42**, 311-319 (2017).

6 I., M. A., Jocelyn, D. & Jacqueline, L. B. Fusion-Based Additive Manufacturing for Processing Aluminum Alloys: State-of-the-Art and Challenges. *Advanced Engineering Materials* **19**, 1700003 (2017).

7 Wang, Y. M. *et al.* Additively manufactured hierarchical stainless steels with high strength and ductility. *Nature Materials* **17**, 63 (2017).

8 Lai-Chang, Z. & Hooyar, A. Selective Laser Melting of Titanium Alloys and Titanium Matrix Composites for Biomedical Applications: A Review *Advanced Engineering Materials* **18**, 463-475 (2016).

9 Jia, Q. & Gu, D. Selective laser melting additive manufacturing of Inconel 718 superalloy parts: Densification, microstructure and properties. *Journal of Alloys and Compounds* **585**, 713-721 (2014).

10 Becker, D. & Wissenbach, K. in *Proceeding conference* 195-199 (2009).

11 Louvis, E., Fox, P. & Sutcliffe, C. J. Selective laser melting of aluminium components. *Journal of Materials Processing Technology* **211**, 275-284 (2011).

12 Steen, W. Laser material processing—an overview. *Journal of Optics A: Pure and Applied Optics* **5**, S3 (2003).

13 Sames, W. J., List, F. A., Pannala, S., Dehoff, R. R. & Babu, S. S. The metallurgy and processing science of metal additive manufacturing. *International Materials Reviews* **61**, 315-360 (2016).

14 Montero Sistiaga, M. L. *et al.* Changing the alloy composition of Al7075 for better processability by selective laser melting. *Journal of Materials Processing Technology* **238**, 437-445 (2016).

15 Kaufmann, N. *et al.* Influence of Process Parameters on the Quality of Aluminium Alloy EN AW 7075 Using Selective Laser Melting (SLM). *Physics Procedia* **83**, 918-926 (2016).

16 Rawal, S. P. Metal-matrix composites for space applications. *Jom* **53**, 14-17 (2001).

17 Crainic, N. & Marques, A. T. Nanocomposites: a State-of-the-Art Review. *Key Engineering Materials* **230-232**, 656-650 (2002).

18 Chang, S.-Y., Chen, C.-F., Lin, S.-J. & Kattamis, T. Z. Electrical resistivity of metal matrix composites. *Acta Materialia* **51**, 6291-6302 (2003).

19 Chen, L.-Y. *et al.* Processing and properties of magnesium containing a dense uniform dispersion of nanoparticles. *Nature* **528**, 539-543 (2015).

20 Cao, C., Chen, L., Xu, J., Choi, H. & Li, X. Strengthening Al–Bi–TiC0.7N0.3 nanocomposites by Cu addition and grain refinement. *Materials Science and Engineering: A* **651**, 332-335 (2016).

21 Ma, C., Zhao, J., Cao, C., Lin, T.-C. & Li, X. Fundamental Study on Laser Interactions With Nanoparticles-Reinforced Metals—Part I: Effect of Nanoparticles on Optical Reflectivity, Specific Heat, and Thermal Conductivity. *Journal of Manufacturing Science and Engineering* **138**, 121001 (2016).

22 Ma, C., Zhao, J., Cao, C., Lin, T.-C. & Li, X. Fundamental Study on Laser Interactions With Nanoparticles-Reinforced Metals—Part II: Effect of Nanoparticles on Surface Tension, Viscosity, and Laser Melting. *Journal of Manufacturing Science and Engineering* **138**, 121002-121002-121006 (2016).

23 Borkar, T. & Harimkar, S. P. Effect of electrodeposition conditions and reinforcement content on microstructure and tribological properties of nickel composite coatings. *Surface and Coatings Technology* **205**, 4124-4134 (2011).

24 Chen, L., Wang, L., Zeng, Z. & Zhang, J. Effect of surfactant on the electrodeposition and wear resistance of Ni–Al2O3 composite coatings. *Materials Science and Engineering: A* **434**, 319-325 (2006).

25 García-Lecina, E., García-Urrutia, I., Díez, J. A., Morgiel, J. & Indyka, P. A comparative study of the effect of mechanical and ultrasound agitation on the properties of electrodeposited Ni/Al2O3 nanocomposite coatings. *Surface and Coatings Technology* **206**, 2998-3005 (2012).

26 Yang, Y., Lan, J. & Li, X. Study on bulk aluminum matrix nano-composite fabricated by ultrasonic dispersion of nano-sized SiC particles in molten aluminum alloy. *Materials Science and Engineering: A* **380**, 378-383 (2004).

27 Cao, G., Konishi, H. & Li, X. Mechanical properties and microstructure of Mg／SiC nanocomposites fabricated by ultrasonic cavitation based nanomanufacturing. *Journal of Manufacturing Science and Engineering* **130**, 031105 (2008).

28 Gu, D. & Shen, Y. Effects of processing parameters on consolidation and microstructure of W–Cu components by DMLS. *Journal of Alloys and Compounds* **473**, 107-115 (2009).

29 Gu, D., Wang, Z., Shen, Y., Li, Q. & Li, Y. In-situ TiC particle reinforced Ti–Al matrix composites: powder preparation by mechanical alloying and selective laser melting behavior. *Applied Surface Science* **255**, 9230-9240 (2009).

30 Chu, K. *et al.* Fabrication and effective thermal conductivity of multi-walled carbon nanotubes reinforced Cu matrix composites for heat sink applications. *Composites Science and Technology* **70**, 298-304 (2010).

31 Gu, D., Hagedorn, Y.-C., Meiners, W., Wissenbach, K. & Poprawe, R. Nanocrystalline TiC reinforced Ti matrix bulk-form nanocomposites by Selective Laser Melting (SLM): Densification, growth mechanism and wear behavior. *Composites Science and Technology* **71**, 1612-1620 (2011).

32 Gu, D., Meng, G., Li, C., Meiners, W. & Poprawe, R. Selective laser melting of TiC/Ti bulk nanocomposites: Influence of nanoscale reinforcement. *Scripta Materialia* **67**, 185-188 (2012).

33 Gu, D., Wang, H. & Zhang, G. Selective Laser Melting Additive Manufacturing of Ti-Based Nanocomposites: The Role of Nanopowder. *Metallurgical and Materials Transactions A* **45**, 464-476 (2014).

34 Gu, D. *et al.* Rapid fabrication of Al-based bulk-form nanocomposites with novel reinforcement and enhanced performance by selective laser melting. *Scripta Materialia* **96**, 25-28 (2015).

35 Pengpeng, Y. & Dongdong, G. Molten pool behaviour and its physical mechanism during selective laser melting of TiC/AlSi10Mg nanocomposites: simulation and experiments. *Journal of Physics D: Applied Physics* **48**, 035303 (2015).

36 Biedunkiewicz, A., Biedunkiewicz, W., Figiel, P. & Grzesiak, D. Preparation of stainless steel-TiC composite by selective laser melting. *Chem. Listy* **105**, 773-774 (2011).

37 Figiel, P., Biedunkiewicz, W. & Grzesiak, D. Oxidation process of the steel/nc-TiC nanocomposites. *Journal of thermal analysis and calorimetry* **108**, 979-983 (2012).

38 Biedunkiewicz, A. *et al.* Effect of milling time on thermal treatment of TiC, TiB 2/steel powders. *Journal of Thermal Analysis and Calorimetry* **113**, 379-383 (2013).

39 Dadbakhsh, S. & Hao, L. Effect of Al alloys on selective laser melting behaviour and microstructure of in situ formed particle reinforced composites. *Journal of alloys and compounds* **541**, 328-334 (2012).

40 Song, B. *et al.* Microstructure and tensile behavior of hybrid nano-micro SiC reinforced iron matrix composites produced by selective laser melting. *Journal of Alloys and Compounds* **579**, 415-421 (2013).

41 Frazier, W. E. Metal additive manufacturing: a review. *Journal of Materials Engineering and Performance* **23**, 1917-1928 (2014).

42 Olakanmi, E. O., Cochrane, R. F. & Dalgarno, K. W. A review on selective laser sintering/melting (SLS/SLM) of aluminium alloy powders: Processing, microstructure, and properties. *Progress in Materials Science* **74**, 401-477 (2015).

43 Wang, X., Zhang, L., Fang, M. & Sercombe, T. B. The effect of atmosphere on the structure and properties of a selective laser melted Al–12Si alloy. *Materials Science and Engineering: A* **597**, 370-375 (2014).

44 Campbell, J. *Castings*. (Elsevier, 2003).

45 Buchbinder, D., Meiners, W., Wissenbach, K. & Poprawe, R. Selective laser melting of aluminum die-cast alloy—Correlations between process parameters, solidification conditions, and resulting mechanical properties. *Journal of Laser Applications* **27**, S29205 (2015).

46 Read, N., Wang, W., Essa, K. & Attallah, M. M. Selective laser melting of AlSi10Mg alloy: Process optimisation and mechanical properties development. *Materials & Design (1980-2015)* **65**, 417-424 (2015).

47 Brandl, E., Heckenberger, U., Holzinger, V. & Buchbinder, D. Additive manufactured AlSi10Mg samples using Selective Laser Melting (SLM): Microstructure, high cycle fatigue, and fracture behavior. *Materials & Design* **34**, 159-169 (2012).

48 Gu, D. D. & Shen, Y. F. Development and characterisation of direct laser sintering multicomponent Cu based metal powder. *Powder Metallurgy* **49**, 258-264 (2006).

49 Tang, Y. *et al.* Direct laser sintering of a copper-based alloy for creating three-dimensional metal parts. *Journal of Materials Processing Technology* **140**, 368-372 (2003).

50 Zhu, H. H., Lu, L. & Fuh, J. Y. H. Development and characterisation of direct laser sintering Cu-based metal powder. *Journal of Materials Processing Technology* **140**, 314-317 (2003).

51 Zhu, H. H., Lu, L. & Fuh, J. Y. H. Influence of binder's liquid volume fraction on direct laser sintering of metallic powder. *Materials Science and Engineering: A* **371**, 170-177 (2004).

52 Pogson, S., Fox, P., O'Neill, W. & Sutcliffe, C. J. The direct metal laser remelting of copper and tool steel powders. *Materials Science and Engineering: A* **386**, 453-459 (2004).

53 Gu, D. & Shen, Y. Influence of reinforcement weight fraction on microstructure and properties of submicron WC–Cop/Cu bulk MMCs prepared by direct laser sintering. *Journal of Alloys and Compounds* **431**, 112-120 (2007).

54 Gu, D. & Shen, Y. Influence of Cu-liquid content on densification and microstructure of direct laser sintered submicron W–Cu/micron Cu powder mixture. *Materials Science and Engineering: A* **489**, 169-177 (2008).

55 Wu, W., Yang, Y. & Huang, Y. Direct manufacturing of Cu-based alloy parts by selective laser melting. *Chin. Opt. Lett.* **5**, 37-40 (2007).

56 Bhattacharya, S. *et al.* Microstructural evolution and mechanical, and corrosion property evaluation of Cu–30Ni alloy formed by Direct Metal Deposition process. *Journal of Alloys and Compounds* **509**, 6364-6373 (2011).

57 Liu, Z. H., Zhang, D. Q., Sing, S. L., Chua, C. K. & Loh, L. E. Interfacial characterization of SLM parts in multi-material processing: Metallurgical diffusion between 316L stainless steel and C18400 copper alloy. *Materials Characterization* **94**, 116-125 (2014).

58 Scudino, S. *et al.* Additive manufacturing of Cu–10Sn bronze. *Materials Letters* **156**, 202-204 (2015).

59 Popovich, A. *et al.* Microstructure and mechanical properties of additive manufactured copper alloy. *Materials Letters* **179**, 38-41 (2016).

60 Song, C., Yang, Y., Liu, Y., Luo, Z. & Yu, J.-K. Study on manufacturing of W-Cu alloy thin wall parts by selective laser melting. *The International Journal of Advanced Manufacturing Technology* **78**, 885-893 (2015).

61 Kaden, L. *et al.* Selective laser melting of copper using ultrashort laser pulses. *Applied Physics A* **123**, 596 (2017).

62 Leuders, S. *et al.* On the mechanical behaviour of titanium alloy TiAl6V4 manufactured by selective laser melting: Fatigue resistance and crack growth performance. *International Journal of Fatigue* **48**, 300-307 (2013).

63 Attar, H. *et al.* Comparison of wear properties of commercially pure titanium prepared by selective laser melting and casting processes. *Materials Letters* **142**, 38-41 (2015).

64 Thijs, L., Verhaeghe, F., Craeghs, T., Humbeeck, J. V. & Kruth, J.-P. A study of the microstructural evolution during selective laser melting of Ti–6Al–4V. *Acta Materialia* **58**, 3303-3312 (2010).

65 Marcu, T., Todea, M., Gligor, I., Berce, P. & Popa, C. Effect of surface conditioning on the flowability of Ti6Al7Nb powder for selective laser melting applications. *Applied Surface Science* **258**, 3276-3282 (2012).

66 Zhang, M. Y. *et al.* Laser Engineered Multilayer Coating of Biphasic Calcium Phosphate/Titanium Nanocomposite on Metal Substrates. *ACS Applied Materials & Interfaces* **3**, 339-350 (2011).

67 Campoli, G. *et al.* Mechanical properties of open-cell metallic biomaterials manufactured using additive manufacturing. *Materials & Design* **49**, 957-965 (2013).

68 Thomas, I. Mechanical properties of open‐pore titanium foam. *Journal of Biomedical Materials Research Part A* **81A**, 964-970 (2007).

69 Li, J. P. *et al.* Bone ingrowth in porous titanium implants produced by 3D fiber deposition. *Biomaterials* **28**, 2810-2820 (2007).

70 Zhang, L. C. & Attar, H. Selective laser melting of titanium alloys and titanium matrix composites for biomedical applications: a review. *Advanced Engineering Materials* **18**, 463-475 (2016).

71 Yadroitsev, I., Krakhmalev, P., Yadroitsava, I., Johansson, S. & Smurov, I. Energy input effect on morphology and microstructure of selective laser melting single track from metallic powder. *Journal of Materials Processing Technology* **213**, 606-613 (2013).

72 Li, S., Wei, Q., Shi, Y., Zhu, Z. & Zhang, D. Microstructure Characteristics of Inconel 625 Superalloy Manufactured by Selective Laser Melting. *Journal of Materials Science & Technology* **31**, 946-952 (2015).

73 Johannes, S., Michael, T. & Uwe, G. Mechanical and Microstructural Investigation of Nickel - Based Superalloy IN718 Manufactured by Selective Laser Melting (SLM). *Advanced Engineering Materials* **17**, 1099-1105 (2015).

74 Liu, F. *et al.* The effect of laser scanning path on microstructures and mechanical properties of laser solid formed nickel-base superalloy Inconel 718. *Journal of Alloys and Compounds* **509**, 4505-4509 (2011).

75 Jia, Q. & Gu, D. Selective laser melting additive manufactured Inconel 718 superalloy parts: High-temperature oxidation property and its mechanisms. *Optics & Laser Technology* **62**, 161-171 (2014).

76 Vilaro, T., Colin, C., Bartout, J. D., Nazé, L. & Sennour, M. Microstructural and mechanical approaches of the selective laser melting process applied to a nickel-base superalloy. *Materials Science and Engineering: A* **534**, 446-451 (2012).

77 Cloots, M., Kunze, K., Uggowitzer, P. J. & Wegener, K. Microstructural characteristics of the nickel-based alloy IN738LC and the cobalt-based alloy Mar-M509 produced by selective laser melting. *Materials Science and Engineering: A* **658**, 68-76 (2016).

78 Amato, K. N. *et al.* Microstructures and mechanical behavior of Inconel 718 fabricated by selective laser melting. *Acta Materialia* **60**, 2229-2239 (2012).

79 Delgado, J., Ciurana, J. & Rodríguez, C. A. Influence of process parameters on part quality and mechanical properties for DMLS and SLM with iron-based materials. *The International Journal of Advanced Manufacturing Technology* **60**, 601-610 (2012).

80 Wang, Y., Chen, M., Zhou, F. & Ma, E. High tensile ductility in a nanostructured metal. *Nature* **419**, 912 (2002).

81 Yan, F., Liu, G., Tao, N. & Lu, K. Strength and ductility of 316L austenitic stainless steel strengthened by nano-scale twin bundles. *Acta Materialia* **60**, 1059-1071 (2012).

82 Burger, G., Gupta, A., Jeffrey, P. & Lloyd, D. Microstructural control of aluminum sheet used in automotive applications. *Materials Characterization* **35**, 23-39 (1995).

83 Starke Jr, E. & Staley, J. Application of modern aluminum alloys to aircraft. *Progress in Aerospace Sciences* **32**, 131-172 (1996).

84 Prasad, S. & Asthana, R. Aluminum metal-matrix composites for automotive applications: tribological considerations. *Tribology letters* **17**, 445-453 (2004).

85 Li, R. *et al.* Densification behavior of gas and water atomized 316L stainless steel powder during selective laser melting. *Applied Surface Science* **256**, 4350-4356 (2010).

86 Lu, L., Shen, Y., Chen, X., Qian, L. & Lu, K. Ultrahigh Strength and High Electrical Conductivity in Copper. *Science* **304**, 422-426 (2004).

87 Hirosawa, S., Shigemoto, Y., Miyoshi, T. & Kanekiyo, H. Direct formation of Fe3B/Nd2Fe14B nanocomposite permanent magnets in rapid solidification. *Scripta materialia* **48**, 839-844 (2003).

88 Liu, W., Cao, C., Xu, J., Wang, X. & Li, X. Molten salt assisted solidification nanoprocessing of Al-TiC nanocomposites. *Materials Letters* **185**, 392-395 (2016).

89 Li, X. P. *et al.* Selective laser melting of nano-TiB2 decorated AlSi10Mg alloy with high fracture strength and ductility. *Acta Materialia* **129**, 183-193 (2017).

90 Lee, D. W. & Kim, B. K. Nanostructured Cu–Al 2 O 3 composite produced by thermochemical process for electrode application. *Materials Letters* **58**, 378-383 (2004).

91 Zhang, X.-H. *et al.* Investigation on microstructure and properties of Cu–Al 2 O 3 composites fabricated by a novel in-situ reactive synthesis. *Materials & Design* **92**, 58-63 (2016).

92 Chandrasekhar, S. *et al.* Microstructure and properties of hot extruded Cu–1wt% Al 2 O 3 nano-composites synthesized by various techniques. *Materials Science and Engineering: A* **591**, 46-53 (2014).

93 Xu, J., Chen, L., Choi, H. & Li, X. Theoretical study and pathways for nanoparticle capture during solidification of metal melt. *Journal of Physics: Condensed Matter* **24**, 255304 (2012).

94 Casati, R. & Vedani, M. Metal matrix composites reinforced by nano-particles—a review. *Metals* **4**, 65-83 (2014).

95 Low, C., Wills, R. & Walsh, F. Electrodeposition of composite coatings containing nanoparticles in a metal deposit. *Surface and Coatings Technology* **201**, 371-383 (2006).

96 Chen, H. *et al.* Sliding wear behaviour of laser clad coatings based upon a nickel-based self-fluxing alloy co-deposited with conventional and nanostructured tungsten carbide–cobalt hardmetals. *Wear* **259**, 801-806 (2005).

97 Wang, A. *et al.* Ni-based alloy/submicron WS2 self-lubricating composite coating synthesized by Nd: YAG laser cladding. *Materials Science and Engineering: A* **475**, 312-318 (2008).

98 Yan, H. *et al.* Nd: YAG laser cladding Ni base alloy/nano-h-BN self-lubricating composite coatings. *Materials Science and Technology* **26**, 461-468 (2010).

99 Jiang, D. *et al.* Fabrication of nano-TiCp reinforced Inconel 625 composite coatings by partial dissolution of micro-TiCp through laser cladding energy input control. *Surface and Coatings Technology* **249**, 125-131 (2014).

100 Wu, X. & Hong, Y. Surface amorphous and crystalline microstructure by alloying zirconium using Nd: YAG pulsed laser. *Metallurgical and Materials Transactions A* **31**, 3123-3127 (2000).

101 Choudhury, A. R., Ezz, T., Chatterjee, S. & Li, L. Microstructure and tribological behaviour of nano-structured metal matrix composite boride coatings synthesized by combined laser and sol–gel technology. *Surface and Coatings Technology* **202**, 2817-2829 (2008).

102 Ezz, T., Crouse, P., Li, L. & Liu, Z. Laser/sol–gel synthesis: a novel method for depositing nanostructured TiN coatings in non-vacuum conditions. *Applied Physics A* **85**, 79-82 (2006).

103 Choudhury, A. R., Ezz, T. & Li, L. Synthesis of hard nano-structured metal matrix composite boride coatings using combined laser and sol–gel technology. *Materials Science and Engineering: A* **445**, 193-202 (2007).

104 Kumar, A., Mahapatra, M. M. & Jha, P. K. Fabrication and characterizations of mechanical properties of Al-4.5% Cu/10TiC composite by in-situ method. *Journal of Minerals and Materials Characterization and Engineering* **11**, 1075 (2012).

105 Bai, J. G., Creehan, K. D. & Kuhn, H. A. Inkjet printable nanosilver suspensions for enhanced sintering quality in rapid manufacturing. *Nanotechnology* **18**, 185701 (2007).

106 Czyżewski, J., Burzyński, P., Gaweł, K. & Meisner, J. Rapid prototyping of electrically conductive components using 3D printing technology. *Journal of Materials Processing Technology* **209**, 5281-5285 (2009).

107 Wong, K. V. & Hernandez, A. A review of additive manufacturing. *ISRN Mechanical Engineering* **2012** (2012).

108 Wozniak, M., Graule, T., de Hazan, Y., Kata, D. & Lis, J. Highly loaded UV curable nanosilica dispersions for rapid prototyping applications. *Journal of the European Ceramic Society* **29**, 2259-2265 (2009).

109 Sandoval, J. *et al.* Nanotailoring stereolithography resins for unique applications using carbon nanotubes. *The Sixteenth Solid Freeform Fabrication Proceedings*, 3-5 (2005).

110 Shofner, M., Lozano, K., Rodríguez - Macías, F. & Barrera, E. Nanofiber - reinforced polymers prepared by fused deposition modeling. *Journal of applied polymer science* **89**, 3081-3090 (2003).

111 Chartoff, R., McMorrow, B. & Lucas, P. in *Solid Freeform Fabrication Symposium Proc.* 385-391.

112 Kim, J. *et al.* Rapid-prototyped PLGA/β-TCP/hydroxyapatite nanocomposite scaffolds in a rabbit femoral defect model. *Biofabrication* **4**, 025003 (2012).

113 De Santis, R. *et al.* 3D fibre deposition and stereolithography techniques for the design of multifunctional nanocomposite magnetic scaffolds. *Journal of Materials Science: Materials in Medicine* **26**, 250 (2015).

114 Kim, J. & Creasy, T. Selective laser sintering characteristics of nylon 6/clay-reinforced nanocomposite. *Polymer Testing* **23**, 629-636 (2004).

115 Zheng, H., Zhang, J., Lu, S., Wang, G. & Xu, Z. Effect of core–shell composite particles on the sintering behavior and properties of nano-Al2O3/polystyrene composite prepared by SLS. *Materials Letters* **60**, 1219-1223 (2006).

116 Wahab, M., Dalgarno, K., Cochrane, R. & Hassan, S. in *Proceedings of the World Congress on Engineering WCE.*

117 Kim, H. C. *et al.* in *Proceedings of the 18th International Solid Freeform Fabrication Symposium (SFF 2007), The University of Texas at Austin.* 367-376.

118 Duan, B. *et al.* Three-dimensional nanocomposite scaffolds fabricated via selective laser sintering for bone tissue engineering. *Acta biomaterialia* **6**, 4495-4505 (2010).

119 Chang, K. & Gu, D. Direct metal laser sintering synthesis of carbon nanotube reinforced Ti matrix composites: Densification, distribution characteristics and properties. *Journal of Materials Research* **31**, 281-291 (2016).

120 Gu, D. & Shen, Y. Direct laser sintered WC-10Co/Cu nanocomposites. *Applied Surface Science* **254**, 3971-3978 (2008).

121 Lin, D., Richard Liu, C. & Cheng, G. J. Laser sintering of separated and uniformly distributed multiwall carbon nanotubes integrated iron nanocomposites. *Journal of Applied Physics* **115**, 113513 (2014).

122 Ready, J. F. & Farson, D. F. *LIA handbook of laser materials processing*. (Laser Institute of America Orlando, 2001).

123 AlMangour, B., Grzesiak, D. & Yang, J.-M. Rapid fabrication of bulk-form TiB 2/316L stainless steel nanocomposites with novel reinforcement architecture and improved performance by selective laser melting. *Journal of Alloys and Compounds* **680**, 480-493 (2016).

124 Martin, J. H. *et al.* 3D printing of high-strength aluminium alloys. *Nature* **549**, 365 (2017).

125 AlMangour, B., Grzesiak, D. & Yang, J.-M. Rapid fabrication of bulk-form TiB2/316L stainless steel nanocomposites with novel reinforcement architecture and improved performance by selective laser melting. *Journal of Alloys and Compounds* **680**, 480-493 (2016).

126 Chen, M. *et al.* Novel composite powders with uniform TiB2 nano-particle distribution for 3D printing. *Applied Sciences* **7**, 250 (2017).

127 Xu, J., Chen, L., Choi, H., Konish, H. & Li, X. Assembly of metals and nanoparticles into novel nanocomposite superstructures. *Scientific Report* **3**, 1730 (2013).

128 Li, X., Kong, C., Becker, T. & Sercombe, T. Investigation of interfacial reaction products and stress distribution in selective laser melted Al12Si/SiC composite using confocal Raman microscopy. *Advanced Engineering Materials* **18**, 1337-1341 (2016).

129 Gu, D. & Shen, Y. Effects of dispersion technique and component ratio on densification and microstructure of multi-component Cu-based metal powder in direct laser sintering. *Journal of Materials Processing Technology* **182**, 564-573 (2007).

130 Wang, L. *et al.* Microstructure and tensile properties of in situ synthesized nano-sized TiCx/2009Al composites. *Materials & Design* **79**, 68-72 (2015).

131 Gu, D. & Shen, Y. Balling phenomena in direct laser sintering of stainless steel powder: Metallurgical mechanisms and control methods. *Materials & Design* **30**, 2903-2910 (2009).

132 Halliday, D., Resnick, R. & Merrill, J. *Fundamentals of physics*. Vol. 9 (Wiley New York, 1981).

133 Nelson, I. C., Banerjee, D. & Ponnappan, R. Flow loop experiments using polyalphaolefin nanofluids. *Journal of thermophysics and heat transfer* **23**, 752 (2009).

134 Tiznobaik, H. & Shin, D. Enhanced specific heat capacity of high-temperature molten salt-based nanofluids. *International Journal of Heat and Mass Transfer* **57**, 542-548 (2013).

135 Zebarjadi, M. *et al.* Power factor enhancement by modulation doping in bulk nanocomposites. *Nano letters* **11**, 2225-2230 (2011).

136 Poudel, B. *et al.* High-thermoelectric performance of nanostructured bismuth antimony telluride bulk alloys. *Science* **320**, 634-638 (2008).

137 Biswas, K. *et al.* High-performance bulk thermoelectrics with all-scale hierarchical architectures. *Nature* **489**, 414-418 (2012).

138 Vineis, C. J., Shakouri, A., Majumdar, A. & Kanatzidis, M. G. Nanostructured thermoelectrics: big efficiency gains from small features. *Advanced Materials* **22**, 3970-3980 (2010).

139 Mingo, N., Hauser, D., Kobayashi, N., Plissonnier, M. & Shakouri, A. "Nanoparticle-in-Alloy" approach to efficient thermoelectrics: silicides in SiGe. *Nano letters* **9**, 711-715 (2009).

140 Henry, A. & Chen, G. High thermal conductivity of single polyethylene chains using molecular dynamics simulations. *Physical review letters* **101**, 235502 (2008).

141 Corcione, M. Empirical correlating equations for predicting the effective thermal conductivity and dynamic viscosity of nanofluids. *Energy Conversion and Management* **52**, 789-793 (2011).

142 Vafaei, S., Purkayastha, A., Jain, A., Ramanath, G. & Borca-Tasciuc, T. The effect of nanoparticles on the liquid–gas surface tension of Bi2Te3 nanofluids. *Nanotechnology* **20**, 185702 (2009).

143 Vafaei, S. *et al.* Effect of nanoparticles on sessile droplet contact angle. *Nanotechnology* **17**, 2523 (2006).

144 Kim, S., Bang, I. C., Buongiorno, J. & Hu, L. Effects of nanoparticle deposition on surface wettability influencing boiling heat transfer in nanofluids. *Applied Physics Letters* **89**, 153107 (2006).

145 Bahk, J.-H. *et al.* Thermoelectric power factor enhancement by ionized nanoparticle scattering. *Applied Physics Letters* **99**, 072118 (2011).

146 Selezneva, E. *et al.* Thermoelectric transport in InGaAs with high concentration of rare-earth TbAs embedded nanoparticles. *Journal of electronic materials* **41**, 1820-1825 (2012).

147 Zebarjadi, M. *et al.* Effect of nanoparticle scattering on thermoelectric power factor. *Applied Physics Letters* **94**, 202105 (2009).

148 Koirala, M. *et al.* Thermoelectric property enhancement by Cu nanoparticles in nanostructured FeSb2. *Applied Physics Letters* **102**, 213111 (2013).

149 Minnich, A., Dresselhaus, M., Ren, Z. & Chen, G. Bulk nanostructured thermoelectric materials: current research and future prospects. *Energy & Environmental Science* **2**, 466-479 (2009).

150 Heringhaus, F., Schneider-Muntau, H.-J. & Gottstein, G. Analytical modeling of the electrical conductivity of metal matrix composites: application to Ag–Cu and Cu–Nb. *Materials Science and Engineering: A* **347**, 9-20 (2003).

151 Weber, L., Fischer, C. & Mortensen, A. On the influence of the shape of randomly oriented, non-conducting inclusions in a conducting matrix on the effective electrical conductivity. *Acta materialia* **51**, 495-505 (2003).

152 Zebarjadi, M., Esfarjani, K., Dresselhaus, M., Ren, Z. & Chen, G. Perspectives on thermoelectrics: from fundamentals to device applications. *Energy & Environmental Science* **5**, 5147-5162 (2012).

153 Zhang, Z. & Chen, D. Contribution of Orowan strengthening effect in particulate-reinforced metal matrix nanocomposites. *Materials Science and Engineering: A* **483**, 148-152 (2008).

154 Dieter, G. E. & Bacon, D. J. *Mechanical metallurgy*. Vol. 3 (McGraw-hill New York, 1986).

155 Zhang, Q. & Chen, D. A model for predicting the particle size dependence of the low cycle fatigue life in discontinuously reinforced MMCs. *Scripta materialia* **51**, 863-867 (2004).

156 Sanaty-Zadeh, A. Comparison between current models for the strength of particulate-reinforced metal matrix nanocomposites with emphasis on consideration of Hall–Petch effect. *Materials Science and Engineering: A* **531**, 112-118 (2012).

157 Nardone, V. C. & Prewo, K. M. On the strength of discontinuous silicon carbide reinforced aluminum composites. *Scripta Metallurgica* **20**, 43-48 (1986).

158 Hull, D. & Bacon, D. J. *Introduction to dislocations*. (Butterworth-Heinemann, 2001).

159 King, W. E. *et al.* Laser powder bed fusion additive manufacturing of metals; physics, computational, and materials challenges. *Applied Physics Reviews* **2**, 041304 (2015).

160 Gusarov, A. V., Yadroitsev, I., Bertrand, P. & Smurov, I. Heat transfer modelling and stability analysis of selective laser melting. *Applied Surface Science* **254**, 975-979 (2007).

161 Karantzalis, A., Lekatou, A., Georgatis, M., Poulas, V. & Mavros, H. Casting-Based Production of Al-TiC-AlB 2 Composite Material Through the Use of KBF 4 Salt. *Journal of materials engineering and performance* **20**, 198-202 (2011).

162 Zhong, M. & Liu, W. Laser surface cladding: The state of the art and challenges. *Proceedings of the Institution of Mechanical Engineers, Part C: Journal of Mechanical Engineering Science* **224**, 1041-1060 (2010).

163 Dimiduk, D. M., Uchic, M. D. & Parthasarathy, T. A. Size-affected single-slip behavior of pure nickel microcrystals. *Acta Materialia* **53**, 4065-4077 (2005).

164 Sillekens, W. H. *et al.* The ExoMet Project: EU/ESA Research on High-Performance Light-Metal Alloys and Nanocomposites. *Metallurgical and Materials Transactions A* **45**, 3349-3361 (2014).

165 Thangaraju, S., Heilmaier, M., Murty, B. S. & Vadlamani, S. S. On the Estimation of True Hall–Petch Constants and Their Role on the Superposition Law Exponent in Al Alloys. *Advanced Engineering Materials* **14**, 892-897 (2012).

166 Singh, S. S., Guo, E., Xie, H. & Chawla, N. Mechanical properties of intermetallic inclusions in Al 7075 alloys by micropillar compression. *Intermetallics* **62**, 69-75 (2015).

167 May, J., Höppel, H. & Göken, M. Strain rate sensitivity of ultrafine-grained aluminium processed by severe plastic deformation. *Scripta Materialia* **53**, 189-194 (2005).

168 Pozuelo, M., Chang, Y. & Yang, J. Effect of diamondoids on the microstructure and mechanical behavior of nanostructured Mg-matrix nanocomposites. *Materials Science and Engineering: A* **633**, 200-208 (2015).

169 Guo, E.-Y. *et al.* Mechanical characterization of microconstituents in a cast duplex stainless steel by micropillar compression. *Materials Science and Engineering: A* **598**, 98-105 (2014).

170 Gong, J. & Wilkinson, A. J. A microcantilever investigation of size effect, solid-solution strengthening and second-phase strengthening for< a> prism slip in alpha-Ti. *Acta Materialia* **59**, 5970-5981 (2011).

171 Cordero, Z. C. *et al.* Powder-route synthesis and mechanical testing of ultrafine grain tungsten alloys. *Metallurgical and Materials Transactions A* **45**, 3609-3618 (2014).

172 Girault, B., Schneider, A. S., Frick, C. P. & Arzt, E. Strength Effects in Micropillars of a Dispersion Strengthened Superalloy. *Advanced Engineering Materials* **12**, 385-388 (2010).

173 Mazaheri, Y., Meratian, M., Emadi, R. & Najarian, A. R. Comparison of microstructural and mechanical properties of Al–TiC, Al–B4C and Al–TiC–B4C composites prepared by casting techniques. *Materials Science and Engineering: A* **560**, 278-287 (2013).

174 Suthar, J. & Patel, K. M. Processing issues, machining, and applications of aluminum metal matrix composites. *Materials and Manufacturing Processes* **33**, 499-527 (2018).

175 Contreras, A., Albiter, A. & Pérez, R. Microstructural properties of the Al–Mg x / TiC composites obtained by infiltration techniques. *Journal of Physics: Condensed Matter* **16**, S2241 (2004).

176 Kennedy, A. R., Karantzalis, A. E. & Wyatt, S. M. The microstructure and mechanical properties of TiC and TiB2-reinforced cast metal matrix composites. *Journal of Materials Science* **34**, 933-940 (1999).

177 Selcuk, C. & Kennedy, A. R. Al–TiC composite made by the addition of master alloys pellets synthesised from reacted elemental powders. *Materials Letters* **60**, 3364-3366 (2006).

178 Bauri, R., Yadav, D. & Suhas, G. Effect of friction stir processing (FSP) on microstructure and properties of Al–TiC in situ composite. *Materials Science and Engineering: A* **528**, 4732-4739 (2011).

179 Shyu, R. F. & Ho, C. T. In situ reacted titanium carbide-reinforced aluminum alloys composite. *Journal of Materials Processing Technology* **171**, 411-416 (2006).

180 Rai, R. N., Rao, A., Dutta, G. & Chakraborty, M. in *Materials Science Forum.* 418-422 (Trans Tech Publ).

181 Mohapatra, S., Chaubey, A. K., Mishra, D. K. & Singh, S. K. Fabrication of Al–TiC composites by hot consolidation technique: its microstructure and mechanical properties. *Journal of Materials Research and Technology* **5**, 117-122 (2016).

182 Bobbili, R., Madhu, V. & Gogia, A. K. Tensile behaviour of aluminium 7017 alloy at various temperatures and strain rates. *Journal of Materials Research and Technology* **5**, 190-197 (2016).

183 Chen, J. & Young, B. Stress–strain curves for stainless steel at elevated temperatures. *Engineering Structures* **28**, 229-239 (2006).

184 El-Magd, E. & Abouridouane, M. Characterization, modelling and simulation of deformation and fracture behaviour of the light-weight wrought alloys under high strain rate loading. *International Journal of Impact Engineering* **32**, 741-758 (2006).

185 Maisonnette, D., Suery, M., Nelias, D., Chaudet, P. & Epicier, T. Effects of heat treatments on the microstructure and mechanical properties of a 6061 aluminium alloy. *Materials Science and Engineering: A* **528**, 2718-2724 (2011).

186 Ramesh, P. D., Vaidhyanathan, B., Ganguli, M. & Rao, K. J. Synthesis of β-SiC powder by use of microwave radiation. *Journal of Materials Research* **9**, 3025-3027 (2011).

187 Liu, Z., Rakita, M., Xu, W., Wang, X. & Han, Q. Ultrasound assisted combustion synthesis of TiC in Al–Ti–C system. *Ultrasonics Sonochemistry* **27**, 631-637 (2015).

188 Saidi, A. & JV, W. Reaction synthesis of TiC and Fe-TiC composites. *ISIJ international* **37**, 188-193 (1997).

189 Mengxian, Z., Yanqiu, H., Li, M., Bin, H. & Qiaodan, H. In Situ TiC Ceramic Particles Locally Reinforced Al-Si Matrix Composites Prepared by SHS-Casting Method from the Al-Si-Ti-C System. *International Journal of Applied Ceramic Technology* **11**, 723-731 (2014).

190 Jeffers, E. A. *Reaction Synthesis of Titanium Aluminide/Titanium Diboride in-Situ Composites*, Virginia Tech, (2006).

191 Luo, Y.-R. *Handbook of bond dissociation energies in organic compounds*. (CRC press, 2002).

192 Chou, R., Milligan, J., Paliwal, M. & Brochu, M. Additive manufacturing of Al-12Si alloy via pulsed selective laser melting. *Jom* **67**, 590-596 (2015).

193 Mills, K. C. *Recommended values of thermophysical properties for selected commercial alloys*. (Woodhead Publishing, 2002).